Title

Energy Transfer in the Face of Disorder: Spatiotemporal Probing of Artificial and Natural Light Harvesting Complexes

Author

Hamerlynck, Leo

Publication Date

2024

Energy Transfer in the Face of Disorder: Spatiotemporal Probing of Artificial and Natural Light Harvesting Complexes

by

Leo Hamerlynck

A dissertation submitted in partial satisfaction of the

requirements for the degree of

Doctor of Philosophy

in

Chemistry

in the

Graduate Division

of the

University of California, Berkeley

Committee in charge:

Professor Naomi S. Ginsberg, Chair
Professor Ke Xu
Professor Na Ji

Summer 2024

Energy Transfer in the Face of Disorder: Spatiotemporal Probing of Artificial and Natural Light Harvesting Complexes

Abstract

Energy Transfer in the Face of Disorder: Spatiotemporal Probing of Artificial and Natural Light Harvesting Complexes

by

Leo Hamerlynck

Doctor of Philosophy in Chemistry

University of California, Berkeley

Professor Naomi S. Ginsberg, Chair

Photosynthesis, the process by which plants and some bacteria convert sunlight into usable chemical energy, is a remarkable process that feeds nearly all of life on earth. At the smallest scales, photosynthesis is driven by molecular machinery in the form of various light-harvesting protein complexes (LHCs) contained in bacterial cells and in the chloroplasts of plant cells. At the earliest stages in photosynthesis, a photon of sunlight is absorbed by a small light-absorbing molecule (a "chromophore") and that energy is transported through a network of chromophores contained in these proteins towards specialized reaction centers where chemistry begins. This transfer process is remarkably efficient, and can result in nearly all absorbed photons reaching the reaction centers successfully. Understanding what factors of the design of these protein complexes give rise to this efficiency is thus of great interest for developing novel light-harvesting technologies. In this work, we present a series of studies focused on understanding the factors important to achieving efficient light harvesting, by spectro- and spatiotemporally resolving the few picoseconds-to-nanoseconds after photoexcitation in artificial and natural light harvesting complexes.

Chapter 1 presents a brief introduction to photosynthetic light-harvesting complexes in a variety of organisms. These complexes present a number of challenges to systematic study that kept open questions about their structure-function relationships even after over a century of study. We summarize some of these challenges and lay out our approaches to overcoming them.

Chapter 2 gives an introduction to transient absorption (TA) and transient absorption anisotropy (TAA) spectroscopy, from basic principles to practical implementation. TAA is a powerful technique for measuring energy transfer by measuring the depolarization of the transient absorption signal caused by energy transfer. We detail the implementation of a high signal-to-noise ratio TAA apparatus built in order to apply this technique to artificial light harvesting complexes.

Chapter 3 explores the role of disorder in intra-LHC energy transfer in an artificial LHC based on a circular permutant of the tobacco mosaic virus coat protein (cpTMV). This model system afford far greater control to perform systematic investigation than natural LHCs. In this study we measure the intra-complex energy transfer in these model LHCs using TAA spectroscopy and model that transport via kinetic Monte Carlo simulations. We find that fast site-to-site hopping as high as 1.6 ps^{-1} is occurring in these complexes. With these simulations, we identify static disorder in orientation, site energy, and degree of coupling as key remaining factors to control to achieve long-range energy transfer in these systems. We thereby establish this system as a highly promising, bottom-up model for studying long-range energy transfer in light-harvesting protein complexes.

Chapter 4 introduces stroboscopic interferometric scattering microscopy (stroboSCAT), a label-free, time-resolved microscopy technique that can directly image energy carriers from excitons to heat in a broad range of materials. We provide an overview of the technique and detail improvements made to the technique to increase time resolution in order to study the first few picoseconds of natural light harvesting complexes. To achieve this objective we coupled an ultrafast laser source into the microscope, increasing the time resolution of the apparatus by over two orders of magnitude, to below 1 ps. We present a study of short-lived photogenerated charge carriers' migration in silicon, previously barely detectable with our lower time resolution, where we observe density-dependent diffusivity as a result of carrier-carrier scattering.

Chapter 5 presents ongoing spatially-resolved measurements of exciton migration and exciton-exciton annihilation in de-enveloped thylakoid membranes from green plants via stroboSCAT. We find that exciton-exciton annihilation dominates the observed spatial response and present a model to simultaneously fit exciton diffusion and annihilation, leveraging the spatial resolution to capture both. Finally, we provide a number of future directions and propose improvements to the apparatus to facilitate future experiments on these samples.

Taken together, this dissertation presents a set of novel approaches to studying energy transfer in LHCs that reveals the role of disorder and many-body interactions in photosynthetic light-harvesting. Both by studying novel model systems via a more well-established spectroscopic technique and by studying well-established natural photosynthetic samples via a novel microscopic technique, we unveil new findings about the important role that disorder plays in these fascinating systems.

À Maman et Poppers

Contents

Contents **ii**

List of Figures **iv**

List of Tables **vi**

1 Introduction **1**
- 1.1 Primer on photosynthetic light harvesting 1
- 1.2 Energy transfer and transport in photosynthetic light harvesting 4
- 1.3 Challenges with and progress on understanding photosynthetic light harvesting 6
- 1.4 Our novel approaches to studying photosynthetic light-harvesting 7

2 Transient Absorption Spectroscopy & Polarization Anisotropy **9**
- 2.1 Transient Absorption Spectroscopy 9
- 2.2 Transient Absorption Anisotropy Spectroscopy 16
- 2.3 Developing a high signal-to-noise ratio TAA apparatus 19

3 Static disorder has a dynamic effect on energy transfer in biomimetic light harvesting complexes **24**
- 3.1 Preparation of singly-labeled control complexes and fully-labeled LHCs . . . 26
- 3.2 Transient Absorption Anisotropy and Time-Resolved Fluorimetry of Artificial LHCs 28
- 3.3 Kinetic Monte Carlo simulations of FRET hopping in TMV complexes . . . 33
- 3.4 Impacts of disorder on excitation migration in artificial cpTMV LHCs 44
- 3.5 Outlook and future prospects for cpTMV LHCs 48

4 Implementing ultrafast stroboSCAT for spatiotemporally resolving energy migration in LHCs **50**
- 4.1 Introduction to iSCAT and stroboSCAT 50
- 4.2 Improving the time resolution of stroboSCAT 54
- 4.3 Ultrafast investigation of energy flow in silicon 69

5 Quantifying Diffusion and Exciton-Exciton Annihilation in Thylakoid Membranes via stroboSCAT 79
5.1 Addressing challenges in preparing biological samples for stroboSCAT microscopy 81
5.2 Direct imaging of excitons in thylakoid membranes 85
5.3 Feasibility study and recommendations for future experiments 91

6 Concluding Remarks 98

Bibliography 100

A Practical guide to alignment and taking measurements on TAA apparatus 109
A.1 Probe path alignment 109
A.2 Pump path alignment 111
A.3 Sample stage and detection alignment 112

B Optics diagrams of stroboSCAT microscope 114

List of Figures

1.1 Schematic illustrations of major light harvesting complexes in cyanobacteria, purple bacteria, and plants. 2

2.1 Schematic explanation of transient absorption spectroscopy. 10
2.2 Visual explanation of the instrument response function for a hypothetical instrument. 13
2.3 Illustration of TA anisotropy via simulated TA data for a hypothetical species . 18
2.4 Transient absorption anisotropy configurations and signal-to-noise ratio improvement. 21

3.1 Overview of the TAA experiment on cpTMV-SRB biomimetic light harvesting complexes. 25
3.2 TAA data of singly-labeled cpTMV-SRB control samples at different sites on the protein surface. 27
3.3 Spectroscopically resolving energy transfer in the cpTMV LHC. 29
3.4 Magic-angle TA kinetics of cpTMV complexes and free dye control. 30
3.5 Schematic representation of manifestation of energy transfer in time-resolved emission spectra. 31
3.6 Components of triexponential fit to TRES of fully-labeled cpTMV LHC. 32
3.7 Overview of kinetic Monte Carlo simulation setup and results. 34
3.8 The orientational and energetic parameters passed to the kinetic Monte Carlo simulation. 35
3.9 Convergence of the computed observables in kinetic Monte Carlo simulations . . 39
3.10 Simulated energy transfer observables in the cpTMV LHC. 42

4.1 A diagram of the principles of iSCAT and stroboSCAT. 52
4.2 Schematic diagram of original diode laser-based stroboSCAT setup. 56
4.3 Diagram of homebuilt 3-axis microscope stage used in stroboSCAT. 57
4.4 Simplified optics diagram of the three stroboSCAT configurations. 59
4.5 StroboSCAT images of thylakoid membrane before and after changing LabVIEW averaging routine. 62
4.6 Benchmark stroboSCAT measurement on TIPS pentacene crystal domain. . . . 65
4.7 Top and side view of “sandwich” sample geometry for silicon measurements. . . 69

4.8 Diode laser stroboSCAT measurements of charge carriers and heat in p-doped silicon. 71
4.9 Ultrafast stroboSCAT measurement of charge carriers in undoped silicon. 73
4.10 Comparison of the relative amplitudes of a short-lived and long-lived signal as IRF width increases. 74
4.11 Early-time stroboSCAT data on undoped silicon. 76

5.1 Confocal fluorescence microscopy images of thylakoid samples on glass coverslips. 82
5.2 Thylakoid sample preparation for stroboSCAT. 84
5.3 StroboSCAT study on thylakoid membranes with and without DCMU. 87
5.4 stroboSCAT pump fluence series showing annihilation dominating exciton diffusion to varying degrees in thylakoid membranes. 88
5.5 Simulated stroboSCAT data based on simple diffusion model. 92
5.6 Diffusion simulation with circular "grana" domains. 93
5.7 Sample vibration in x and y directions extracted from a 500-frame iSCAT movie of a thylakoid sample. 95

A.1 Optics diagram of high signal-to-noise ratio transient absorption anisotropy apparatus. 110

B.1 Optical diagram of the newly configured stroboSCAT microscope. 115
B.2 Proposed reconfiguration of stroboSCAT microscope to shorten probe path length and reduce vibration effects. 116

List of Tables

3.1 Multiexponential reconvolution fits for magic-angle TA kinetics. 30

4.1 Results of Gaussian peak fits to diode laser stroboSCAT data shown in Fig. 4.8(c) and (d), and resulting calculation of integrated peak volumes. 72

5.1 Parameters from partial differential equation fits for pump fluence stroboSCAT series. 90

Acknowledgments

I have many people to thank for helping me during my graduate program and making it a memorable experience. The work presented here would not have been possible without the support, encouragement, and friendship of all the people below, and many more.

Thank you Naomi for all your guidance and support throughout my time here. Thank you for creating an atmosphere where everyone is kind and respectful towards one another, and asking questions is always accepted and encouraged. Thank you for all the conversations and troubleshooting that helped me navigate my PhD, on topics ranging from experimental setup and data analysis to HVAC issues and gardening. Lastly, thank you for your patience and flexibility with my tendency to push up against deadlines, and for always encouraging self-compassion.

Thanks to all of my labmates in the Ginsberg lab whom I've had the pleasure to work with for the past six years. Thank you to Trevor for mentoring me when I first joined the group, for showing me the ropes of ultrafast spectroscopy, and for numerous conversations in our time as office-mates, on everything from science to Game of Thrones. Thank you to James for sharing your wisdom on time-resolved spectroscopy and for sharing your musical talents with us all. Thank you to Rongfeng and Steph for working with me to learn stroboSCAT together, which would not have been possible without Hannah's expertise and guidance, and thank you Rongfeng as well for gifting me your e-bike when you left for Guangzhou, which has radically improved my commute for the past year. Thank you Christian for your thoughtful discourse on the excellence of Hollow Knight and to Vivian for being the best softball coach, and to both thank you for many thoughtful discussions on a variety of scientific topics. Thank you to Elena for being a great mentee and partner in lab, and I wish you the best in your graduate career and beyond. To all the above and everyone else in the group I've been able to work with—Milan, Jon R, Ahyoung, Anwesha, Brendan, Rebecca, Jenna, Jon K, Alex L-P, Erin, Calvin, Livia, Alex S, JD, Sanjana, Namu, Taz, Ani, Ethan, Gerd, and others—thank you for your kindness, insightfulness, solidarity, and passion for lawn games, that have made my graduate experience great.

Thank you to the collaborators I have been lucky enough to work with throughout my time here. From Matt Francis' lab, thank you to Jing, Amanda, and Deb, all three remarkable chemical biologists whose protein-synthesizing and labeling capabilities have been and will continue to be essential for our progress understanding photosynthetic light-harvesting. Thanks to Julia Rogers from Phill Geissler's group, not only for running molecular dynamics simulations and helping me develop my kinetic Monte Carlo simulations, but also for being a great stat mech GSI in my first year. Thank you as well to Masa, for preparing thylakoid samples for me at the drop of a hat, and for always being quick to respond to my questions about natural photosynthesis. Thank you to Caroline McKeon from Jeff Neaton's lab for helping to bridge the gap between our experimental measurements and theory. To the many others who have consulted with me along the way, including Vahid Sandoghdar, Doran Raccah, and Will Tisdale, you also have my thanks.

Thank you to Jessie and Shobit for their hard work handling the administrative back-end of our lab and helping me when issues arose, and to Alexei Anderson, Steve Williams, and Peter Bolton, and other members of facilities services who have been helpful in keeping our labs running and office spaces habitable, and fixing issues with climate control and water leaks as quickly as they could.

Before coming to Berkeley, I was lucky to work as an undergraduate student researcher in the Armstrong lab at the University of Arizona. Thank you to Neal, Clayton, Jimmy, Kara, and Sona for fostering my interest in solar energy materials and teaching me practical fundamentals of research. Thank you also to Renske van der Veen, in whose lab I spent one summer and was first introduced to ultrafast spectroscopy, my interest in which led me to where I am today. Thanks to Tyler, who was a great mentor for my time there and first showed me how to align a laser, as well as Cecilia and Allan who were great office mates.

Thank you to the friends old and new who have supported me throughout my time here. Shout out to the Scotts and the rest of our first year study group who made first semester classes bearable. Thanks to my roommates Alex and Ben for keeping each other sane during the pandemic. And thank you to my friends who spent many nights unwinding with me over a video game: Nick and Kyle, for making time zone differences work, Scott and Nugent, for (almost) surviving the zombie apocalypse over and over, and Daniel, for all the great game and book recommendations and for being a great DM. Rock and stone, brothers.

Thank you to my coworkers in UAW Local 4811 who fight to make sure the work we do at UC can take place in a safe, respectful environment with adequate compensation to live in the cities where we work. Thanks to Garrett, Kavitha, Gerard, and Val, for first showing me that we could improve our workplace by standing together for change, and to David, Jess, Diane, Tanzil, Mia, Max, Iris, and many others whom I can't list here, for your solidarity through it all and for pushing me to be a better organizer. Thanks to Tarini, my bargaining team rep, and Khalid, Liz, Daniel, Conor, Ruby, Elise, and *the whole Chem OC* for fighting for better working conditions for the teaching and research we do in the Chemistry department.

Thank you to Sarah, who has loved and supported me during the final stretch of my graduate program. Thank you for always encouraging me to finish, for making me bean dishes for dinner when I was working late, for taking me new and exciting places in the great state of California, and for not holding it too hard against me that my experiments were all performed below 200 GPa.

Lastly, thank you to my family for getting me to where I am today. Thanks to Mama and Poppers for encouraging me to follow science and social and environmental justice since before I was blurting out, “Look, a solar panel!” at every passing emergency call box on the highway. Thanks to Roxane for spurring my creativity and challenging me to think critically about society, to Felix for honing your craftsmanship and inspiring me to try and do the same, and to Amelia, for balancing academic brilliance with an impish wit and sense of humor (Dame Fortuna hath smiled upon you!). I can't wait until we're all together again!

Chapter 1

Introduction

Photosynthesis is the process by which plants and some bacteria convert the energy from sunlight into chemical energy that serves as the fundamental energetic feedstock for almost all life on earth. Over billions of years, photosynthetic organisms have evolved exquisite molecular machinery to achieve this task with a balance of efficiency, adaptability, and stability. Of particular interest from a perspective of light-matter interactions are the very first steps in the light-dependent reactions of photosynthesis, wherein a photon is absorbed by a chromophore (i.e., a light-absorbing molecule) and that energy is then transported in the form of an electronic molecular excitation through a network of chromophores embedded in a protein environment to a reaction center complex where charge separation occurs and chemistry begins.

1.1 Primer on photosynthetic light harvesting

Chemically speaking, photosynthesis can be described as the light-driven reduction of inorganic carbon, typically carbon dioxide, into a bioavailable form such as glucose. To perform this reduction, a corresponding oxidation must occur, requiring an electron donor. In plants and cyanobacteria, this electron donor is water, which is oxidized to produce molecular oxygen as a byproduct:

$$6\,\mathrm{CO_2} + 6\,\mathrm{H_2O} \xrightarrow{h\nu} \mathrm{C_6H_{12}O_6} + 6\,\mathrm{O_2}$$

Other photosynthetic organisms such as purple bacteria evolved to utilize different electron donors, such as sulfur or hydrogen sulfide. The expression shown above is an oversimplification of an extensive and intricate biochemical mechanism in many ways, but the symbol $h\nu$ in particular does its fair share of heavy lifting. Because the photon flux of bright sunlight is only high enough to excite a chlorophyll molecule every tenth of a second or so,[1] nature has evolved a number of systems to absorb and concentrate sunlight energy into so-called "reaction centers," or the specialized chromophores where charge separation occurs. By doing so, the effective absorption cross section of the reaction centers is amplified by orders of

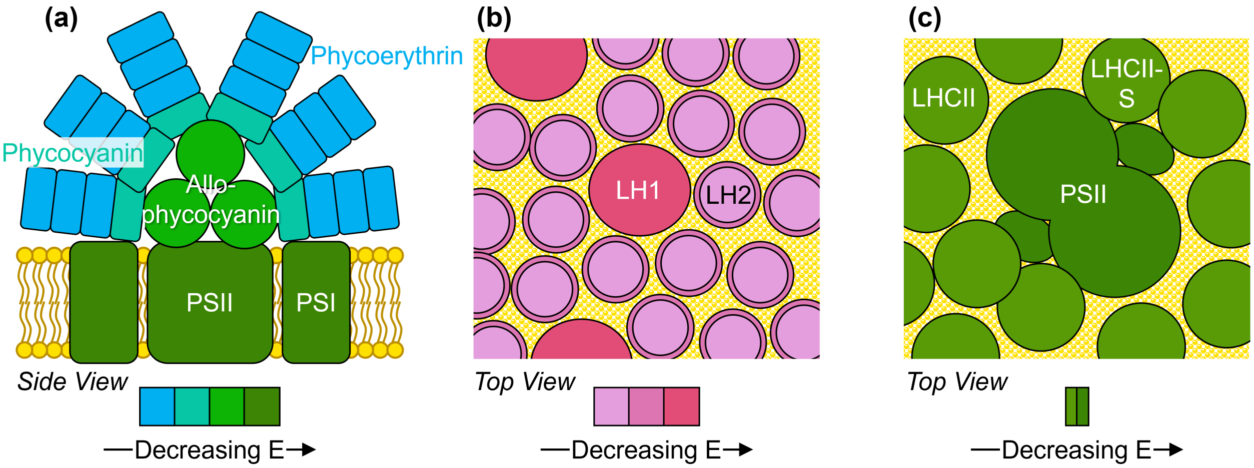

Figure 1.1: Schematic illustrations of major light harvesting complexes in cyanobacteria, purple bacteria, and plants. (a) The phycobilisome, found in cyanobacteria, is bound directly to photosystem II (PSII) and photosystem I (PSI) with a strong downhill energy gradient directed toward the reaction-center-containing PSII. (b) In purple bacteria, the multiple copies of light harvesting complex 2 (LH2) are arrayed within a membrane and act as antennae for light harvesting complex 1 (LH1), which contains the reaction center. (c) Light harvesting complex II in plants and green algae may be free (LHCII) or bound (LHCII-S) in the PSII supercomplex and act as antennae for PSII and PSI (not shown), with little downhill energy gradient.

magnitude, allowing the reaction centers to turn over far faster than they could as isolated molecules.

These sunlight-concentrating systems are known as light-harvesting complexes (LHC) and are composed of proteins packed with chromophores that both absorb light and transfer absorbed energy through both excitonic and resonance energy transfer toward the reaction center. Remarkably, across different species, in low light conditions these light-harvesting complexes achieve near 100% quantum efficiency, i.e., nearly all photons absorbed anywhere in the system are successfully transported to the reaction center.[2] When considering the fact that these are room-temperature condensed-phase molecular systems with considerable heterogeneity, this feat is doubly remarkable, and understanding how plants and bacteria achieve such high efficiencies has been the subject of much research.

Plants and bacteria have adopted a number of structural approaches to solar light harvesting, some of which are illustrated schematically in Fig. 1.1. In all cases, the molecular machinery core to light harvesting is in the form of integral membrane proteins, as, typically, these proteins operate by generating a potential across the membrane (such as a proton gradient) to drive the downstream light-dependent reactions. In cyanobacteria and plants, two important transmembrane protein complexes are photosystem I and II (dark green in Fig. 1.1(a) and (c)), which contain the reaction centers where photoredox chemistry occurs. In purple bacteria, the reaction center is contained in light-harvesting complex 1 (LH1, dark magenta ovals in Fig. 1.1(b)). While PSI, PSII, and LH1 all contain their own light-absorbing chromophores in addition to the reaction centers, they are in all cases surrounded by antennae complexes that greatly increase their effective absorption cross-section.

In cyanobacteria, attached to PSII on the outside of the membrane is an antenna complex known as the phycobilisome, which is depicted in Fig. 1.1(a). The phycobilisome, tens of nanometers across, consists of an allophycocyanin core (light green circles) surrounded by rod-shaped structures approximately 10-20 nm in length, composed of phycocyanin at the base (teal rectangles) and phycoerythrin far from the core (blue rectangles). As depicted by the color gradient, the chromophores in these proteins progressively decrease in light absorption energy as the proteins get closer to PSII, from 560 nm in phycoerythrin to 670 nm in PSII.[3] This creates a strong, short-ranged downhill energy gradient that directs energy from where light was absorbed towards the reaction center in PSII, over a distance of approximately 20 nm.

In purple bacteria, the antenna structure is arranged in two dimensions within the membrane, rather than on the third dimension above it, as depicted in the top-down view shown in Fig. 1.1(b). Unlike in cyanobacteria, here the antenna complexes, primarily 6 nm-diameter light harvesting complex 2 (LH2, light pink circles), are not bound directly to LH1 but are placed in close proximity by dense packing of these proteins within the membrane. LH2 contains bacteriochlorophyll chromophores in two chemical environments, the so-called B800 and B850 species, which absorb at 800 and 850 nm respectively, whiLle bacteriochlorophyll in LH1 absorb at 875 nm.[4] Thus, in purple bacteria there is also a downhill energy gradient directing absorbed energy toward the reaction-center-containing LH1; unlike in cyanobacteria, however, the distributed nature of the system means that excitations may have to travel over longer ranges between identical LH2 complexes before arriving at an LH1 complex. Indeed, in low-light conditions purple bacteria will grow excess LH2 resulting in large regions with no LH1, consisting only of semicrystalline LH2 on the order of ten or more proteins across.[5]

Within plants and green algae, the photosynthetic thylakoid membranes are contained within 3-10 µm diameter organelles called chloroplasts. Themselves believed to be descended from endosymbiotic cyanobacteria, thylakoid membranes in plants conserve PSI and PSII from their ancestors, but no longer utilize phycobilisomes as their antenna structure. Instead, plants evolved in a similar direction as purple bacteria, with the trimeric light harvesting complex II (LHCII, lighter green circles, $\sim$8 nm diameter)[6] serving as a transmembrane antenna complex arrayed in a two dimensional structure, as depicted in Fig. 1.1(c). Depending on conditions, LHCII can bind to the PSII core, along with other minor LHCs, to form a supercomplex, but free LHCII in the membrane also acts as an antenna similarly to LH2 in purple bacteria.[7,8] Unlike in purple bacteria, however, there exists very little energetic gradient within between LHCII and PSII, with both complexes containing chlorophyll *a* and *b*, which absorb near 670 and 650 nm, respectively, and the energetic landscape is more complicated.[9,10] These PSII and free LHCII complexes are packed closely in the thylakoid membrane, with typical distances between reaction centers on the order of 10 nm or less.[11]

Understanding how nature achieves such high energy transport efficiencies in these varied architectures is of great interest for informing how we may imitate its performance in our own technologies. In this work we take particular interest in longer-range energy transport exhibited in the two-dimensional LHC systems present in purple bacteria and green plants. Unlike the phycobilosome, which presents a fairly intuitive and extensively characterized strategy for light-harvesting, there are still open questions regarding the efficiency of long-range energy transport in these photosyntetic systems. For instance, to what extent are excitations undergoing a purely random walk in green plants, or to what extent is the reaction center acting as an attractor? Which of these possibilities is most important in plants and green algae is unclear, and if the latter is dominant, the mechanism by which it may occur is not fully explored. In general, as will be explored herein, the long-range energy transport between identical chromophores (either within individual complexes or across multiple) remains relatively under-studied, and in this work we aim to explore this scale of photosynthetic light harvesting.

1.2 Energy transfer and transport in photosynthetic light harvesting

Deeply related to the question of how photosynthetic LHCs achieve such high quantum efficiencies is the question of how energy is transferred from chromophore to chromophore in these systems. When a photon is absorbed by a molecule in the vicinity of other optically excitable molecules, there are a number of energy transfer processes that may allow that energy to move between these different molecules, and photosynthetic LHCs take advantage of a number of them. Together, these chromophore-to-chromophore transfer processes give rise to emergent energy transport through the chromophore network to reaction centers.

Broadly speaking, energy transfer processes may be coherent or incoherent.[12] Incoherent transfer occurs when excitations are localized to individual molecules or aggregates, and transfer occurs as discrete “hopping” between sites. Coherent energy transfer, on the other hand, is mediated by the evolution of a superposition of quantum states delocalized over several molecules, where the phase relationship is well-defined over the time scales of the energy transfer.[13] Typically, this is possible when the energy of coupling between chromophores is larger than the thermal fluctuations of the surroundings, or else coupling to the surrounding thermal bath causes dephasing. Interestingly, in photosynthetic systems it is often the case that these coupling are nearly equal (the so-called “intermediate coupling regime”), which gives rise to complex and interesting energy transfer dynamics, such as environmental noise enhancing energy transfer efficiency.[14,15]

At longer distances on the scale of 1-10 nm, energy transfer proceeds via an incoherent interaction known as Förster resonance energy transfer (FRET).[16] Under this model, which is described in more detail in Section 3.3.1.1, energy is transferred from an excited donor molecule to an acceptor molecule in its ground state by a dipole-dipole interaction, with the efficiency decreasing as the sixth power of the distance between the two molecules. For efficient FRET to occur, the molecules must have their transition dipole moments aligned, and there must be overlap between the fluorescence spectrum of the donor and the absorption spectrum of the acceptor.[1]

At distances below ~1 nm, the approximation central to Förster theory, that the coupling between molecules is small and can be treated perturbatively,[12] breaks down, and new transfer processes arise. The close proximity of chromophores in LHCs often results in failure of classical Förster theory to fully describe energy transfer, which has led to the development of semiclassical theories[17] of energy transfer that account for the stronger coupling between nearby chromophores, such as modified Redfield theory[18] and generalized Förster theory.[19]

When there is wavefunction overlap and strong coupling between adjacent chromophores, the electronic system can no longer be described classically, and wavefunction delocalization across many pigments gives rise to coherent energy transfer, where there is prolonged oscillation in the electron density across the system.[12] One such process is Dexter energy transfer,[20] which requires direct wavefunction overlap of the involved chromophores. For example, Dexter energy transfer proceeds by a spin exchange mechanism, allowing spin-forbidden transitions between very close molecules. Dexter transfer is involved in the photoprotective function of carotenoids in photosynthetic systems, where spin-forbidden transitions are required.[21,22] Furthermore, in the LH2 antenna complex of purple bacteria, the B850 ring of bacteriochlorophylls are strongly coupled together, resulting in delocalization across many bacteriochlorophyll molecules and extremely rapid transfer on the order of 100 fs.[1,23]

1.2.1 Emergent energy transport in photosynthetic systems

Together, these energy transfer processes between the many chromophores involved in photosynthetic light harvesting give rise to emergent *transport* of energy, i.e., the ensemble of trajectories taken by excitations through the chromophore network. At this scale, emergent properties become apparent, such as spatial diffusion, i.e., the ensemble motion of many randomly-walking 'particles.' Nanoscopic heterogeneity modifies these transport dynamics,[24] causing effects such as spectral diffusion (i.e., drift in the average energy of the excitation population) when excitations are transported through an energetically heterogeneous environment.[25,26]

Diffusive energy transport varies from incoherent hopping, when the excitations spend almost all of their lifetimes localized on single chromophores and undergo very rapid "hops" between sites, to band-like, where excitations spend most of their time traveling ballistically, interrupted by occasional scattering events.[24] True band-like transport occurs in semiconductors such as silicon, where electrons promoted to the conduction band travel ballistically, while molecular systems often support only incoherent transport. Photosynthetic LHCs are molecular systems, yet are remarkable for achieving extremely high transport efficiencies, in some cases by utilizing coherent effects among chromophores that are close enough to electronically couple to one another more strongly than with FRET.[27,28]

Throughout this work, understanding how the energy transport informs the underlying transfer mechanisms and heterogeneity are a major theme. As will be explained below, transport on the scale, i.e., inter-protein energy transport in photosynthesis, is an understudied regime in photosynthetic light harvesting.

1.3 Challenges with and progress on understanding photosynthetic light harvesting

The photophysics of photosynthesis has been the topic of extensive study in the past century,[29–36] leading to a strong foundation of understanding of the design principles behind the function of LHCs, yet many open and interesting questions remain. Investigation of photosynthetic LHCs presents a variety of challenges that must be overcome in order to fully understand these complex systems.

One major challenge in studying LHCs is the difficulty of working with these samples. Transmembrane proteins are notoriously difficult to isolate and characterize, comprising under 6% of all protein structures in the Protein Data Bank[37] as of July 2024, despite representing 20-30% of the total proteome.[38] To further complicate matters, as discussed previously, LHCs in plants and purple bacteria are composed not of single transmembrane proteins, but of loosely associated super-complexes of many such proteins, which can be difficult if not impossible to isolate. The structure of the PSII supercomplex, for example, was not determined until 2009,[39,40] and even so, an isolated supercomplex itself does not include the many loosely associated LHCII complexes arrayed around it. Furthermore, these intricate protein complexes are difficult to mutate without destabilizing the system, which makes systematic investigation challenging.

Recent advances in structural characterization techniques, particularly in the resolving power of cryo-electron microscopy down to below 3 Å have made structural characterization of the membrane-bound proteins involved in LHCs far more feasible, resulting in increasingly detailed pictures of the structure of these molecular machines.[41–43] A number of mutants of photosynthetic proteins have been developed that, for example, modify the non-photochemical quenching capabilities of plants[44] or alter the morphology of thylakoid membranes.[45] Another approach has been the development of artificial light harvesting constructs to serve as model systems for protein-chromophore interactions that are more easily modifiable than natural systems. One such model is that developed by Prof. Matt Francis' lab based on the tobacco mosaic virus (TMV).[46] This complex presents a stable, disk-shaped protein scaffold that is easily modified to insert chromophores at various sites on the protein. This platform has been used for studying individual protein-complex interactions,,[47,48] as well as (as will be explained in this work) for studying intra-protein energy transfer.[49] It has recently also been expanded to enable multi-complex conjugation to model inter-protein energy transfer.[50] The use of artificial light harvesting complexes to study the fundamental factors important in efficient energy transfer promises an exciting pathway for elucidating mechanisms in photosynthetic light harvesting.

Another challenging aspect of the study of light harvesting complexes is deconvolving the many processes occurring simultaneously. Following photoexcitation, energy transfer occurs through a complex network of chromophores, some spectrally indistinct from one another. Meanwhile any of a number of regulatory mechanisms may interact with the excitation to quench it before it reaches a reaction center. Long-range energy transfer may occur over multiple identical antenna protein subunits, making the problem of how to measure this transfer challenging. One approach to solving this problem has been the development of novel multidimensional spectroscopy techniques,[51–55] effectively distributing the crowded spectrum onto multiple dimensions, which has allowed detailed mapping of energy transfer pathways within photosynthetic protein complexes.[56] On another front, computational models capable of modeling inter-protein energy transfer have been developed and show promising agreement with fluorescence data, highlighting the role of the diffusion length as a tuning control for light harvesting efficiency.[8,57]

The recent development in the Ginsberg lab of time-resolved interferometric scattering microscopy[58] has for the first time allowed widefield spatiotemporal measurement of energy migration in natural light harvesting complexes. This technique's versatility has allowed investigation of charge carrier migration in inorganic and organic semiconductors,[58–60] charge and heat transport in two-dimensional materials,,[61] and subdiffusive heat transport in gold nanoparticle films.[62,63] Now, we have developed the capability to apply this powerful technique to natural LHCs, laying the groundwork for future exploration of long-ranged energy transport in these systems.

1.4 Our novel approaches to studying photosynthetic light-harvesting

In this work, we present a series of studies on photosynthetic light-harvesting by novel means. First, we explore the role of disorder in energy transfer in a model light harvesting complex based on the tobacco mosaic virus.[49] By studying a model complex, we have far more control over the system than in natural light-harvesting complexes, which are difficult to work with systematically as detailed above. We used transient absorption anisotropy spectroscopy to study energy transfer in these complexes, a technique which can probe transfer between spectrally identical chromophores. By developing a kinetic Monte Carlo simulation to model the observed anisotropy decay, we are able to explore the role of disorder on energy transfer in this system.

Second, we utilize time-resolved interferometric scattering microscopy to image exciton migration following photoexcitation of a thylakoid membrane by a focused laser pulse. These first-of-their-kind measurements required significant improvements to our microscope apparatus and sample preparation methods, but have yielded promising initial measurements that allow us to directly image exciton migration in these systems.

By applying an old technique to a novel model light harvesting complex, and a novel technique to a natural photosynthetic system, we detail herein new understanding of the factors important for achieving efficient photosynthetic light-harvesting.

Chapter 2

Transient Absorption Spectroscopy & Polarization Anisotropy

To study the energy transfer processes occuring in LHCs on time scales of picoseconds or faster, we require a technique capable of measuring such fast events. Transient absorption (TA) spectroscopy is a powerful nonlinear spectroscopy that allows the determination of how the absorption spectrum of a sample changes over time following photoexcitation. Herein we delve into the fundamental concepts behind TA spectroscopy and pump-probe techniques in general.

Furthermore, we will explore transient absorption anisotropy (TAA) spectroscopy, an extension of TA spectroscopy that allows probing of the orientation of excited species and how the orientation of that population evolves after photoexciation. This technique is invaluable for measuring energy transfer processes between otherwise spectrally indistinguishable chromophores, as is necessary for studying the long-range energy transfer processes in photosynthesis.

In Chapter 3, we will detail the study of a model LHC via TAA spectroscopy that illuminated the role that disorder plays in long-range energy transfer. To accomplish this goal, we constructed a high signal-to-noise ratio (SNR) TAA apparatus, which we will detail below.

In Section 2.1 we describe the principles of transient absorption spectroscopy, then in Section 2.2 we go on to describe transient absorption polarization anisotropy spectroscopy as a method for measuring energy transfer. Last, in Section 2.3 we detail the implementation of a high signal-to-noise ratio TAA apparatus.

2.1 Transient Absorption Spectroscopy

When an electron inside of an atom, molecule, semiconductor, protein, or any other chemical system absorbs a photon and enters an energetically excited state, typically within a few nanoseconds it will return to its ground state, releasing that energy in some form, such

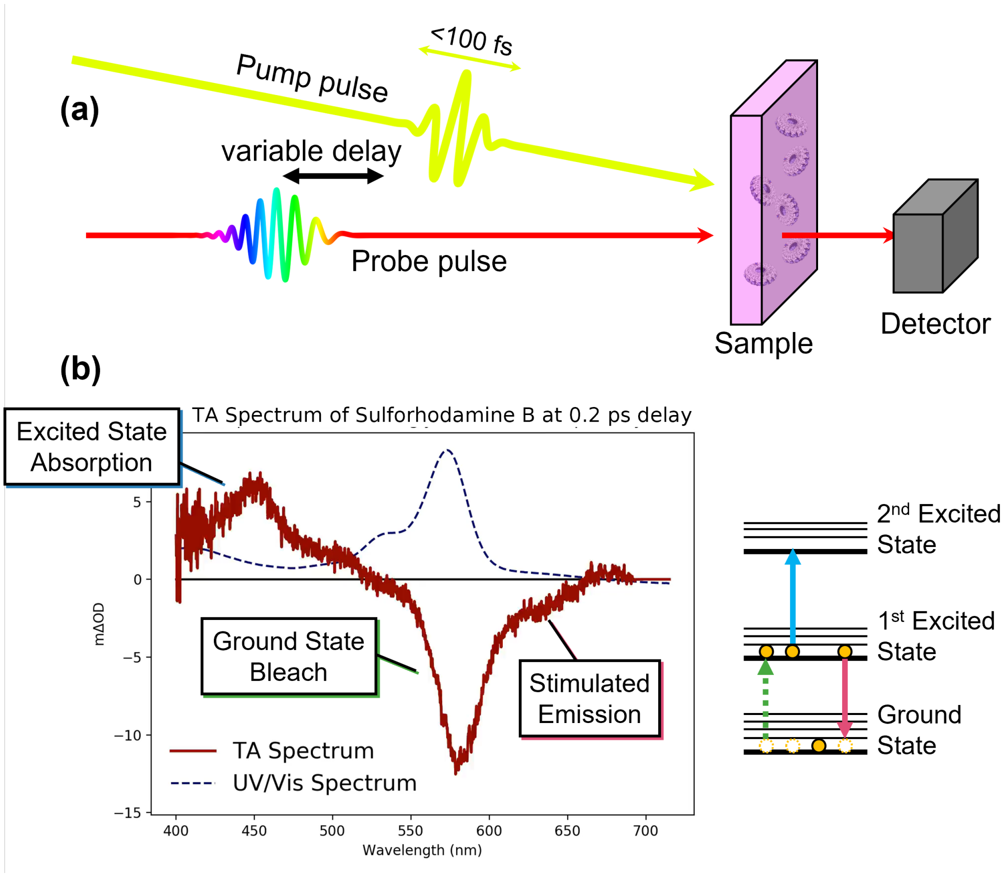

Figure 2.1: Schematic explanation of transient absorption spectroscopy. (a) A simplified diagram of a typical TA setup, where a pump laser pulse (yellow) excites a sample shortly before a probe pulse (red/rainbow) arrives at the sample, and, following transmission through the sample, is incident on a detector. (b) TA spectrum of sulforhodamine B pigment in water (maroon curve) pumped at 570 nm, demonstrating the three common types of TA spectral features identified by callout boxes, with the ground-state UV/Vis spectrum also shown (blue dashed curve) to illustrate position of the ground state absorption peak. (c) Simplified Jablonski diagram demonstrating the transitions giving rise to the ground state bleach (green), excited state absorption (blue) and stimulated emission (magenta).

as light or heat. While this process is over in in less than one millionth of the blink of an eye, it is constantly occurring around us, allowing our eyes to perceive light and color, driving plants' ability to create sugar out of sunlight and water, and powering the display of the device you're using to read this work (or perhaps the pigments of the ink you used to print it). Transient absorption spectroscopy is perhaps the most commonly-used nonlinear spectroscopy to characterize this ultrafast process by measuring how the absorption spectrum of a system evolves over time in the femtoseconds-to-nanoseconds (or longer) following photoexcitation. In essence, the technique helps us answer the question: after an electron absorbs a photon and enters an excited state, what is the energetic pathway (or pathways) that that electron takes to return to the ground state, and how does the environment change in response to the perturbation?

TA spectroscopy can be understood from the basis of ordinary linear absorption (i.e., UV/Vis) spectroscopy. In ground-state linear absorption spectroscopy, light with some intensity spectrum $I_0(\lambda)$ is incident on a sample, and the intensity spectrum $I(\lambda)$ of light that transmitted through the sample is measured by dispersing it at a spectrometer. The optical density $OD(\lambda)$ of the sample at a given wavelength is then defined by the following expression:

$$OD(\lambda) = -\ln\left(\frac{I(\lambda)}{I_0(\lambda)}\right) \tag{2.1}$$

In TA spectroscopy, the goal is simply to measure the change in OD right after the sample has been illuminated by a light pulse.

To accomplish this objective, the continuous light source is replaced by a pulsed one, typically an ultrafast pulsed laser with pulse widths down to tens or even single femtoseconds. By doing so, the beam, which we will refer to as the "probe" beam is shown as the red/rainbow beam in the diagram in Fig. 2.1 (a), measures only a very brief "snapshot" of the sample's optical density, similar to taking a flash photo in a dark room. To complete the setup, a second pulsed laser source is added that typically has a narrow spectrum tuned to an optical resonance of the sample. We call this beam the "pump," as its role is to promote some portion of the sample, typically on the order of 0.01-1%, into an excited state, and it is represented as the yellow beam in Fig. 2.1 (a). By synchronizing the repetition frequencies of the pump and probe pulses (often by generating them from the same laser source) and timing their arrival at the sample such that the probe pulse arrives only just after the pump pulse, the intensity spectrum $I_{\text{on}}(\lambda)$ of the probe pulse will reflect the absorption spectrum of this mixture of ground and excited state sample. To remove the contribution from the ground state portion, the pump beam is modulated, or "chopped," so that every other measurement of the probe is taken with the pump blocked. Therefore, the intensity spectrum $I_{\text{off}}(\lambda)$ of the probe pulse corresponds only to the ground state (linear) absorption. With this pair of measurements we compute the change in optical density $\Delta OD = \Delta OD_{\text{on}} - \Delta OD_{\text{off}}$ by making use of the approximation that the intensity of the probe is constant, i.e., $I_{0,\text{on}} \approx I_{0,\text{off}}$:

$$\Delta OD(\lambda) = -\ln\left(\frac{I_{\text{on}}(\lambda)}{I_{0,\text{on}}(\lambda)}\right) + \ln\left(\frac{I_{\text{off}}(\lambda)}{I_{0,\text{off}}(\lambda)}\right) \approx -\ln\left(\frac{I_{\text{on}}(\lambda)}{I_{\text{off}}(\lambda)}\right) \tag{2.2}$$

This approximation is justified because the relative standard deviation over time of the power of the laser sources used for the probe are typically specified to within a few percent, such that the measurement-to-measurement intensity may be treated as constant. Last, we can vary the time delay t between the arrival of the pump and probe to obtain individual $\Delta OD(\lambda, t)$ spectra for a set of time delays, thus creating the measurement of how the excited-state spectrum evolves over time.

2.1.1 Understanding transient absorption spectral features

Unlike in a ground-state (linear) absorption spectrum, in a TA spectrum there can be both positive and negative peaks, representing features of the excited state that increase and decrease absorption, respectively, relative to absorption in the ground state. For a molecular system, there are typically three types of features that appear in a TA spectrum, an example of each of which can be seen in the TA spectrum (maroon curve) of sulforhodamine B shown in Fig. 2.1(b). The first is the *ground state bleach*, which is a result of the pump reducing the concentration of ground state species (by exciting them) that can absorb the probe, as indicated by the dashed green line in the Jablonski diagram shown in Fig. 2.1(c). This reduction in absorption results in a negative feature that seems to "mirror" the ground state absorption spectrum. In Fig. 2.1(b), the ground state bleach is the strong negative signal near 570 nm, occurring opposite the peak in the ground state UV/Vis spectrum (blue dashed curve). The second common spectral feature is an *excited state absorption*, which is a positive feature arising from the absorption of probe light by species already excited by the pump, to populate even higher-energy excited states, as indicated by the blue arrow in 2.1(c). As indicated by the blue callout box, sulforhodamine B exhibits an excited state absorption at around 450 nm. The third type of feature is due to *stimulated emission*, whereby excited species relax to the ground state by coherently adding a photon to the transmitting probe field, as illustrated by the magenta arrow in 2.1(c). This occurrence increases the intensity of the detected field and thus appears to decrease absorption—hence, this signal presents as a negative ΔOD, which can be seen as the "shoulder" extending out to 650 nm in 2.1(b). In almost all cases, the peak of the stimulated emission appears lower in energy than the ground state bleach due to the Stokes' shift; the position(s) of excited state absorption peak(s) are determined by the energy states accessible from the pumped excited state, but otherwise may appear anywhere with respect to the two other types.

2.1.2 Time resolution

In a time-resolved measurement, the time resolution is limited by the so-called instrument response function (IRF), which is a function $IRF(t)$ of the pump-probe time delay t that

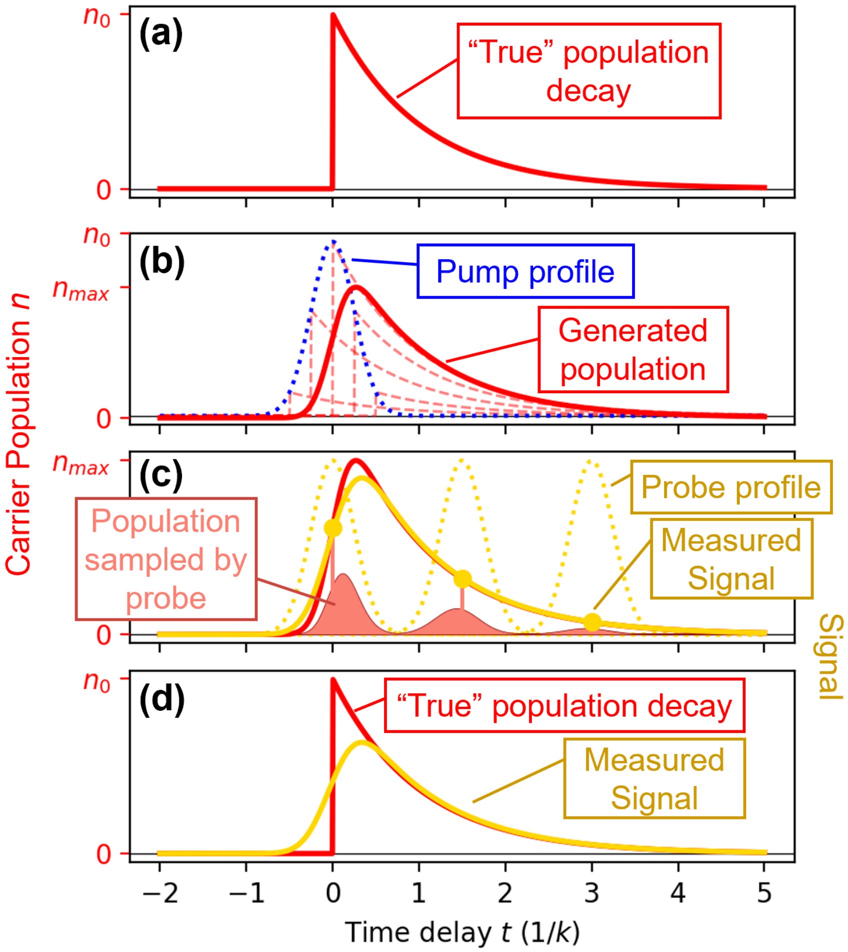

Figure 2.2: Visual explanation of the instrument response function for a hypothetical instrument. (a) The "true" population dynamics of a hypothetical impulsively excited species. (b) The temporal averaging caused by the finite pump profile width (blue dotted curve) leads to a generated population (solid red) that is smoothed relative to the "true" population. (c) The probe pulse samples an average of the generated population (light red filled peaks) due to finite pulse width (green dotted curve), resulting in further temporal averaging in the measured signal (green curve). (d) Comparison of "true" population dynamics (red) and the measured signal (green).

gives the signal $S(t)$ measured by the instrument in response to a hypothetical perfectly impulsive stimulus, i.e., the Dirac delta function $\delta(t)$. Physically, the IRF is primarily a result of the finite durations of the pump and probe pulses, which causes the instrument to temporally average over the response of the sample. We can consider the hypothetical case of a population n_δ of carriers that undergoes exponential decay with rate k following excitation by a perfectly impulsive pump that generates an initial population of n_0 at $t = 0$, in other words:

$$n_\delta(t) = H(t) \cdot n_0 e^{-kt} \tag{2.3}$$

where $H(t)$ is the Heaviside step function. This population is plotted in Fig. 2.2(a). Then, we can consider the same system excited by a pump pulse whose temporal profile $I_{pu}(t)$ is Gaussian with finite width σ_{pu}. In this case, at time delay t relative to the peak of the pump pulse, the population will consist of carriers excited not only exactly t temporal units ago, but will be a mixture of carriers excited slightly before and after that time due to the finite duration of the pump. Specifically, we can consider the subpopulation of carriers which were excited some time τ relative to the peak of the pump pulse. The initial population is modulated by the amplitude of the pump at that time τ, and the decay of this subpopulation is advanced (or retarded) by that time τ, giving a temporal profile of:

$$n_\tau(t) = I_{pu}(\tau) \cdot n_\delta(t - \tau). \tag{2.4}$$

To extend from this subpopulation to the entire population present at time t, we must integrate this equation over all the subpopulations generated at different times τ:

$$n(t) = \int_{-\infty}^{\infty} I_{pu}(\tau) \cdot n_\delta(t - \tau) d\tau = I_{pu}(t) * n_\delta(t), \tag{2.5}$$

which demonstrates that the carrier population present at time t following the pump peak is equal to the convolution of the “true” impulsive carrier population and the pump pulse’s temporal intensity profile. This is demonstrated in Fig. 2.2(b), where individual instances of n_τ are plotted as light red dashed curves, and the resulting convolution is plotted as a red curve.

Now, we would like to measure the carrier population $n(t)$ at time t following the excitation by the pump pulse, and for similar reasons we find that the probe pulse, with its finite width, is unable to sample the population exactly at time t. Instead, it measures a weighted average of $n(t)$ near the peak of the probe pulse, weighted by the probe’s intensity at an offset in time τ, which is shown as light red filled peaks in Fig. 2.2(c). In effect, for the same reasons as above, the signal $S(t)$ that we observe is another convolution, this time with the temporal profile of the probe, $I_{pr}(t)$:

$$S(t) = I_{pr}(t) * n(t) = I_{pr}(t) * I_{pu}(t) * n_\delta(t) \tag{2.6}$$

as shown as the green curve in Fig. 2.2(c). As can be seen in the figure, this effect is relatively small due to the similar durations of the pump and probe pulses. A comparison between the "true" impulsive population decay and the signal measured by an instrument with a Gaussian IRF is shown in Fig. 2.2(d).

Now, rather than a carrier population with a finite exponential decay, we can consider a hypothetical population of carriers which undergo immediate decay, i.e., a perfectly impulsive stimulus $n_\delta(t) = \delta(t)$. Then, using the definition of the IRF above as the signal measured in response to such an impulsive stimulus, we find a definition of the IRF in terms of the pump and probe temporal profiles:

$$IRF(t) = I_{pr}(t) * I_{pu}(t) * \delta(t) = I_{pr}(t) * I_{pu}(t), \tag{2.7}$$

and furthermore we can see that the signal $S(t)$ measured for an arbitrary system can be expressed as a convolution of the IRF and the "true" carrier population $n_\delta(t)$:

$$S(t) = IRF(t) * n_\delta(t). \tag{2.8}$$

This definition of the IRF ignores some other sources of temporal averaging that may be present in the instrument, such as jitter in the delay between pump and probe pulses, but these other sources tend to be negligible in comparison to the pulse widths. For the diode laser-based time-resolved microscopy described in Chapter 4, for example, the jitter is specified to be under 3-5 ps, two orders of magnitude smaller than the 150-ps laser pulse widths.

This temporal averaging from the IRF is ultimately what limits our ability to resolve ultrafast processes. To understand this intuitively requires one only to visualize the effect of convolving an exponential decay with a finite-width Gaussian. For a more rigorous explanation, we can use the convolution theorem, which states that the convolution of two functions is equivalent to multiplying the two functions together in Fourier space:

$$f(t) * g(t) = \mathcal{F}^{-1}\left\{\mathcal{F}\{f\} \cdot \mathcal{F}\{g\}\right\}, \tag{2.9}$$

where $\mathcal{F}$ denotes the Fourier transform. In the common case where the pump and probe pulses both have Gaussian profiles in time with respective widths σ_{pu} and σ_{pr} and are the main contributors to the IRF, their convolution, and thus the IRF, will be Gaussian, with a resulting width σ_{IRF} obtained by addition of their two widths in quadrature:

$$\sigma_{\mathrm{IRF}}^2 = \sigma_{pu}^2 + \sigma_{pr}^2. \tag{2.10}$$

Because the Fourier transform of a Gaussian function is Gaussian, when we take a measurement and convolve our "true" signal with the IRF, in Fourier space we are multiplying the Fourier transform of the "true" signal with a Gaussian envelope. This suppresses high-frequency components, which are essential for expressing a quickly-changing signal, making it increasingly difficult to resolve faster decays as their lifetimes approach the width of the IRF. This constrains the time resolution, i.e., the fastest decay that would be resolvable, to approximately the full width at half maximum of the IRF.

2.2 Transient Absorption Anisotropy Spectroscopy

Transient absorption anisotropy (TAA) spectroscopy is an extension of TA spectroscopy in which the polarization anisotropy of the sample is measured as a function of time following photoexcitation by the pump laser pulse. Polarization anisotropy is a measure of the how a sample's absorption changes as a function of the polarization of the electric field of the probe pulse. In TAA, the pump laser pulse is sufficiently weak that we may make the dipole approximation and treat the molecule as a point dipole. Under this approximation, the probability P of a molecule absorbing light from a linearly-polarized, oscillating electric field is proportional to the square of the dot product of the electric field $\vec{E}$ and the transition dipole moment (TDM) $\vec{\mu}$ for the transition between the ground and excited state:

$$P \propto \left|\vec{\mu} \cdot \vec{E}\right|^2 \propto \cos^2\theta, \tag{2.11}$$

where θ is the angle between $\vec{E}$ and $\vec{\mu}$. In other words, a polarized probe beam will preferentially measure molecules whose TDMs are aligned to its polarization. In linear absorption spectroscopy of molecular species in solution, this probability is not usually considered, because the molecules on which the probe beam is incident have completely random orientations, and thus absorption does not depend on the probe's polarization. In a TA measurement, however, the population we are probing is not the perfectly randomized ground-state ensemble, but the excited-state species that have just been excited by a linearly polarized pump pulse. Just as the probe will preferentially interact with molecules with TDMs parallel to the probe polarization, the population of excited molecules resulting from excitation by the pump laser pulse *will* be preferentially oriented such that the TDM of the pumped transition is preferentially aligned parallel to the pump polarization (with the probability distribution given in Eqn.2.11), which is referred to as photoselection. Therefore, if we probe the sample with a probe that is polarized parallel to the pump we will measure one change in OD $\Delta OD_{\parallel}$, while if the two are perpendicularly polarized we will measure a different change, $\Delta OD_{\perp}$. The anisotropy r parameterizes the difference between these two signals and is computed by the following expression:[31]

$$r = \frac{\Delta OD_{\parallel} - \Delta OD_{\perp}}{\Delta OD_{\parallel} + 2 \cdot \Delta OD_{\perp}}. \tag{2.12}$$

In other words, it is the difference between the two differential ODs normalized by the total $\Delta OD = \Delta OD_{\parallel} + 2 \cdot \Delta OD_{\perp}$, where the perpendicular term is doubled to reflect the fact that there are two axes perpendicular to the pump polarization (we only measure along one of them, but by symmetry they must be equal, assuming the pump and probe beams are coplanar and the pump polarization is normal to this plane).

The anisotropy is a useful parameter because it reports on the overall orientation of the TDMs of the excited species measured by the probe, which may evolve over time as those TDMs change. To see this phenomenon, another expression for anisotropy can be derived[64] by considering the electric field of a population of radiating dipoles with angle θ

relative to a z-axis that is parallel to the polarization of the pump pulse field, which gives the characteristic Legendre polynomial:

$$r = \frac{3\langle \cos^2(\theta) \rangle - 1}{2} \tag{2.13}$$

where $\langle \cdots \rangle$ denotes averaging over the population. While this expression appears to have a maximal anisotropy of 1, it is not possible to achieve this experimentally, as the population excited by the pump is not perfectly aligned with it but rather has a probability distribution given by Eqn. 2.11. Solving $\langle \cos^2(\theta) \rangle$ for this distribution gives a value of 3/5, which allows for a maximal anisotropy of 0.4 in practice.[64] The other factor that must be considered is that the TDM that is probed is not always exactly parallel to that which was pumped, which has an additional depolarizing effect. Taken together, these two considerations give the so-called "intrinsic" anisotropy r_0:[64]

$$r_0 = \frac{2}{5} \cdot \frac{3\cos^2\beta - 1}{2}, \tag{2.14}$$

where β is the angle between the pumped and probed TDMs within the molecule. Note the distinction between β here and θ in Eqn. 2.13: β denotes the angle between the pumped and probed TDMs in the frame of reference of the molecule, while θ denotes the angle between the pumped and probed TDMs in the lab frame, which is further changed following excitation by processes such as rotation diffusion and energy transfer. The time-dependent polarization anisotropy measured in TAA is then given in full as:

$$r(t) = r_0 \cdot r_d(t), \tag{2.15}$$

where $r_d(t)$ is a function capturing the time-dependent behavior of the anisotropy following photoexcitation. While $r_d(t)$ could in theory take any value between 1 and -1/2 per Eqn. 2.13, most commonly it is an exponentially decaying function with unity amplitude, with maximal (intrinsic) anisotropy appearing at early times. The full function $r(t)$, however, gradually decays as processes such as rotational diffusion or energy transfer depolarize the TDM population. The exact form this decay takes informs us about the processes that are causing the depolarization. For example, a small molecule undergoing rotational diffusion due to Brownian motion will exhibit a monoexponential TAA decay from r_0 to 0 with a lifetime corresponding to the rotational diffusion constant,,[65] while energy transfer around a ring of identical molecules with maximal intrinsic anisotropy whose TDMs lie in the plane of the ring will exhibit an anisotropy decay from 0.4 to 0.1.[66]

2.2.1 Eliminating polarization effects: finding the "magic angle"

To illustrate how TA anisotropy manifests in practice, using Eqns. 2.12 and 2.15 we compute the $\Delta OD(t)$ curves for a hypothetical species exhibiting a 3 ps TA lifetime and an exponential anisotropy decay with a 1.5 ps lifetime, starting with an intrinsic anisotropy of 0.4. At short

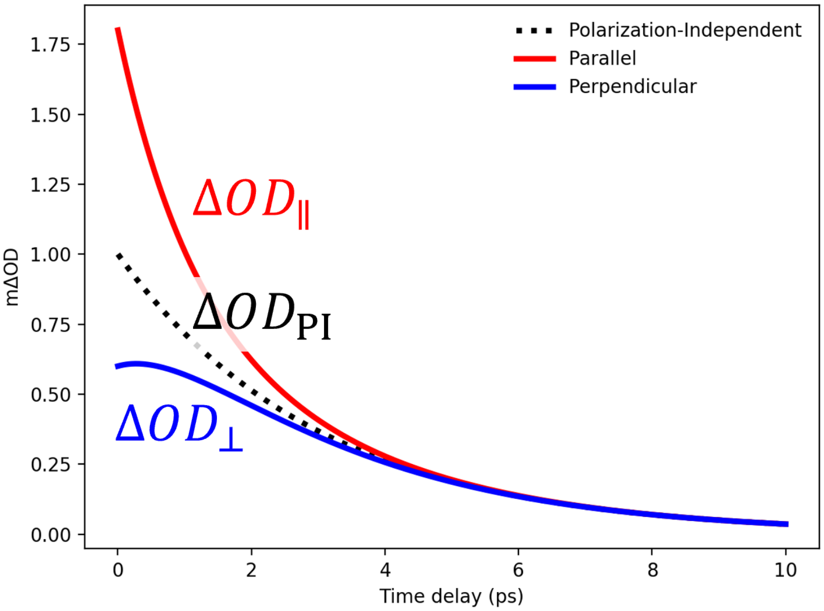

Figure 2.3: Simulated TA data for a hypothetical species with a single TA lifetime of 3 ps, an anisotropy lifetime of 1.5 ps, and an initial anisotropy of 0.4. Shown are the ΔOD curves that would be measured when probing parallel (red curve) or perpendicular (blue curve) to the pump polarization. The polarization-independent ("magic-angle") TA decay kinetics are also shown (black dotted cure).

time delays, when probing parallel to the pump polarization (red curve) the measured ΔOD is higher than when probing perpendicular to the pump polarization (blue curve). At longer time delays, however, as the anisotropy decays, the difference decreases until the two converge to practically the same value.

This effect highlights that it is important to consider polarization effects even when performing standard TA spectroscopy. In a standard TA measurement, the goal is to measure the TA lifetime of the molecule, not its depolarization. Thus, the choice of probe polarization is important, as depolarization could be incorrectly interpreted as excited state decay. In fact, to remove any depolarization artifacts, the polarization-independent ΔOD_{PI} that ought to be measured in a standard TA experiment is the average ΔOD over all three polarization axes:

$$\Delta OD_{\mathrm{PI}} = \frac{1}{3}(\Delta OD_{\parallel} + 2 \cdot \Delta OD_{\perp}). \tag{2.16}$$

To avoid having to measure two polarizations for a standard TA measurement, the solution is to set the angle θ between the pump and probe polarizations such that the pump laser pulse generates an excited population that is equally biased parallel and perpendicular to the probe polarization. This angle, termed the "magic angle," is derived by solving for the root of the Legendre polynomial in Eqn. 2.13, which gives a θ value of $\sim 54.7°$.[64] TA spectroscopy can thus be performed in a single measurement, and the polarization-independent TA decay is termed the "magic-angle" decay for this reason.

2.2.2 Learning about energy transfer from TAA decays

Energy transfer between two differently-oriented chromophores changes the orientation of the probed TDM, because following the transfer, the excitation resides on a different molecule than the one the pump excited. This leads to orientational decorrelation and thus a measurable depolarization of the transient absorption signal. TAA spectroscopy is thus a powerful tool for measuring energy transfer in light harvesting complexes. In particular, a major strength of TAA spectroscopy is that it can probe energy transfer between any two chromophores that are not oriented identically, even when they are otherwise identical, whereas in standard TA spectroscopy, this would not present a measurable change in the $\Delta OD(\lambda)$ spectrum.

In LHCs there are many such cases of otherwise identical chromophores that participate in energy transfer to acheive efficient light harvesting. Polarization anisotropy has been essential in understanding the rate of energy transfer in such systems, for example the use of fluorescence anisotropy by Bradforth *et al.* to study energy transfer between B800 and B850 bacteriochlorophyll molecules in LH2 complexes of purple bacteria[66] and of TAA spectroscopy by Gaab and Bardeen[67] to study energy transfer in conjugated polymers. In such studies, the form that the anisotropy decay $r(t)$ takes informs us of the nature of the energy transfer pathways available to excitations at the microscopic level.

In the case of a perfectly homogeneous system (i.e., the transfer rates between any chromophore and its neighbors are always the same), we expect to observe an exponential decay, as Bradforth *et al.* demonstrated in simulations of perfectly ordered rings of chromophores,[66] as the depolarization is occurring equally and independently for every excitation in our detection volume. Oftentimes, however, the anisotropy decay will present as a nonexponential decay, which is a sign of inhomogeneity at the microscopic level. Indeed, the functional form of the anisotropy decay is directly related to the distribution of transfer rates within the system.[68] In work presented in the Chapter 3, we use these principles to apply TAA spectroscopy to the study of energy transfer in a model LHC, which first required the construction of a TAA spectroscopy apparatus with acceptable SNR for these challenging measurements.

2.3 Developing a high signal-to-noise ratio TAA apparatus

Transient absorption anisotropy measurements are challenging due to the necessity of very high SNR. This challenge arises because anisotropy is a ratiometric measure, and so, as the total TA signal (i.e., the denominator of Eqn.2.12) decays to 0, any noise present becomes greatly amplified when dividing by small near-zero quantities.[69] Indeed, TAA spectroscopy studies are less commonplace in the literature than fluorescence anisotropy, likely owing to the difficulty of achieving the requisite SNR in a technique that is not background-free. We now detail the reconfiguration of the pre-existing TA spectroscopy apparatus that was necessary for the collection of high SNR TAA data on artificial light harvesting complexes whose measurements are described in Chapter 3.

The apparatus was originally used to perform ultrafast TA measurements on a homebuilt transient absorption apparatus reported previously.[47,48] An 80 MHz mode-locked Ti:sapphire Coherent Vitara oscillator seeds a Ti:sapphire Coherent Legend regenerative amplifier that outputs 800 nm, 80 fs pulses at a repetition rate of 5 kHz and a total power of 5 W. The fundamental beam is split to generate the pump and the probe beams. Along the pump path, we generate wavelength-tunable, 100 fs pump pulses in a home-built noncollinear optical parametric amplifier[47,70] followed by a dual prism compressor and a chopper wheel for pump-on/pump-off modulation. The chopped pump beam then enters a retroreflector on a 250 mm linear delay stage, allowing up to 1.6 ns of delay. The pump then passes through a $\lambda/2$ waveplate and a Glan-Thomson polarizer (Thorlabs GL10A) to allow variable attenuation to a desired fluence, and is finally focused by a spherical mirror to a $1/e^2$ diameter of 330 µm onto the sample. On the other path we generate the white-light probe by focusing the 800 nm fundamental beam into a CaF_2 crystal that is continuously rastered back and forth to avoid burning.[71] The probe beam is collimated by a 90° off-axis parabolic mirror and passed through a 750 nm wavelength shortpass filter to remove 800 nm light from the fundamental. The probe is next focused by a spherical mirror to a $1/e^2$ diameter of 90 µm onto the sample, overlapping the pump. The sample is contained in a 1 mm path length quartz cuvette (Starna Cells, 21-Q-1) that is linearly rastered back and forth perpendicular to the probe beam propagation to mitigate sample bleaching. Beyond the sample, the probe is passed through an aperture to block pump light before being collected by a lens and focused into a fiber-optic coupler attached to a fiber-coupled spectrometer (OceanOptics USB-4000).

Initially, the setup was modified to introduce TAA capabilities by addition of a second $\lambda/2$ waveplate on a motorized rotation stage (Thorlabs, ELL14) following the waveplate-polarizer attenuator in the pump path, as shown in Fig. 2.4(a). This addition afforded automated control of the pump polarization, allowing spectrally-resolved TA anisotropy measurements by collecting two sequential TA measurements at each time delay, rotating the pump polarization 90° between each by means of the motorized waveplate. While retaining the spectral resolution of the original setup is a strength of this setup, as it would allow simultaneous characterization of the anisotropy of all spectral features, a major drawback of this approach is the reduced rate of data acquisition. Even excluding additional overhead incurred due to the time spent rotating the waveplate (which was minimized by the use of a high-speed motorized mount), at best this approach doubles the amount of time required to collect a scan. Because the SNR decreases by the square root of the number of averaged measurements, halving the number of measurements achievable in a given amount of time reduces the SNR achievable in that amount of time by a factor of $\sqrt{2}$, all other factors being equal.

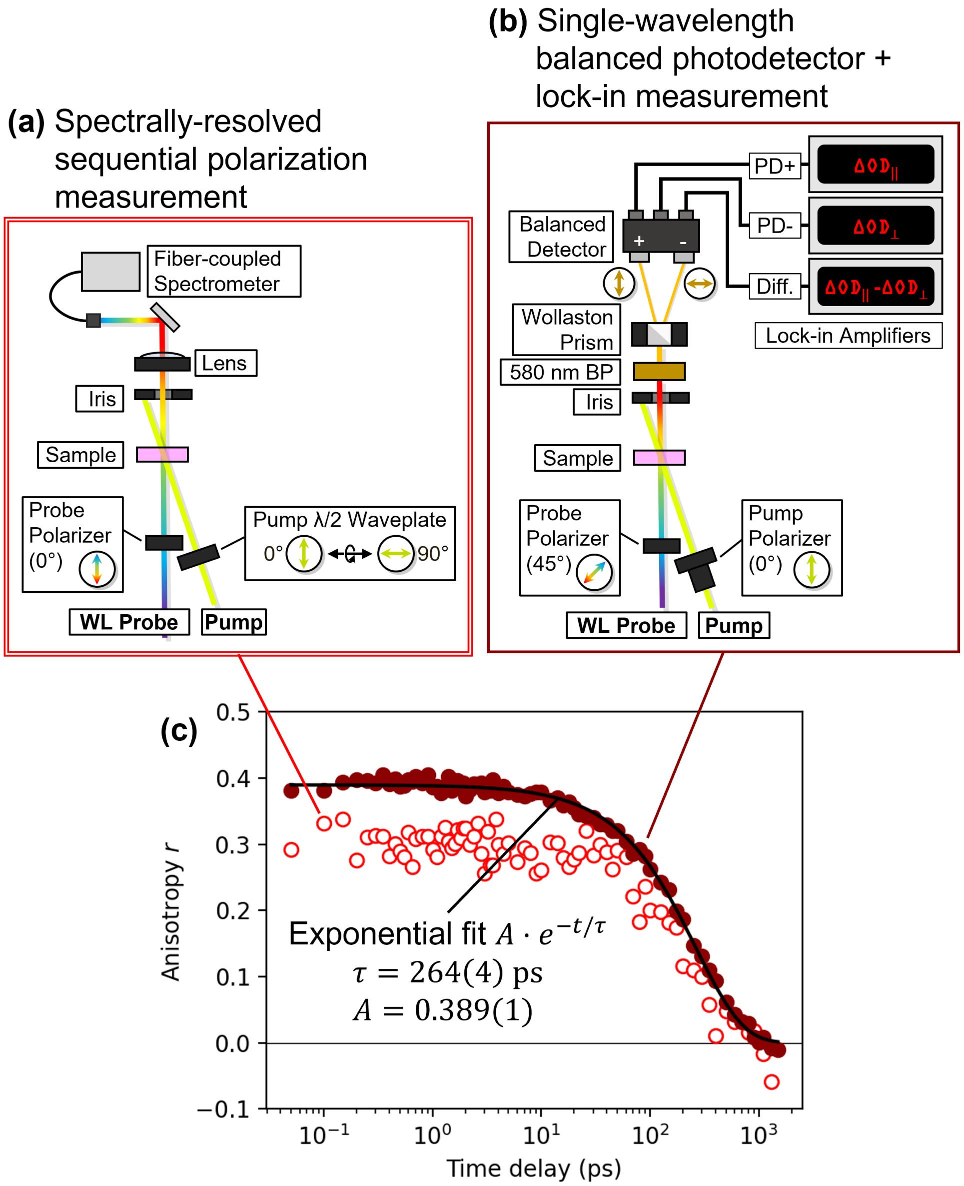

Figure 2.4: Transient absorption anisotropy configurations. (a) Spectrally-resolved, sequential polarization TAA approach, with motorized rotation mount to control pump polarization. (b) Single-wavelength balanced photodetector TAA setup with lock-in detection. (c) Comparison of measured anisotropy of ground state bleach of sulforhodamine B with spectrally-resolved setup (outlined dots) and single-wavelength setup (filled dots).

To overcome these limitations, we implemented a different approach that uses single-wavelength detection and lock-in amplification to greatly increase the SNR, at the expense of losing spectral resolution. The polarization of the pump and probe are set at 45° relative to one another with a the Glan-Thompson prism polarizer and a linear film polarizer (Thorlabs, LPVIS050), respectively, placed immediately before the sample to avoid any depolarizing effects of reflection. Following the sample, a series of irises removes as much scattered light as possible, and a 580 ± 5 nm bandpass filter selects the measurement wavelength. Following the bandpass filter, a Wollaston prism (Thorlabs WP 10-B) rotated 45° relative to the probe polarization splits the probe beam into its two polarization components, which are incident on the two photodiodes of a Thorlabs PDB210 balanced photodetector (BPD) and measured via lock-in amplification. Further details of this configuration follow, but first, the result of this change is illustrated in Fig. 2.4(c), with marked SNR improvement in the scan taken on the single wavelength setup (dark red filled points) in comparison to the spectrally-resolved setup (red open points). The latter also took over three times as long to collect. The initial anisotropy also appears higher in the new apparatus, which is likely a result of the more effective filtering of scattered pump light by the bandpass filter, which otherwise reduces the apparent relative difference in amplitude of the transient signal between the pump-on and pump-off measurements.

The BPD outputs three voltage signals P_+, P_-, and D, respectively proportional to the intensities of the parallel and perpendicular probe components and their difference. We measure these values by lock-in amplification referenced to the frequency of the chopper, yielding differential (pump-on minus pump-off) values ΔP_+, ΔP_-, and ΔD. With these three quantities we compute the TAA signal, as detailed below.

2.3.1 Balanced Photodetector Transient Absorption Anisotropy

We measure the transient difference between pump-on and pump-off of the three signals from the BPD using three Stanford Research Systems SR830 lock-in amplifiers. The lock-in amplifiers are referenced to the chopping frequency of the pump, which was set to 1/8 of the laser repetition rate, i.e., 625 Hz. Thus we measure three quantities in the TAA experiment, each proportional to differences between beam intensities with the pump on ($I_{X,\mathrm{on}}$) and the pump off ($I_{X,\mathrm{off}}$) of the X polarization component (parallel, $\|$, and perpendicular, $\perp$): the two photodiode signals $\Delta P_+ \propto I_{\|,\mathrm{on}} - I_{\|,\mathrm{off}}$ and $\Delta P_- \propto I_{\perp,\mathrm{on}} - I_{\perp,\mathrm{off}}$, and the difference signal $\Delta D \propto (I_{\|,\mathrm{on}} - I_{\perp,\mathrm{on}}) - (I_{\|,\mathrm{off}} - I_{\perp,\mathrm{off}})$. The difference signal from the BPD is pre-amplified with an internal low-noise transimpedance amplifier, specified at a very low noise-equivalent power of $2.2\,\mathrm{pW}/\sqrt{\mathrm{Hz}}$, which allows much greater SNR when the overall beam intensities are weak by performing the subtraction in hardware rather than incurring read error and quantization error prior to performing the subtraction in software. Due to this amplification, however, the proportionality constant for ΔD differs from that of ΔP_+ and ΔP_- by some gain factor G, which we measure during an experiment by taking the ratio $\frac{\Delta D}{\Delta P_+ - \Delta P_-}$.

For each polarization component, the differential optical density can be expressed in terms of probe intensities, as expressed in Eqn. 2.1. For small changes in OD, such as the $\leq 10^{-3}$

changes observed in a typical TA measurement, we can make the linear approximation:

$$\ln \frac{I_{\text{off}}}{I_{\text{on}}} \approx -\frac{I_{\text{on}} - I_{\text{off}}}{I_{\text{off}}}. \tag{2.17}$$

Substituting this approximation into the definition of TA anisotropy given in Eqn. 2.12, we arrive at:

$$r \approx \frac{\frac{I_{\parallel,\text{on}} - I_{\parallel,\text{off}}}{I_{\parallel\text{off}}} - \frac{I_{\perp,\text{on}} - I_{\perp,\text{off}}}{I_{\perp\text{off}}}}{\frac{I_{\parallel,\text{on}} - I_{\parallel,\text{off}}}{I_{\parallel\text{off}}} + 2 \cdot \frac{I_{\perp,\text{on}} - I_{\perp,\text{off}}}{I_{\perp\text{off}}}}. \tag{2.18}$$

Last, because we carefully set the polarization of the probe such that the pump-off intensities of the two polarization components are equal, we can make the approximation that $I_{\parallel,\text{off}} \approx I_{\perp,\text{off}}$, and thus our expression becomes:

$$r \approx \frac{(I_{\parallel,\text{on}} - I_{\parallel,\text{off}}) - (I_{\perp,\text{on}} - I_{\perp,\text{off}})}{(I_{\parallel,\text{on}} - I_{\parallel,\text{off}}) + 2(I_{\perp,\text{on}} - I_{\perp,\text{off}})}. \tag{2.19}$$

This can now be rewritten in terms of the three measured quantities and the gain factor defined previously:

$$r = \frac{1}{G} \cdot \frac{\Delta D}{\Delta P_{+} + 2 \cdot \Delta P_{-}}. \tag{2.20}$$

To measure the quantities ΔD, ΔP_{+}, and ΔP_{-}, we utilize three lock-in amplifiers. Lock-in amplification works by multiplying a voltage signal with a reference frequency and low-pass filtering the result, removing any contributions from the signal that are not oscillating at the same frequency as the reference and outputing a DC voltage proportional to the amplitude of the component that is resonant. In this case, we reference the amplifiers to the chopping frequency of the pump, which isolates only the components of D, P_{+}, and P_{-} that are changing at the same frequency as the pump modulation, i.e., the differential component. This can be done with exquisite sensitivity, which greatly improves the SNR of the measured differential signal. Hence, with a single pair of balanced photodetectors and three lock-in amplifiers we measure the transient absorption anisotropy with high SNR.

Chapter 3

Static disorder has a dynamic effect on energy transfer in biomimetic light harvesting complexes

This chapter is adapted from previous original work reported in J. Phys. Chem. B,[49] *reproduced under the CC-BY-4.0 Creative Commons license.*

Natural light-harvesting protein complexes (LHC) in plants and photosynthetic bacteria absorb photons from the sun and, within a few tens of picoseconds, transport that energy across several protein complexes to reaction centers, where charge separation and subsequent chemistry occur.[32] Remarkably, this transfer process can have near unity quantum efficiency, thus a detailed model of which parameters lead to this efficiency is of great fundamental interest and is of value for developing efficient artificial light-harvesting technologies such as sensitive photodetectors and artificial photosynthesis.[34,72,73] Despite extensive study, a full picture of the structure-function relationships that give rise to excellent energy transfer capabilities of LHCs in plants and photosynthetic bacteria remains to be described. In natural LHCs, the difficulty lies mainly in the complexity of these multi-process systems, compounded by their fragility *in vitro*, which makes systematic investigation, for example through targeted mutation,[74–77] difficult.

Many artificial LHCs have been developed and studied, but these typically rely on short-range energy funnels.[78–82] Light harvesting in natural LHCs often involves energy transfer between identical chromophores. In particular, some purple bacteria species develop extended regions of identical protein subunits in low-light conditions, which is known to increase efficiency.[34,83] Measurement of energy transfer between spectrally-identical chromophores is difficult due to the lack of an obvious signature of energy transfer. In some cases, time-resolved polarization anisotropy measurements can be used to characterize energy transfer,[66,84–86] by measuring the loss of preferred orientation i.e., depolarization, of the probed transition dipole moment (TDM) following excitation. As explained in Chapter 3,

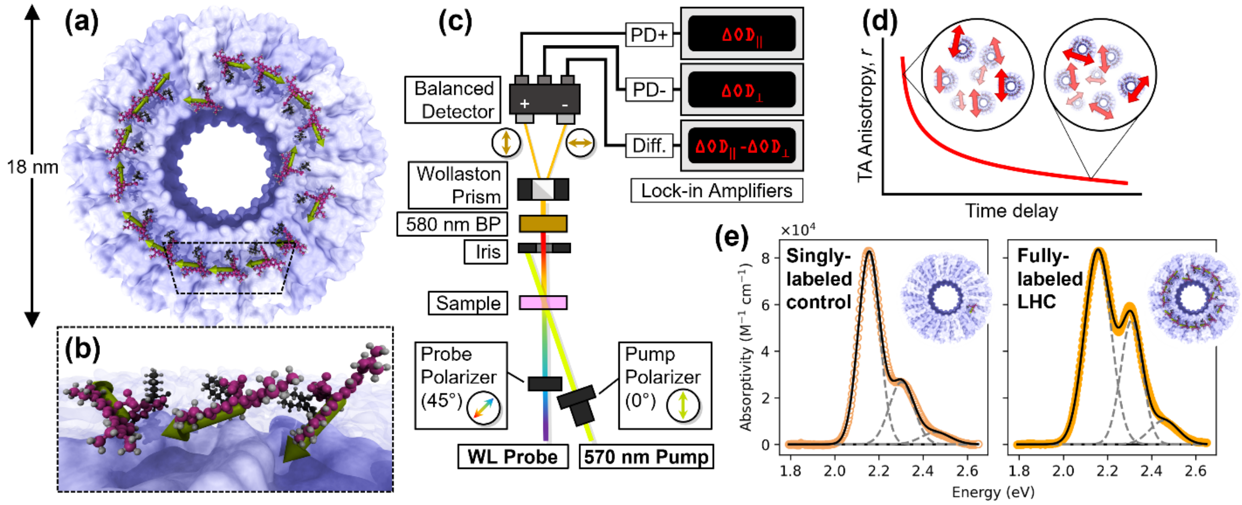

Figure 3.1: Overview of the TAA experiment on cpTMV-SRB biomimetic light harvesting complexes. (a) Schematic representation of the cpTMV biomimetic LHC with attached SRB chromophores, and (b) a zoomed-in view on three binding sites demonstrating the high TDM orientational disorder. (c) Diagram of the TAA experimental setup, indicating polarization of pump and probe beams and use of Wollaston prism to measure both polarization components simultaneously, yielding (d) a TAA decay curve following optical excitation as energy transfer randomizes TDM orientation. (e) Steady-state absorption spectra of the singly-labeled controls and the fully-labeled LHCs.

transient absorption anisotropy (TAA) is one technique able to probe depolarization without relying on fluorescence. These types of measurements are challenging due to the low sensitivity of absorption measurements and often overlapping spectral features with uniquely evolving anisotropies. The benefit of using TAA, however, is its general applicability to any absorbing sample, and the relative simplicity of ultrafast implementation compared to, for example, fluorescence upconversion. In addition, TAA as a quantitative measure of energy transfer relies on the ability to isolate the depolarization associated with energy transfer from those due to other processes, such as rotational diffusion. In natural systems, the inability to modularly synthesize control complexes, however, still makes this isolation difficult.

In this study we demonstrate rapid energy transfer in a modular biomimetic LHC consisting of protein-bound identical chromophores and uncover the microscopic sources of disorder whose future control will facilitate even longer-range exciton migration in this system. In Section 3.1, we introduce our model artificial LHC and detail its preparation. Then, in Section 3.2 we report our TAA and time-resolved fluorimetry measurements on these artificial LHCs that reveal signatures of energy transfer. Next, in Section 3.3.1 we describe our implementation of a kinetic Monte Carlo simulation based on Förster energy transfer between chromophores in these ring-shaped complexes and the three sources of disorder—orientation, site energy, and coupling—that recapitulation of the observed TAA and time-resolved fluorimetry measurements. Finally, in Section 3.4 we discuss the impacts of the various sources of disorder on the emergent excitation migration, and in Section 3.5 we provide some promising future directions for this project.

3.1 Preparation of singly-labeled control complexes and fully-labeled LHCs

Our model biomimetic LHC is based on a circular permutant of the tobacco mosaic virus (cpTMV) coat protein which self-assembles into C_2-symmetric double-disk super-complexes (PDB:3KML),[46] with each disk composed of 17 identical monomers, as seen in Fig. 3.1(a). By preparing mutants with reactive cysteine substitutions, we covalently attach chromophores at specific sites, as illustrated in Fig. 3.1(b), affording great control over factors such as chromophore identity and location,[47] and rigidity of the linking molecule.[48] Utilizing this modularity, we construct a model system amenable to study by TAA and, importantly, we can also generate singly-labeled control complexes to isolate the signature of energy transfer in this measurement from confounding effects of rotational diffusion. This work represents a crucial step in constructing an artificial LHC super-complex that can serve as a truly biomimetic model system to study long-range energy transfer. Our measurements demonstrate that site-to-site energy transfer occurs quickly in these LHCs, while long-ranged transport is currently somewhat impeded by disorder in TDM orientation, site energy, and coupling. Fortunately, the modularity afforded by this system affords a high degree of control appropriate for addressing these sources of disorder.

By varying the stoichiometry of the bioconjugation sample preparation procedure (described below), we produce both fully-labeled LHCs (Fig. 3.1(e), right), with a chromophore at every site, and singly-labeled control complexes (Fig. 3.1(e), left), which allows us to study inter-chromophore interactions separate from protein-chromophore interactions. The synthesis of the biomimetic cpTMV LHCs was developed in Matt Francis' lab and first reported in 2010..[87] The details of this synthesis, including synthetic procedures, mutant generation, protein expression, bioconjugation, and purity analyses, have been described in detail in previous collaborative work between the Ginsberg and Francis labs,[47,48] and synthesis for this work was performed by Jing Dai and Amanda Bischoff.[49] Briefly, maleimide functionalized sulforhodamine B (SRB) chromophores with SS-cyclohexyl linkers[†] are synthesized from commercially available alcoholamines. SS-cyclohexyl linkers are much more rigid than typical molecular linkers and were developed with the goal of immobilizing the SRB on the protein surface.[48] Site-directed mutagenesis is performed on a circular permutant of the tobacco mosaic virus coat protein to prepare D18C mutants, and the proteins are expressed in *E. coli.* cpTMV fully-labeled LHCs and singly-labeled control samples are pre-

---

[†] SS signifies the chirality of the two adjacent carbon atoms on the cyclohexyl group that bridges the SRB and maleimide groups.

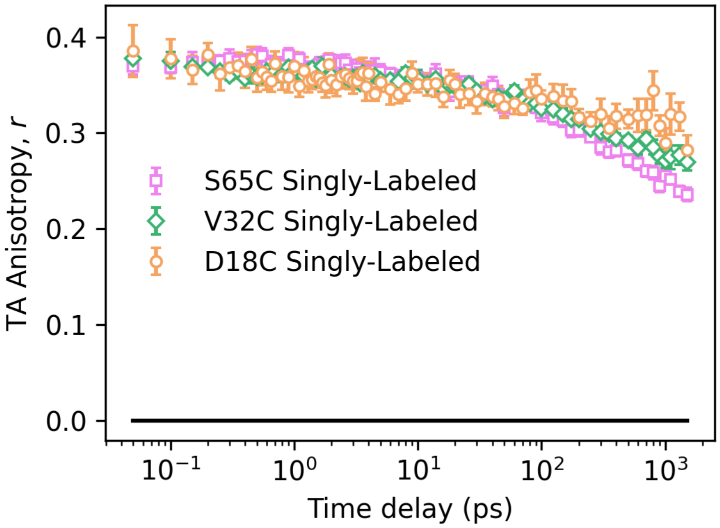

Figure 3.2: TAA data of singly-labeled cpTMV-SRB control samples at different sites on the protein surface, with anisotropy decay least prevalent on D18C complexes indicating highest site rigidity.

pared by maleimide bioconjugation of the modified SRB complexes with the reactive cysteine introduced to the mutant cpTMV surface. Fully-labeled LHCs are prepared by performing the bioconjugation with >1 equivalents of modified SRB and the mutant cpTMV monomers. For the singly-labeled controls that assist in dissecting contributions to the TAA signal, 0.01 equivalents are used, resulting in statistically singly-labeled complexes, though the majority have no attached chromophores. Labeling yields are verified by electrospray ionization time-of-flight mass spectrometry connected with high-performance liquid chromatography, and size-exclusion chromatography is performed to purify the samples. Prior to transient absorption anisotropy measurements, all samples are diluted to an optical density (OD) of 0.1 at the pump wavelength of 570 nm, resonant with the SRB $S_0 \rightarrow S_1$ transition.

The steady-state absorption spectra of singly-labeled control complexes and full-labeled LHCs are shown in Fig. 3.1(e) and both show a vibronic progression of peaks. The higher relative amplitude of the second vibronic peak in the fully-labeled complex most likely arises from the close proximity of the SRB molecules to one another.[88] We rely on a separation of the time scales of energy transfer and chromophore reorientation, using short, rigid linking molecules and a sufficiently immobile attachment site on the protein, in order to distinguish energy transfer from rotational diffusion of the chromophore. For the purpose of immobilization, we select D18C TMV mutants, in which the chromophore binding sites are 4.5 nm from the center of the disk and separated by 1.5 nm from one another. D18C mutants also demonstrate the greatest immobilization in control experiments, as seen in the comparison TAA decays of singly-labeled controls at different sites in Fig. 3.2. In the absence of energy transfer, TAA measurements on the SL control complexes report solely on the motion of the chromophore and how it is impacted by interaction with the protein. While this does not account for the effects that chromophore-chromophore interactions may have on reorientation in the fully-labeled LHCs, it is unlikely that the increased concentration of chromophores would lead to significantly faster reorientation dynamics.

3.2 Transient Absorption Anisotropy and Time-Resolved Fluorimetry of Artificial LHCs

We measure ultrafast optical TAA of our biomimetic LHCs to characterize the ultrafast depolarization associated with energy transfer following optical excitation by a linearly polarized 100 fs laser pulse. As detailed in the previous chapter, TAA is a variation of transient absorption (TA), a pump probe technique, in which a pump light pulse (Fig. 3.1(c), yellow) first excites the sample (Fig. 3.1(c), pink), and a probe light pulse (Fig. 3.1(c), rainbow-colored) is used to observe changes of the excited state population at progressively longer time delays in successive experiments.[31]

In the experimental setup in Fig. 3.1(c), we use a balanced photodiode detector to measure the parallel and perpendicular TA components, and their difference, simultaneously via lock-in amplification, allowing an excellent SNR, as described in Section 2.3. cpTMV LHC samples are diluted in buffer to an OD of 0.1 at 570 nm and measured in a 1 mm path length quartz cuvette (Starna Cells, 21-Q-1). The sample holder is on a continuously rastering micrometer stage to prevent burning, and ground-state UV/Vis spectra are taken before and after each measurement to check for sample damage. We resonantly pump the samples with a 570 nm pump laser (18 $\mu J/cm^2$ pulse fluence) chopped at 625 Hz (one eighth the 5 kHz repetition rate of the laser), and by filtering a white light continuum pulse, we take single-wavelength TAA measurements at 580 nm, on the red side of the ground state bleach (GSB) peak of sulforhodamine B (SRB), the labeling chromophore. The GSB, which results from the absence of ground-state absorption in the excited chromophores, is the strongest feature in the TA spectrum of the SRB molecule. In addition, because the pumped and probed transitions are the same in the GSB, this transition is expected to have the maximum initial anisotropy of 0.4.[31]

As shown in Fig. 3.3(a) on a logarithmic time scale, TAA measurements of the ground state bleach of the cpTMV LHCs (solid yellow circles) demonstrate a decay, while uncoupled singly-labeled control complexes (open yellow circles) exhibit almost none. The TA anisotropy decay of the cpTMV LHCs extends over several decades in time, from hundreds of femtoseconds to hundreds of picoseconds, with super-exponential decay at early times and then stretched, sub-exponential decay at late times. In the singly-labeled control complexes, where energy transfer is not possible, the TA anisotropy remains almost constant over the course of the measurement, falling only slightly from 0.37 immediately after excitation to 0.33 at 1.5 ns. In a free dye control sample (Fig. 3.3(a), grey circles), we observe an expo-

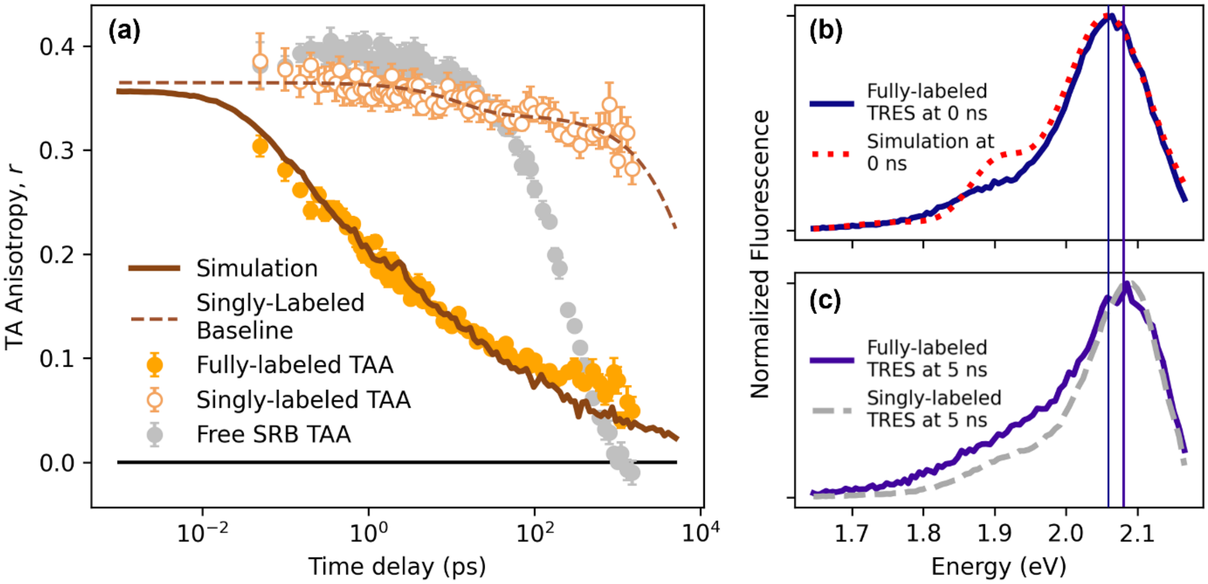

Figure 3.3: Spectroscopically resolving energy transfer in the cpTMV LHC. (a) Experimental TAA data (dots) at 580 nm of free SRB chromophore in solution (grey), singly-labeled control (orange outlined) and fully-labeled LHC (solid orange), with error bars representing standard error relative to the mean of 10 consecutive measurements. Note the log scale in time, causing exponential decays to appear as sigmoids. Overlaid are the biexponential fit to the singly-labeled decay (dashed line) and anisotropy computed from the simulation (solid line). (b) Early-time emission spectrum of fully-labeled LHC, overlaid with predicted spectrum from simulation (dotted red), and (c) late-time emission spectrum of fully-labeled LHC overlaid with late-time emission spectrum of singly-labeled controls (dashed gray), with drop lines to indicate spectral shift.

nential decay from 0.38 to 0 (a characteristic sigmoid shape when plotted on a logarithmic time axis) with a time constant of 260 ps, which matches well to literature values.[89,90] We generate the magic-angle TA decays $\Delta OD_{MA} = \Delta OD_{\parallel} + 2 \cdot \Delta OD_{\perp}$ for the denominator of the anisotropy expression. As shown in Fig. 3.4(b) and (c), the magic-angle TA decays for the free dye and singly-labeled complexes are well-fit by a biexponential decay, which we previously attributed to vibrational relaxation and radiative decay processes.[48] Meanwhile the LHCs show a more extended TA decay profile over several decades that decays faster than their singly-labeled counterparts. Table 3.1 lists the parameters for multiexponential fits of these data.

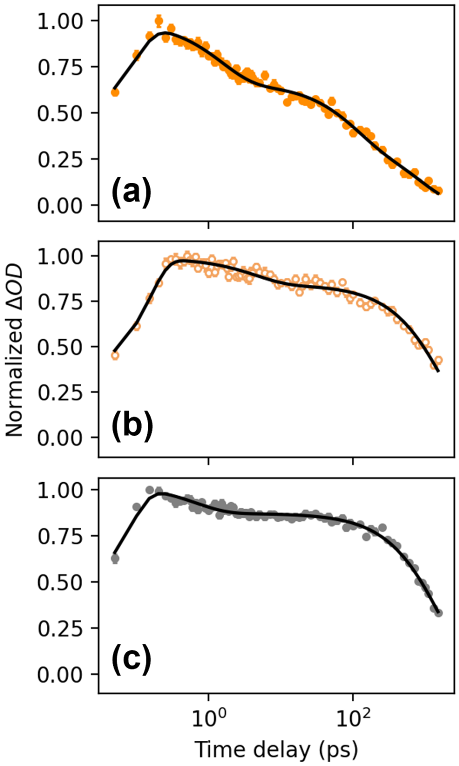

Figure 3.4: Magic-angle TA kinetics of (a) fully-labeled cpTMV LHC, (b) singly-labeled control, and (c) free SRB control at 580 nm, with multiexponential reconvolution fits overlaid; see fit parameters in Table 3.1.

	A_1	τ_1 (ps)	A_2	τ_2 (ps)	A_3	τ_3 (ps)
Fully-labeled LHC	0.33	1.5	0.31	98	0.35	870
Singly-labeled control	0.15	4.4	—	—	0.84	1800
Free SRB control	0.15	6.6	—	—	0.87	1600

Table 3.1: Multiexponential reconvolution fits for magic-angle TA kinetics as shown in Fig. 3.4. Fit equation is of the form $\Delta OD(t) = IRF(t) * \left(\sum_n A_n \cdot e^{-(t-t_0)/\tau_n}\right)$, where n indexes exponential components, t_0 is the pump-probe overlap time (not shown, typically $|t_0| < 50$ fs), and $IRF(t)$ is the instrument response function, assumed to be Gaussian.

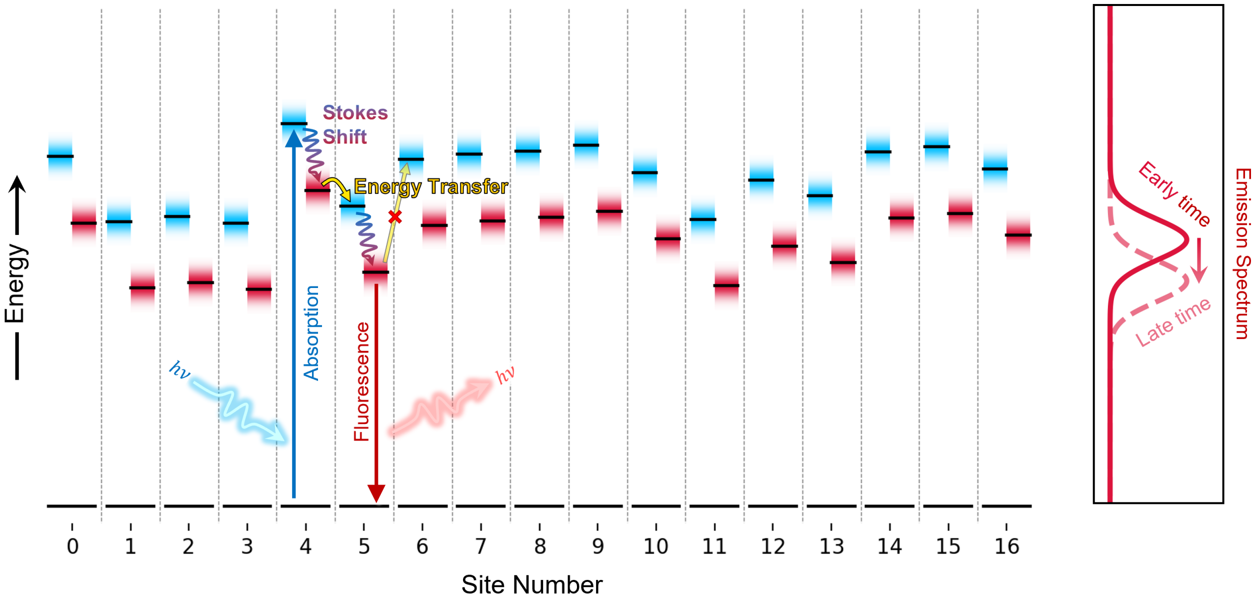

Figure 3.5: Schematic representation of manifestation of energy transfer in time-resolved emission spectra. Left panel depicts a hypothetical system's inhomogeneous site energies (absorption in blue, fluorescence in red), with energy transfer preferentially proceeding towards lower-energy sites. Right panel depicts shift in energy spectrum following excitation due to downhill energy transfer.

3.2.1 Time-resolved Emission Spectra

Time-resolve emission spectra (TRES) serves as a valuable complementary measurement to TAA to resolve energetic shifts in the excited state population. In TRES, the sample is excited by a laser pulse, and the fluorescence decay is measured over a range of detection wavelengths. Taken together, TRES allows for resolving how the emission spectrum of the sample changes over time, following excitation.

This technique is useful in studying energy transfer in a network of chromophores with energetic disorder, i.e., when the energy levels of individual sites have some random distribution. As depicted in Fig. 3.5, in a system with site energetic disorder, following excitation (blue arrow), energy transfer (yellow arrow) preferentially proceeds downhill due to the energy losses associated with the Stokes shift (red-blue gradient arrow) following each "hop." Thus excitations tend towards lower energy sites over time, which causes an overall red shift of the emission spectrum over time (right panel), with the degree of shift depending on the magnitude of energetic disorder.[25]

To characterize the evolution of the average site energy following excitation, we collected TRES measurements of the fully-labeled LHCs and singly-labeled controls. TRES data are collected on cpTMV samples in 100 mM sodium phosphate buffer solution, in a 2 mm-wide, 10 mm path length cuvette (Starna Cells 18F-Q-10-GL14-S). In a PicoQuant FluoTime

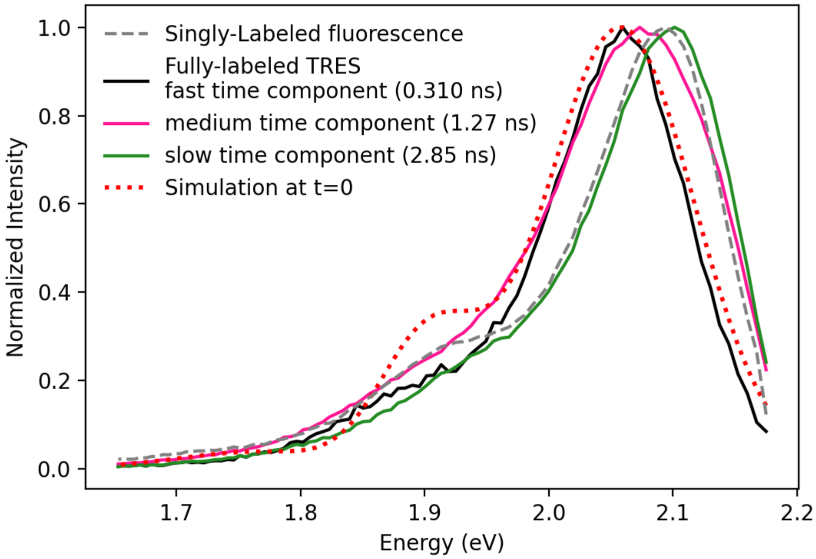

Figure 3.6: Components of triexponential fit to TRES of fully-labeled cpTMV LHC (solid curves) compared to the early time spectrum of simulated population convolved with a 150 ps Gaussian IRF (dotted red), and to the late-time spectrum of singly-labeled control complexes (dashed gray).

300 fluorometer, the samples are resonantly excited at 565 nm by a 150 ps laser pulse (PicoQuant LDH-D-TA-560B), and an emission decay is collected via time-correlated single photon counting (TCSPC) via a PicoQuant PMA 192 photomultiplier tube at wavelengths from 570 nm to 750 nm.

The TRES data demonstrate the emergence of a red-shifted component in the fully-labeled LHCs that is absent in the singly-labeled controls. The fully-labeled LHC TRES data is fit by three exponentially-decaying components, which are shown in Fig. 3.6: one short-lived 310 ps component that is redshifted by 0.04 eV relative to the singly-labeled control spectrum, one long-lived component resembling that of the SL controls (2.85 ns), and one intermediate component (1.27 ns) that appears to be a mixture of the two with an intermediate lifetime. Thus, the spectrum appears red-shifted relative to the singly-labeled controls at early times, as seen in Fig. 3.3(b), while at late times the spectrum, as shown in Fig. 3.3(c) appears very similar to that of the singly-labeled control, which does not demonstrate any appreciable shift in energy over time. We assign the red-shifted components to the excitations that undergo rapid energy transfer, and the SL-like component to excitations on uncoupled chromophores which are unable to participate in energy transfer.

3.3 Kinetic Monte Carlo simulations of FRET hopping in TMV complexes

To relate the observed TAA and TRES data to a microscopic picture of energy transfer within the TMV complexes, we use a kinetic Monte Carlo simulation based on incoherent hopping of excitations among static TDMs on a ring. Our approach incorporates methods developed by Bradforth *et al.*[66] and Bardeen.[67,92] A full description of the simulations is included in the following subsection, but briefly, we evenly space 17 sites around a ring of radius 4.5 nm, equal to the radius of the D18C binding site. At each site, we generate a unit vector representing the chromophore's TDM orientation by sampling from the orientational distribution obtained from molecular dynamics simulations of a single chromophore attached to the LHC surface.[48] A representation of one such ring is shown in Fig. 3.7(a) with the TDMs represented by rods originating at the chromophore binding sites. TDM orientation local coordinate system shown in the inset. The vectors are represented in a lab frame with the z-axis parallel to the implied polarization of the excitation. We assign each site an energy, indicated in false color in Fig. 3.7(a), drawn from a Gaussian distribution with width given by the inhomogeneous width. The rates between each pair of sites on the ring are then calculated using Förster theory, giving a 17×17 matrix of rates. We thus generate a population of thousands of these rings and randomly rotate them relative to one another to simulate the random orientation of the rings in solution. Using an implementation of the Gillespie algorithm,[93–95] we place one excitation on each ring and allow these excitations to hop between sites, producing a trajectory for each ring, two of which are represented in Fig. 3.7 (b), with the initial conditions of the chromophores shown at the bottom and the trajectories being traced as a function of time in the vertical direction. The polarization anisotropy $r(t)$ of the excited state population is then calculated from the orientation of the TDMs of the sites occupied by the excitations at any given time after "excitation."

3.3.1 Kinetic Monte Carlo Simulation Setup and Details

To simulate incoherent energy transfer in our statically disordered system, we represent an artificial light-harvesting complex as a ring of unit vectors each representing the orientation of the transition dipole moment (TDM) of a chromophore bound to the protein surface. These unit vectors are represented in a lab frame illustrated in Fig. 3.8(b), where the z-axis is parallel to the polarization of the electric field of the pump. The orientation of each TDM in its site-local frame of reference (i.e., relative to the center of the ring, as shown in Fig. 3.8(b)) is selected via rejection sampling[96] from a probability distribution $P(\theta, \phi)$ over polar angle θ and azimuthal angle ϕ. We perform simulations using two types of probability distributions of the TDM orientations: one obtained from molecular dynamics (MD) simulations and the other type being Gaussian probability distribution, described below. Once the TDM orientations are selected, each site is assigned an energy drawn from a Gaussian distribution centered at the fundamental absorption energy $\tilde{\nu}_0$ and width σ_{ih},

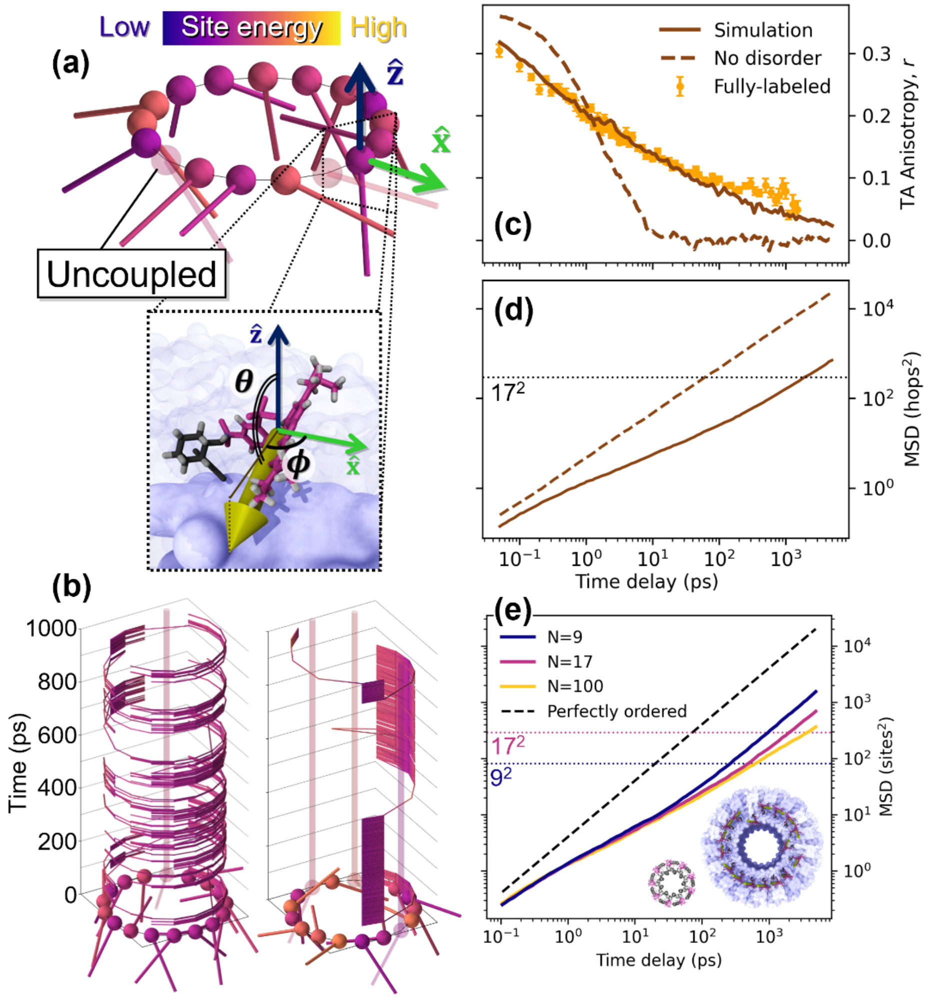

Figure 3.7: Overview of simulation setup and results. Here, (a) is a representative ring of TDM orientation vectors, with site energy color scale normalized to entire population and uncoupled chromophores shown with reduced opacity; zoom-in shows schematic representation of chromophore corresponding to a given TDM vector in the site-local coordinate frame. (b) Two such rings with excitation trajectories shown, with time increasing vertically upward. (c) The simulation fit with and without disorder included, overlaid with experimental TAA data, and (d) the corresponding mean squared expansion of excitation population, with dotted line indicating the boundary of the equilibrium regime. (e) Similar such MSD curves shown for simulations with varying numbers of sites, including $N = 9$ corresponding to LH2 (shown inset, PDB:1NKZ[91]), demonstrating size-dependent equilibrium diffusivity.

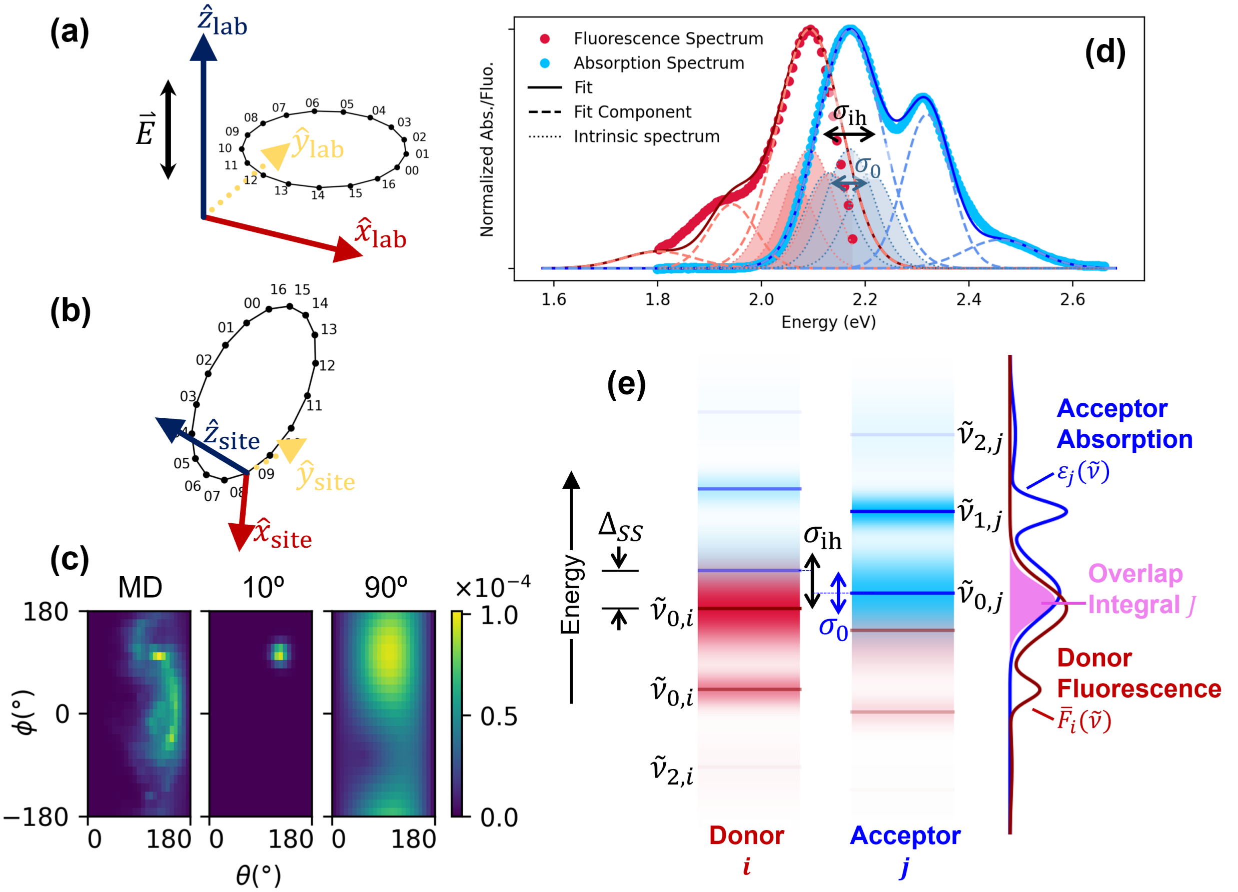

Figure 3.8: The orientational and energetic parameters passed to the kinetic Monte Carlo simulation. (a) The lab frame of the simulation, where the electric field $\vec{E}$ is parallel to the z-axis $\hat{z}_{\text{lab}}$. (b) The local site frame where the x-axis $\hat{x}_{\text{site}}$ points outward from the center of the ring. In this coordinate frame the orientations are randomly generated from an orientation probability distribution, as shown in false color in (c), obtained from molecular dynamics simulations (left panel) or using a Gaussian distribution (right two panels, for two widths σ_α). (d) The Gaussian fits to the absorption and emission spectra of the LHC, with the inhomogeneous linewidth σ_{ih} and intrinsic linewidth σ_0 represented; from this fit we derive the parameters shown in (e) which are used in the computation of the spectral overlap integral J (see Eqn. 3.13).

representing the inhomogeneous broadening.

The TDM orientation probability distribution used to match the experimental data, which can be seen in the leftmost panel of Fig. 3.8(c), is obtained from MD simulations, performed by Julia Rogers for a previous collaboration, of an individual chromophore covalently attached via a SS-cyclohexyl linker to residue 25 (as numbered in PDB 3KML) on three surface exposed α-helices of the biomimetic LHC.[48] The orientation of the TDM during the MD simulation is approximated by the orientation of the xanthene core[97] of the chromophore (specifically the vector from atom C12 to C11) in its site-local frame. To construct the site-local frame, illustrated for one site in Fig. 3.8(b), the C atom of residue 25 and the N atom of residue 29 were used to define $\hat{x}_{\text{site}}$, and $\hat{z}_{\text{site}}$ as the vector normal to the plane that additionally contains the C_α atom of residue 25 (with all residue numbers as in PDB 3KML[46]). The distribution of θ and ϕ was constructed from the last 500 ns of the MD simulation. While experiments were performed on LHCs with the chromophore attached to a different, nearby residue, we do not expect this to significantly impact our findings since the experimental anisotropy curves are also well fit by sampling orientations from a Gaussian distribution with sufficient variance. Nevertheless, the distribution from the MD simulation captures the general influence of the linker, solvent, and protein environment.

To investigate the effects of TDM orientation disorder on excitation migration and anisotropy decay, we also run simulations using a Gaussian TDM orientation distribution. This orientation is defined with a central vector $\hat{\mu}_0$, chosen to be at the peak of the MD orientation distribution ($\theta_0 = 120°$, $\phi_0 = 105°$) and an angular width σ_α, which can be increased or decreased to respectively increase or decrease TDM orientational disorder. The probability $P_G(\theta,\phi)d\Omega$ for the TDM $\hat{\mu}$ defined by θ and ϕ to be drawn from this distribution, is defined as

$$P_G(\theta,\phi)d\Omega \propto e^{-\frac{\alpha^2}{2\sigma_\alpha^2}} \sin(\theta)d\theta d\phi, \tag{3.1}$$

where α is the angle formed between $\hat{\mu}$ and $\hat{\mu}_0$, i.e., $\alpha = \arccos(\hat{\mu}\cdot\hat{\mu}_0)$, and the proportionality is set by normalization over the solid angle Ω. Two such orientation distributions for $\sigma_\alpha = 10°$ and $\sigma_\alpha = 90°$ are represented in false color in the right two panels of Fig. 3.8(c). In the limit where $\sigma \to 0$ we obtain a Dirac delta function distribution where all TDMs on a ring point in the same direction in their site-local frame, while in the limit $\sigma \to \infty$ we obtain a uniform random TDM orientation distribution.

Once the rings are generated, they must be rotated randomly to simulate the random orientation of TMV rings in solution during the measurement. To do so, each ring is associated with a randomly-generated 3D rotation matrix. Because there is a correlation between the different sites' orientations, care must be taken to do this correctly, as the selection of orientations must produce the same distribution one would expect from photoexcitation. In the dipole approximation, the probability of excitation at any site is proportional to the modulus squares of the dot product of the TDM with the electric field, $|\hat{\mu}\cdot\vec{E}|^2$, or equivalently in this context, μ_z^2 in the lab frame. For a dilutely excited population, where rings predominantly have one or zero excitations, the probability of a ring having one excitation is proportional to the average of all its member TDMs' alignments with the electric field:

$$P_{\text{ring}} \propto \frac{1}{N} \sum_{i=0}^{N-1} |\hat{\mu}_i \cdot \vec{E}|^2, \tag{3.2}$$

where N is the number of sites on a ring and $\hat{\mu}_i$ is the TDM at the i^{th} site. This is achieved by rejection sampling against the above probability criterion.

3.3.1.1 Calculating site-to-site rates via Förster theory

The rate $k_{i,j}$ between each site i and j on each ring is calculated using Förster theory. Förster resonance energy transfer (FRET) is an incoherent energy transfer process by which an excited donor molecule transfers its energy to a nearby acceptor molecule via a dipole-dipole interaction of their respective TDMs.[16] This process typically occurs on the order of 1-10 nm; further than 10 nm, energy transfer becomes exceedingly rare, and closer than 1 nm, other transfer pathways relying on direct wavefunction overlap dominate.[1,98] With an inter-site distance of 1.5 nm in the cpTMV LHCs, the inter-chromophore energy transfer is thus squarely in the FRET regime. Taking the position of the D18C binding site as the position of the molecule, according to FRET theory, the rate of transfer $k_{i,j}$ is given by:

$$k_{i,j} = k_F \cdot \frac{R_0^6}{r_{i,j}^6}, \tag{3.3}$$

where k_F is the fluorescence rate of SRB in the absence of FRET (1/1600 ps^{-1}), $r_{i,j}$ is the distance between the sites in nm, and R_0 is the FRET radius in nm, given by:

$$R_0^6 = \left(10^7 \frac{\text{nm}}{\text{cm}}\right)^6 \cdot \frac{9 \log 10 \cdot \Phi \cdot \kappa^2 \cdot J}{128\pi^5 \cdot N_A \cdot \eta^4}, \tag{3.4}$$

where $\Phi = 0.9$ is the fluorescence quantum yield of SRB, N_A is Avogadro's number, $\eta = 1.33$ is the refractive index of the solvent, taken to be that of water. Here, κ^2 is the dipole orientation factor, which is computed from the two TDMs $\hat{\mu}_i$ and $\hat{\mu}_j$ and the unit vector $\hat{R}_{i,j}$ pointing from site i to site j:

$$\kappa^2 = \left(\hat{\mu}_i \cdot \hat{\mu}_j - 3 \cdot (\hat{\mu}_i \cdot \hat{R}_{i,j}) \cdot (\hat{\mu}_j \cdot \hat{R}_{i,j})\right)^2. \tag{3.5}$$

Last, J is the overlap integral of the acceptor's molar absorptivity spectrum $\varepsilon_j(\tilde{\nu})$ and the donor's area-normalized fluorescence spectrum $\bar{F}(\tilde{\nu})$:

$$J = \int_0^\infty \bar{F}_i(\tilde{\nu}) \cdot \varepsilon_j(\tilde{\nu}) \cdot \tilde{\nu}^{-4} d\tilde{\nu}, \tag{3.6}$$

which, when evaluated over energy in wavenumbers (cm^{-1}) has units of $\text{cm}^6 \cdot \text{mol}^{-1}$. In short, efficient FRET transfer requires the donor and acceptor molecules to:

- be within a distance of $\leq R_0$ of one another, with efficiency scaling inversely by R^6,
- bave their TDMs aligned either parallel or head-to-tail, and
- have good overlap between the fluorescence spectrum of the donor and the absorption spectrum of the acceptor.

Our calculation of J builds on the method developed by Ahn *et al.*[92] to incorporate the vibronic progression and differing intrinsic linewidths. For the simulation, the steady-state absorption and fluorescence spectra are fit by a sum of three Gaussian peaks, as shown in Fig. 3.8(d), representing the fundamental ($\tilde{\nu}_0$) and two higher vibronic transitions. The fit for absorption is specified by the lowest absorption energy $\tilde{\nu}_0$, and for each peak (including the fundamental), an energy shift $\delta\tilde{\nu}_n$ relative to $\tilde{\nu}_0$, a width $\sigma_{\text{abs},n}$, and an absorption maximum $\varepsilon_{\text{abs},n}$ for each peak, where n indexes the peaks of the vibronic progression beginning at 0. The normalized fluorescence spectrum is fit by specifying a Stokes shift Δ_{SS} and a set of amplitudes $A_{\text{flu},m}$ for three peaks, otherwise using the same widths and energy shifts of the absorption peaks, in reversed energy order, thus assuming a perfectly mirror-imaged vibronic progression, which fits the spectrum reasonably well. A single inhomogeneous linewidth σ_{ih} is specified for all peaks, and the intrinsic linewidths σ_n for each peak are computed under a relation derived from the convolution of two Gaussians:

$$\sigma_n^2 = \sigma_{\text{abs},n}^2 - \sigma_{\text{ih}}^2, \tag{3.7}$$

and likewise for intrinsic peak amplitudes:

$$\varepsilon_n = \varepsilon_{\text{abs},n} \cdot \frac{\sqrt{\sigma_n^2 + \sigma_{\text{ih}}^2}}{\sigma_n}, \tag{3.8}$$

and for intrinsic fluorescence amplitudes F_n. For the mth donor fluorescence peak and the nth acceptor absorption peak we define the respective peak energies $\tilde{\nu}_{m,i}$ and $\tilde{\nu}_{n,j}$ as follows:

$$\tilde{\nu}_{m,i} = \tilde{\nu}_{0,i} - \Delta_{SS} - \delta\tilde{\nu}_m, \text{ and} \tag{3.9}$$

$$\tilde{\nu}_{n,j} = \tilde{\nu}_{0,j} + \delta\tilde{\nu}_n. \tag{3.10}$$

Thus, for each site an intrinsic absorption and fluorescence spectrum is constructed, using these intrinsic parameters as illustrated in Fig. 3.8(e) for a donor and acceptor pair of chromophores.

Next, the total overlap integral, shown as the pink shaded region in Fig. 3.8(e), between sites i and j is given by a sum of overlap integrals over each pair of peaks:

$$\sum_{n=0}^{2}\sum_{m=0}^{2}\int_0^\infty F_{i,m} \cdot \exp\left(-\frac{(\tilde{\nu}-\tilde{\nu}_{m,i})^2}{2\sigma_m^2}\right) \cdot \varepsilon_{j,n} \cdot \exp\left(-\frac{(\tilde{\nu}-\tilde{\nu}_{n,j})^2}{2\sigma_n^2}\right) \cdot \tilde{\nu}^{-4} d\tilde{\nu}. \tag{3.11}$$

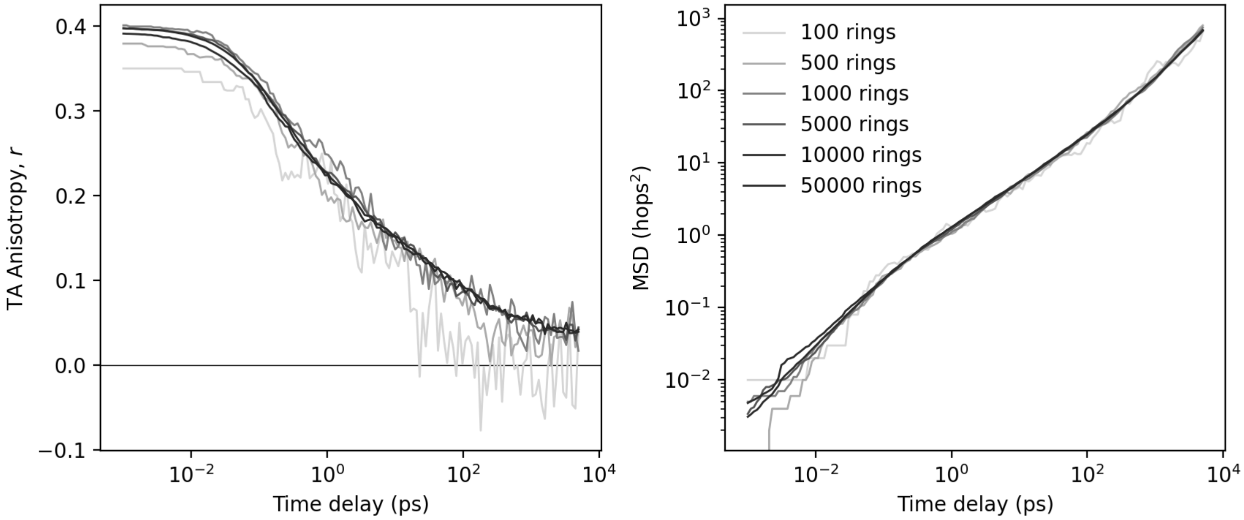

Figure 3.9: Convergence of the computed observables, anisotropy (top) and MSD (bottom), to a reproducible result occurs above a population size of 5000 for a 17-membered ring with disorder included.

The product of two Gaussians itself is Gaussian and thus the integrand of Eqn. 3.11 can be rewritten as a the product of a single Gaussian and $\tilde{\nu}^{-4}$:

$$\begin{gathered}\sum_{n=0}^{2}\sum_{m=0}^{2} F_{i,m}\cdot\varepsilon_{j,n}\cdot\exp\left(-\frac{(\tilde{\nu}_{n,j}-\tilde{\nu}_{m,i})^2}{2(\sigma_m^2+\sigma_n^2)}\right)\\ \cdot\int_0^\infty \exp\left(\frac{1}{2}\cdot\frac{\sigma_m^2+\sigma_n^2}{\sigma_m^2\cdot\sigma_n^2}\cdot\left(\tilde{\nu}-\frac{\sigma_n^2\tilde{\nu}_{m,i}+\sigma_m^2\tilde{\nu}_{n,j}}{\sigma_m^2+\sigma_n^2}\right)^2\right)\cdot\tilde{\nu}^{-4}d\tilde{\nu}.\end{gathered} \tag{3.12}$$

Eqn. 3.12 does not have an analytical solution; thus we make an approximation that the $\tilde{\nu}^{-4}$ term is constant over the width of the Gaussian, which is valid when the width is much smaller than the energy at the peak. We therefore treat the $\tilde{\nu}^{-4}$ term as constant when evaluated at the mean of the Gaussian, allowing analytical integration of the expression:

$$\begin{gathered}\sum_{n=0}^{2}\sum_{m=0}^{2} F_{i,m}\cdot\varepsilon_{j,n}\cdot\exp\left(-\frac{(\tilde{\nu}_{n,j}-\tilde{\nu}_{m,i})^2}{2(\sigma_m^2+\sigma_n^2)}\right)\cdot\left(\frac{\sigma_m^2+\sigma_n^2}{\sigma_n^2\tilde{\nu}_{m,i}+\sigma_m^2\tilde{\nu}_{n,j}}\right)^4\\ \cdot\sigma_m\cdot\sigma_n\sqrt{\frac{2\pi}{\sigma_m^2+\sigma_n^2}}.\end{gathered} \tag{3.13}$$

With this expression we efficiently compute J for all pairs of sites on each ring.

3.3.1.2 Running the Kinetic Monte Carlo simulation

An excitation is placed on each ring by randomly selecting a site with probability proportional its TDM's alignment with the $\hat{z}$-aligned electric field, i.e., $|\hat{\mu} \cdot \hat{z}|^2$. We then propagate the system in a kinetic Monte Carlo scheme using an implementation of the Gillespie algorithm.[93–95] For each ring we keep 1D arrays of each time at which the excitation hopped, the index of the site hopped to, and a tally of the excitation displacement in units of number of sites, with counterclockwise hops counted positively and *vice versa*. Each trajectory ends after 5 ns have elapsed, as the 1.6 ns lifetime of SRB is long enough that almost all chromophores will have relaxed back to the ground state.

Once all trajectories have ended, we compute the anisotropy of the population at any time t as:

$$r(t) = \frac{3\left\langle \mu_{n,z}^{*2} \right\rangle - 1}{2}, \tag{3.14}$$

where $\mu_{n,z}^{*}$ is the z-component of the TDM occupied by the excitation on the nth ring at time t, and $\langle \cdots \rangle$ denotes averaging over the population. As shown in Fig. 3.9, this observable converges to a repeatable value with around 5000 rings. The mean squared displacement (MSD) is similarly defined using the displacement:

$$MSD(t) = \left\langle d_n(t)^2 \right\rangle, \tag{3.15}$$

where $d_n(t)$ is the displacement of the excitation on the nth ring at time t. Last, we compute the time-dependent fluorescence spectrum of the excited population as:

$$F(\tilde{\nu}, t) = \langle IRF(t) * F_n(\tilde{\nu}, t) \rangle, \tag{3.16}$$

where $IRF(t)$ is the Gaussian instrument response function, and F_n is the fluorescence spectrum of the excited chromophore at time t.

3.3.2 Accounting for chromophore motion using singly-labeled TAA data

To account for contributions to the anisotropy decay in the model that are not due to inter-chromophore energy transfer, we incorporate the effects observed in the singly-labeled control complexes. Doing so involved fitting the experimental singly-labeled control TAA data, as described in the following process. We fit the slight TAA decay of the singly-labeled control complexes with a biexponential decay following the model of segmental motion of a protein-bound chromophore.[99] The expression used is $r_{SL}(t) = r_0 \cdot (\alpha e^{-t/\tau_F} + (1-\alpha)) \cdot e^{-t/\tau_P}$ where τ_F and τ_P are the time scales of the fast chromophore motion and slow protein motion, respectively, r_0 is the initial anisotropy, and $0 \leq \alpha \leq 1$ parameterized the chromophore's freedom of motion relative to the protein, with 0 being fully immobilized and 1 being fully unconstrained. Through least-squares fitting we arrive at parameters of r_0=0.36, τ_F=130 ps, τ_P=14 ns, and α=0.09, producing the dashed red "baseline" fit shown in Fig. 3.3(a). The initial anisotropy value r_0 of the singly-labeled complexes is lower than the theoretical maximum of 0.4; this is true not only in the SL control complexes but also in the free chromophore controls. This lower anisotropy is likely because of a small (<10%) contribution from the stimulated emission signal at this wavelength, which is not guaranteed to have maximum intrinsic anisotropy as the GSB is. In addition, scattering of the pump or the probe beam can spuriously increase or decrease the measured anisotropy. While we took steps to mitigate this contamination, we note that the initial anisotropy can vary between ~0.36-0.39 between different measurements, but without an appreciable impact on the rest of the analysis.

We take the anisotropy decay of the SL controls to represent the contribution to the decay in the fully-labeled LHCs coming from chromophore and protein fluctuations, occurring independent of any energy transfer. When two processes act independently to rotate the observed TDM, the effects of the two processes on the anisotropy decay combine multiplicatively. Thus, the anisotropy decay from the simulation $r_{\mathrm{sim}}(t)$ and the decay from the SL control data $r_{\mathrm{SL}}(t)$ are combined to yield a fit to the fully-labeled TAA decay $r_{\mathrm{FL}}(t) = \frac{r_{\mathrm{sim}}(t)}{0.4} \cdot r_{\mathrm{SL}}(t)$. The factor of 0.4 is necessary to avoid doubly applying the effect of photoselection that is present in both $r_{\mathrm{sim}}(t)$ and $r_{\mathrm{SL}}(t)$. This final expression combining the raw simulation results and the singly-labeled control fit is what is shown in Fig. 3.3(a) as the solid red curve, demonstrating excellent agreement with the experimental data.

3.3.3 Effects of disorder on excitation migration

The key simulation parameters required to recapitulate the experimental anisotropy decay are those that affect the sites differently on each ring, i.e., those that introduce disorder, which are: the static TDM orientation distribution, the site energy, and the uncoupled chromophores. Together, these three sources of disorder cause the anisotropy decay to be stretched from the exponential decay expected in the absence of disorder, as seen in Fig. 3.7(c). Each type of disorder has a distinct effect on the anisotropy and spectral properties of the population, but we observe a common signature when we track the mean squared displacement (MSD) of the excitation in hops^2 over time. The introduction of each type of disorder generates two different regimes in the MSD vs time. Diffusive transport is always arrived at at later times, however the apparent subdiffusive behavior in the exciton migration that precedes it corresponds to a non-equilibrium regime in which the initial condition relaxes to a more stable state through migration-based exploration of the chromophore disorder. This effect manifests as a distinct "s-curve" shape in the solid red plot of MSD vs time in Fig. 3.7(d). In the non-equilibrium regime, the MSD slows over time, seen as the slope of the curve temporarily decreasing over the first few hundred ps. In the diffusive transport regime, the curve adopts a linear form with unity slope, also benchmarked with the dashed line in Fig. 3.7(d), as the diffusivity D on this periodic one-dimensional lattice is governed by the relationship $MSD(t) = 2Dt$. Although each type of disorder qualitatively manifests similarly in the average observed MSD vs time, we next review their individual contributions

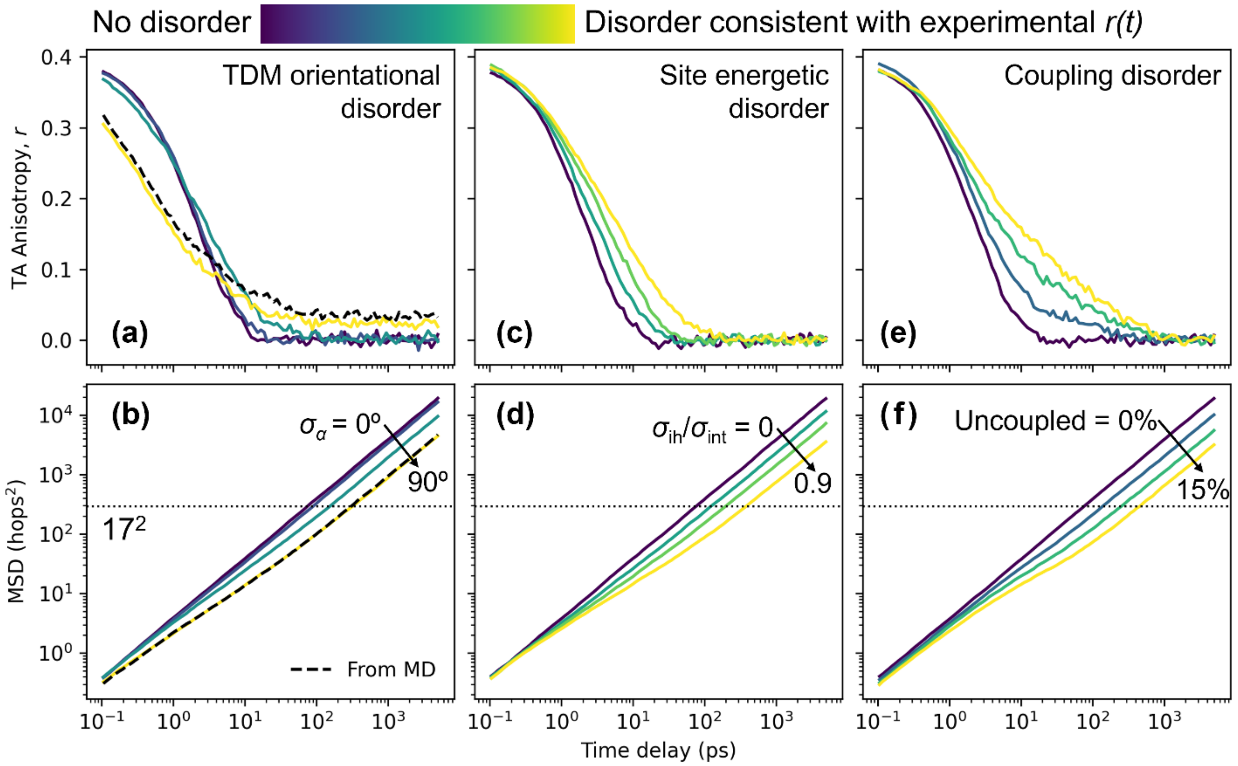

Figure 3.10: Simulated energy transfer observables in the cpTMV LHC. Simulated TAA (a,c,e) and MSD (b,d,f) on populations including disorder in only one parameter: (a-b) TDM orientation, using a Gaussian orientation distribution with width σ_α, (c-d) site energy, and (e-f) coupling. Normalized color scale is from complete absence of disorder increasing to equivalent value as included in reported simulation fit. TDM orientational plots (a-b) also include the results using molecular dynamics distribution (black dashed curves).

to the anisotropy and transport dynamics and explore their impact as a function of the extent of each type of disorder.

TDM orientational disorder causes the anisotropy to decay more slowly at late time delays as more relative TDM orientations are sampled. To explore this concept further, we additionally run simulations in which each TDM orientation is sampled from a Gaussian probability distribution centered on the orientation $\widehat{\mu}_0$ with width σ_α, as shown in Fig. 3.10(a-b). Except in cases of particularly poor dipole-dipole coupling, such as when adjacent TDMs are orthogonal, increased TDM orientational disorder reduces exciton mobility over time. In Fig. 3.10(b) we see that from the case with no disorder ($\sigma_\alpha = 0°$) to the highly disordered limit ($\sigma_\alpha = 90°$), the equilibrium excitation diffusivity, decreases from 1.9 hops^2/ps (blue curve) to 0.44 hops^2/ps (yellow curve). On the log-log scale of Fig. 3.10(b), the difference in diffusivity manifests as an offset between two linear curves with unity slope in the diffusive regime, i.e., at time delays when the curves have exceeded the indicated

$MSD = (17\ hops)^2$ dotted line. A unique effect of TDM orientational disorder, however, is an increased anisotropy decay at early times, as seen in the $\sigma_\alpha = 90^{\text{o}}$ case (yellow curve) in Fig. 3.10(a), where the anisotropy is lesser than in the perfectly ordered case (dark blue) until approximately 4 ps. This effect is not related to a change in the exciton mobility but is due to the greater depolarization associated with each hop between sites. To most faithfully reconstruct the experimental data, we use a TDM orientation probability distribution constructed from molecular dynamics simulations of an SRB-like dye interacting with key protein α-helices of the LHC construct,[48] which is plotted in the left-hand panel of Fig. 3.8(c). This simulation-derived distribution generates the anisotropy and MSD vs. time delay shown in the black dashed curves in Fig. 3.10(a) and (b), respectively. We find, however, that any sufficiently broad distribution produces similar kinetics, as the results using the $\sigma_\alpha = 90^\circ$ Gaussian distribution (yellow curve) match almost identically the results using the molecular dynamics simulations. A slight offset in the anisotropy of these curves in Fig. 3.10(a) evidences a very slight difference in the intrinsic anisotropy of these populations. Thus, the orientation distribution used is not a unique solution to fit the experimental data, but rather a limit in which the orientations are distributed broadly, and our model is thereby constrained to this limit by the prediction of molecular simulation.

Site energetic disorder similarly slows the exciton mobility over time, as excitons accumulate in the lowest-energy sites, often separated spatially from one another, similar to effects reported previously in other site-energetically disordered systems.[25,26] From the simulation, we also predict a spectral red shift as the excitations "cool" while exploring the energetic landscape. In the simulation, we parameterized the site energy disorder the ratio of the (inhomogeneous) width of the ensemble's energy distribution to the intrinsic width of each individual site, $\sigma_{\text{ih}}/\sigma_{\text{int}}$, where the values are constrained by the width of the measured absorption peak. Parameterization of the site energies has been used previously in the group for study of exciton migration in conjugated polymer films,[100] and has been reported elsewhere in similar kinetic Monte Carlo models that inspired this work.[92] A modest amount of site energy disorder, $\sigma_{\text{ih}}/\sigma_{\text{int}}$=0.9, produces a redshift of 0.04 eV that agrees with that seen in the TRES data, as shown by the overlap of the simulated spectrum (dotted red curve) and the early-time fluorescence of the biomimetic LHC (solid blue curve) in Fig. 3.3(b). In Fig. 3.10(d), the equilibrium exciton diffusivity decreases from 1.9 hops^2/ps with no site energetic disorder (blue curve) to 0.35 hops^2/ps (yellow curve / faint dotted line) when $\sigma_{\text{ih}}/\sigma_{\text{int}}$ is increased to 0.9–the ratio ultimately deduced to best match the experimental data. This effect is primarily evidenced in the later decades of the anisotropy decay in Fig. 3.10(c), causing a progressively longer tail to appear as site energy disorder is increased relative to the exponential decay expected in the absence of disorder. If the only contributions to disorder were orientational and this modest contribution from site energies, however, the model could not mimic the long tail of the experimental anisotropy decay. In fact, to fit this data by increasing the site energy disorder alone would require $\sigma_{\text{ih}}/\sigma_{\text{int}}$=4. In order to simultaneously model the TAA decay and the TRES data, another source of disorder is required—hence the addition of randomly uncoupled chromophores.

The introduction of uncoupled chromophores slows the overall exciton mobility considerably, and greatly stretches the late-time anisotropy decay. Uncoupled chromophores, i.e., sites to and from which the rate of energy transfer is greatly diminished, are introduced to the simulation phenomenologically to account for the singly-labeled-like fluorescence and long-time anisotropy observed in the experimental data. With the above mentioned orientational disorder constrained to the highly random limit and site energy disorder constrained by the magnitude of the redshift observed in TRES, we find that uncoupling 15% of the chromophores results in an excellent fit to the TAA data. As seen in Fig. 3.10(f), when increasing this coupling disorder from 0% to the 15% used in the best fit to the experimental data, the equilibrium excitation diffusivity decreases from 1.9 hops^2/ps to 0.31 hops^2/ps. The exciton mobility is reduced due to the barrier-like nature of these uncoupled chromophores, which effectively introduce gaps in the ring of sites. In addition, the subpopulation of excitations that are initialized on one of these isolated chromophores remains locked in said state, meaning this subpopulation remains highly polarized for much longer, which greatly slows the late time anisotropy decay. This phenomenon is best demonstrated by comparing the coupling and site energy disorder. Despite a similar impact on exciton mobility, i.e., the vertical offset in the diffusion regime for the highest amounts of disorder (yellow curves) in Fig. 3.10(d) and (f), the effect of coupling disorder seen in Fig. 3.10(e) on the anisotropy is highly substantial, with an elevated tail stretching into the 100s of picoseconds, compared to the modest impact of site energetic disorder on anisotropy in Fig. 3.10(c).

3.4 Impacts of disorder on excitation migration in artificial cpTMV LHCs

Overall, we find from our model that static disorder has the effect of "stretching" out the relaxation of the biomimetic LHC system (and the associated anisotropy decay) across several decades in time from an exponential form, in the case of no disorder, to that which is observed in the TAA data. Our simulations allow us to study this effect in detail, *in silico*. They show that exciton migration in the presence of all types of disorder equilibrates to ordinary diffusion after a period of a few hundred picoseconds, albeit with a lower diffusion constant than the perfectly ordered case. As demonstrated in Fig. 3.7(d), the time at which regular diffusion is adopted corresponds to the time at which, on average, all excitations have explored their entire ring, i.e., $MSD = (17\ hops)^2$ (dotted horizontal line). Thus, this behavior is associated with an equilibration as excitons explore the entirety of the system and its associated disorder, a phenomenon also observed in a linear system by Ahn et. al.[92] This slowing of exciton mobility following excitation manifests in the anisotropy as an elongation of the model's decay (solid curve) in later decades, Fig. 3.7(c), as average exciton migration in the equilibrium state is strictly slower than the initial condition. Effectively, long-range migration is dominated by the slowest transfer steps, whether resulting from a pair of poorly-aligned TDMs, a site that is low in energy relative to its neighbors, or an uncoupled chromophore. This effect is well-illustrated in the rightmost simulation trajectory in Fig.

3.7(b), where despite fast inter-site hopping, the trajectory shows the excitation remaining in limited subsections of the ring for long periods of time, only rarely hopping between these subsections, such as near 100, 500, and 900 ps. Closer inspection reveals the barriers between wells in this case to be both high-energy sites (colored yellow) and uncoupled chromophores (translucent spires). In contrast, the leftmost example in Fig. 3.7(b) shows a trajectory on a ring in which site energy disorder is low (all site energies are close to the mean energy, indicated by a common plum color of the trajectory trace) and there is only one uncoupled chromophore. Indeed, on this ring the excitation travels more freely, with only two noticeable exceptions: one clearly due to the uncoupled chromophore, and also a second, more subtle orientational barrier due to the TDM seven sites counterclockwise to the first, which is nearly orthogonal to both its neighbors, corresponding to κ^2 values near 0. Simulations of rings of chromophores with fewer sites, with all else being equal, illustrate that this effect is dependent on the number of sites in a ring. A system with fewer sites recovers diffusive behavior earlier and at a higher final equilibrium diffusivity, as seen by comparing the late-time diffusivities between a 9-membered ring (blue) and a 17-membered ring (magenta) in the MSD vs time plots in Fig. 3.7(e). Based on this observation, we hypothesize that incoherent intra-complex energy transfer in circular light-harvesting complexes with fewer sites is more robust to disorder in general, compared to larger complexes. This principle could help to explain the design of the bacterial antenna complexes, as LH2 displays only nine-fold rotational symmetry,[91] and in low-light or low-temperature conditions some purple bacteria instead produce LH4, an eightfold-symmetric structure. Excitonic coupling and coherent transport do occur in these complexes, but nevertheless this principle could apply to any steps involving incoherent transport. Including inter-complex energy transfer would diminish this effect, as it opens the collection of accessible sites beyond the closed, periodic system of our model. Nevertheless, when complex-to-complex transfer is rate-limiting, efficient diffusion around a closed ring would be important for encountering exit sites.

The most straightforward demonstration of the slowing mobility occurs due to static site energy disorder, as the site energy is not directly correlated with the TDM orientation distribution as compared to the other two sources of disorder. A disordered energy environment intuitively results in the emergence of energy "wells," i.e., low-energy sites, out of which energy transfer is slower because it is more likely to be uphill. The population begins with the same average spectral overlap as a system with no site energetic disorder and thus similar exciton mobility. As the excitons explore their chromophore rings, however, they tend to become trapped in these low-energy sites, adopting an equilibrium Boltzmann distribution, and decreasing the spectral overlap and, correspondingly, the mobility, until equilibrium is reached. Thus increasing site energetic disorder does not affect the early-time anisotropy decay, but does stretch the late-time decay. Site energetic disorder additionally can be revealed spectrally from the red-shifted component in the TRES measurements. Since the magnitude of the TRES redshift is determined by the extent of energy disorder, we constrain the latter to a value of 0.04 eV, corresponding to $\sigma_{\mathrm{ih}}/\sigma_{\mathrm{int}} = 0.9$, to recapitulate the experimental redshift. A limitation of our model, however, is the assumption that site energy is independent of chromophore orientation. Since interaction with the protein surface can certainly impact electronic configuration, this is an approximation. In the case of strong interaction between chromophore and protein,[101] this assumption would likely not hold and would require more detailed rate calculations, which would greatly increase the complexity. Yet, this zeroth-order approximation appears valid in our case, as evidenced by the very modest differences between the steady-state spectra of free chromophore and singly-labeled control complexes.

3.4.1 Untangling energy transport effects from anisotropy decays requires care

We demonstrate that more care must be taken when associating TAA data with energy transfer when there is high static TDM orientational disorder in the experimental system, as the TDM orientation is itself associated with the anisotropy signal. We find a high degree of static orientational disorder exists in the surface-bound chromophores, as predicted by molecular dynamics simulations. Despite the rigidity of the linker holding the chromophores steady on nanosecond timescales, which we have shown previously to be important for extending the chromophore's initially hot vibrational excited state,[48] there is a high degree of orientational disorder that is static on the time scale of the electronic dynamics. This disorder is necessary in the simulations to recapitulate the early-time anisotropy decay, which, as seen in the highly disordered case (yellow curve) of Fig. 3.10(a), occurs super-exponentially, i.e., faster than the exponential decay of the perfectly ordered case (blue curve), due to the high degree of depolarization associated with a single hop In particular, in this case of high static orientational disorder, there is an increase in the rate of early-time anisotropy decay relative to a perfectly ordered system, due to increased depolarization with each site-to-site hop. Nevertheless, static orientational disorder leads to a similar decrease in exciton diffusivity over time as is observed with energetic disorder. This relationship may be less intuitive for orientation disorder than for energetic disorder, as the symmetry of the κ^2 term in the FRET rate between two chromophores implies that it is symmetric in the forward and reverse directions, precluding "trapping" on an individual site. As a result of the orientational disorder, however, there emerge groups of consecutive sites with favorable dipole orientation, and the (relatively) low κ^2 at the boundaries of these groups has a trapping effect on excitations which enter these "wells." Indeed, over a population with a highly disordered Gaussian TDM orientational probability distribution of width $\sigma_\alpha = 90°$, the average of the minimum κ^2 between neighbors on each ring is 2% of the average of all such κ^2 values. So, as excitations migrate and explore the orientational space, over time they tend to spend more time trapped in these subsections of the ring rather than freely diffusing, which limits the long-range mobility of excitations. Once the excitations have fully explored the space, however, we recover diffusive transport limited by the relatively slow well-to-well hopping rather than the faster site-to-site transfer. Again in the $\sigma_\alpha = 90°$ case, the final diffusivity is 23% that of the long-time diffusivity obtained for $\sigma_\alpha = 0°$. In comparison, natural LHCs precisely control the orientations of their chromophores through steric effects and hydrogen bonding with specifically placed residues; we believe this fine control over orientation is necessary for efficient long-range energy transfer. This reflects what Sarovar and Whaley have studied in detail – that control over orientation is essential to optimize energy transfer in the presence of disorder in such LHCs.[102]

3.4.2 Uncoupled chromophores present barriers to long-range energy transport

The lack of configurational control of the chromophores, i.e., their physical configuration relative to the protein, in this system is what we hypothesize to be the source of disorder in the degree of coupling between chromophores, which similarly impacts long-range energy transport by producing barriers to transport. The introduction of this disorder to our model is justified phenomenologically. First, it captures the singly-labeled-like fluorescence component observed in the fully-labeled LHCs. Second, the long-lived anisotropy cannot be accounted for by orientational and energetic disorder alone. The subpopulation of initially-excited chromophores that are poorly coupled to the majority of others would fluoresce identically to the singly-labeled controls, and would remain highly anisotropic over the course of the TAA measurement. A lack of control over the position of the chromophore could manifest this disorder, leading some chromophores to adopt positions sufficiently far from the others to greatly reduce FRET coupling due to the $1/R^6$ dependence. For example, as shown in Fig. 3.1(a), chromophores configured anomalously to reside near the pore of the protein ring would be approximately 1.5× the distance from their neighbors as those residing far from the pore. Adopting a configuration which places more protein between the chromophores would further reduce the FRET coupling due to protein's typically higher index of refraction compared to water (1.66 versus 1.33) and the $1/\eta^4$ dependence of the FRET rate. In terms of energy transfer, the effect of these uncoupled chromophores is similar to that of orientational disorder, effectively dividing the ring into wells. Escaping such a well requires bypassing an uncoupled chromophore via next-nearest-neighbor hopping.

Thus far, our model suggests an encouraging capacity for remarkably fast site-to-site energy transfer in the synthetic LHC, but that it is limited in range due to ensemble disorder. This fast hopping rate, averaging 1.6 ps^{-1}, is due to the 1.5 nm site-to-site separation, which places the chromophores (with an average R_0 of 6.5 nm) close enough together to allow FRET efficiencies in excess of 99%. Viewed in isolation, this site-to-site rate is in fact faster than the incoherent hopping rate of 0.67 ps^{-1} reported between B800 molecules in antenna complexes of *Rhodobacter acidophila*,[85] demonstrating the strong potential of the synthetic LHC (though slower than the coherent energy transfer rate of >13 ps^{-1} in the B850 aggregate). As counterpoints, as can be seen in Fig. 3.7(c), these hops occur on limited subsets of the ring due to barriers presented by static disorder, and a well-known side effect of placing chromophores close together without the benefit of photosynthesis' billions of years of pigment-protein complex evolution is nonradiative contact quenching. Indeed, we observe signatures attributable to moderate quenching in both transient absorption and fluorescence, seen as an increase in the rate of signal decay relative to the singly-labeled controls. In singly-labeled controls, the TA signal decays with a slow component of 1.8 ns, while in the fully-labeled LHCs we observe a multiexponential decay with two slow components of 97 ps and 870 ps, as listed in Table 3.1. In natural light harvesting systems, it is not fully understood how such quenching is avoided. In such systems, however, chromophores are most commonly found in pockets within the protein, not covalently linked to the surface. In our biomimetic LHCs, then, it appears the same lesser control over chromophore orientation and position that impacts long-range exciton migration could also play a role in allowing this aggregation and subsequent quenching to occur.

3.5 Outlook and future prospects for cpTMV LHCs

Regardless, our findings suggest that protein scaffolds such as cpTMV, combined with judicious chromophore conjugation, are promising systems for both studying and imitating the efficiency of energy transfer in LHCs. In this study we have demonstrated energy transfer in a modular biomimetic LHC with inter-chromophore energy transfer rates slower than but comparable to natural systems and used kinetic Monte Carlo simulations to describe the key sources of disorder affecting energy transfer in this system. Through the modularity of the system, these key sources of disorder that must be controlled to optimize energy transfer in biomimetic LHCs are: site energy, chromophore orientation, and chromophore coupling. While we showed previously that rigid linkers are capable of slowing vibrational relaxation, which can contribute to improved energy transfer, this study demonstrates that control over the specific chromophore orientation and configuration relative to the protein & to other chromophores remains critical to optimize exciton migration. In particular, fine control over the configuration of chromophores, as occurs in natural systems, will be necessary to prevent the poorly-coupled chromophores that we identified have to hinder exciton migration. Furthermore, we uncovered a potential design principle to ensure robustness to disorder in systems relying on exciton diffusion on a discrete periodic lattice, as in purple bacteria. We find that a smaller period (number of sites on a ring) allows the photoexcitation to equilibrate more rapidly in the presence of disorder, reducing the impact of disorder on long-range energy transfer.

Based on the above findings, one could evaluate and improve the energy transfer performance of model light-harvesting complexes. First, the significant role of static disorder in affecting long-range energy transport points to the need to develop biomimetic LHC strategies beyond restricting chromophore motion and focused on specifically and repeatedly orienting chromophores in the biomimetic LHC structure. For instance, placing chromophores inside a protein cavity might soon become possible by breaking the C_2 symmetry of a disk-like structure like the one employed here. This type of advance would enable investigation of systems more closely resembling natural LHCs. Second, the extensibility of biomimetic LHCs across many scales of organization, from individual chromophore-protein systems, to fully-labeled isolated LHCs, to supercomplexes of LHCs arrayed in films or rod geometries, will continue to enable the study of interactions involved in long-ranged light harvesting through a bottom-up approach. For example, coupling biomimetic LHCs together asymmetrically, allowing for the creation of supercomplexes of different types of disks (e.g., “donor” and “acceptor” disks), might further mirror the membrane-bound systems found in light-harvesting bacteria. Furthermore, combining TAA and TRES with new techniques, such as transient microscopy, should allow energy transfer in such super-complexes to be tracked directly in space, building a ground-up picture of efficient energy transfer in LHCs and heterogeneous systems more broadly and over more scales than is possible with time-resolved spectroscopy alone.

Chapter 4

Implementing ultrafast stroboSCAT for spatiotemporally resolving energy migration in LHCs

With the understanding gained from studying intra-protein energy transfer in our model LHC, we next aimed to better understand long-range, inter-protein energy transfer in natural LHCs, as will be detailed in Chapter 5. In order to do so, we required a technique capable of spatiotemporally resolving photogenerated excitations in natural photosynthetic systems on picosecond time scales and with nanometer sensitivity. In this chapter, we detail the implementation of such a technique by extension of a time-resolved scattering microscopy to picosecond time resolution. In Section 4.1, we introduce the principles behind this microscopic technique, then in Section 4.2 we detail the improvements made to our apparatus to increase time resolution to below 1 ps. Finally, in Section 4.3, we explore the effects of carrier-carrier scattering on charge carrier diffusion in silicon, leveraging this newly improved time resolution, and we report a notable artifact in these spatiotemporal measurements caused by the different diffraction-limited diameters of the pump and probe laser pulses that must be considered when analyzing the data.

4.1 Introduction to iSCAT and stroboSCAT

Stroboscopic interferometric scattering microscopy,[58] stroboSCAT, is a time-resolved extension of interferometric scattering microscopy developed in the Ginsberg group that is used to image, in real space, the time-evolution of photogenerated energy carriers following excitation of a diffraction-limited volume by a focused laser pulse. The technique has been described in detail previously,[58] but for completeness a brief description of the principles of stroboSCAT is included herein.

4.1.1 Interferometric Scattering Microscopy, AKA iSCAT

Underlying the technique of stroboSCAT is interferometric scattering microscopy, or iSCAT. iSCAT is a powerful technique for imaging nano-objects, such as nanocrystals or single proteins. It employs a homodyne detection scheme that relies on interference between light scattered by the sample and a reference field, typically generated by transmission or specular reflection of the incident beam. Due to the near ubiquity of scattering (as compared to, for example, fluorescence), a major strength of iSCAT is its label-free nature and thus its ability to probe a wide variety of materials. In widefield reflection-mode iSCAT, i.e., the mode employed in this work, the measurement is performed in a reflection geometry, with a single objective used both to condense the beam incident on the sample and collect the scattered and reflected light. The setup for this configuration is diagrammed in Fig. 4.1(a). First, a coherent source (translucent red, labeled "Probe beam" in Fig. 4.1(a)) is focused on the back focal plane of the microscope objective, producing a collimated beam incident on the sample, which is the plane wave incident field $\boldsymbol{E}_i$. The light reflected off of the substrate-sample interface forms the reflected field $\boldsymbol{E}_r$, also translucent red in a plane wave, which constitutes the reference field for the interferometric measurement. Meanwhile, some of the light transmitted beyond the substrate-sample interface is scattered by the sample, resulting in a scattered field $\boldsymbol{E}_s$, depicted as a green translucent field in Fig. 4.1(a). The scattered and reflected fields are collected by the objective, then focused by an imaging lens to form an image plane at the camera.

At the camera, the scattered and reflected fields interfere to form the detected image. The detected intensity I_{det} is given by the expression:

$$I_{\text{det}} \propto |\boldsymbol{E}_r + \boldsymbol{E}_s|^2 = |\boldsymbol{E}_r|^2 + |\boldsymbol{E}_s|^2 + 2E_r E_s \cos\phi, \tag{4.1}$$

where E_r and E_s are the scalar amplitudes of the reflected and scattered fields, respectively, and $-\pi \leq \phi \leq \pi$ is the phase difference between the two fields, depicted on the left hand side of Fig. 4.1(a). A typical iSCAT image can be seen in Fig. 4.1(b). The phase can be broken down further into three components, given by the following:

$$\phi = \phi_{\text{Guoy}} + \phi_z + \phi'_{\text{scat}} \tag{4.2}$$

where ϕ_{Guoy} is the Guoy phase shift, ϕ_z is the phase shift due to propagation, and ϕ_{scat} is the scattering phase shift. The Guoy phase shift ϕ_{Guoy} is a property of the imaging system which arises due to the different beam waists in the paths of the reflected and scattered light, but for the purpose of this work it can be regarded as constant. The phase shift due to propagation ϕ_z is a result of the scatterer being displaced along the optical axis relative to the reference; it can be calculated by relating the additional round-trip distance relative to the reference beam ($2z$) to the wavelength of the light in the sample medium λ/n, where n is the real refractive index of the sample:

$$\phi_z = \frac{4\pi n z}{\lambda}. \tag{4.3}$$

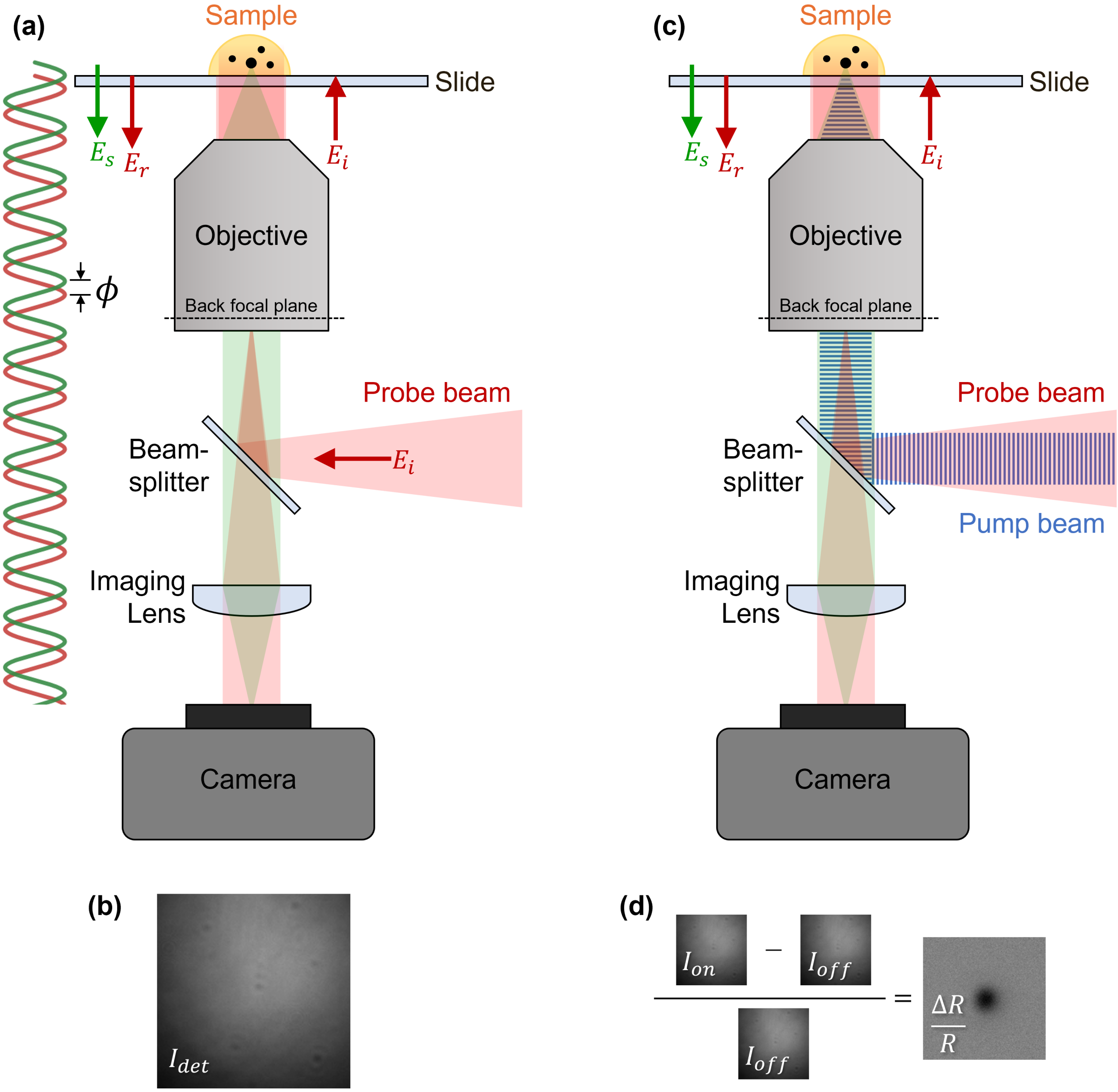

Figure 4.1: A diagram of the principles of iSCAT and stroboSCAT. (a) Diagram of iSCAT microscope, showing incident and reflected field (red) and scattered field (green) and (b) iSCAT measurement of dust motes on a slide as a demonstration. (c) stroboSCAT diagram, with same coloring as iSCAT diagram but with added pump beam (blue striped), and (d) schematic representation of differential measurement taken during stroboSCAT.

While this depth-dependence is a great strength of iSCAT and has led to many interesting results such as three dimensional tracking of charge carriers in polycrystalline perovskites[59] or protein and virus motion on the nanoscale,[103,104] the bulk of the information of interest for time-resolved iSCAT experiments is a result of the scattering phase shift ϕ_{scat}. This phase shift is caused by the scatterer's response to the incident electric field, which depends on its complex refractive index. Far from any optical resonances, the scattering phase is small but nonzero, with its sign dependent on the incident field's frequency relative to nearby resonances.

As will be demonstrated further on, while the scattering phase shift is small far from resonance, where stroboSCAT measurements are typically probed, it nonetheless produces an effect sufficiently strong to perform these measurements on a wide variety of materials. The key to understanding this high sensitivity, one of the key strengths of iSCAT, is in the linear dependence on the scattering field amplitude E_s in the cross term of Equation 4.1. For a spherical nano-object (smaller than the wavelength of the probe), the strength of the scattered field is proportional to the volume of the nano-object, and thus decreases by the cube of the radius.[104] In order to isolate the signal from a small scatterer, it is necessary to remove the large contribution from reflected light, $|\boldsymbol{E}_r|^2$. Typically for conventional iSCAT measurements, this involves measuring the reflected field without sample present,[105] or performing frame-to-frame subtractions to extract the accumulation of sample at the surface over time.[106] This reflected field, however, is typically orders of magnitude stronger than the field scattered by a nano-object. Thus the squared dependence on the field strength in the direct measurement of the scattered field, as might be measured in darkfield microscopy, makes $|E_s|^2$ vanishingly small and easily lost to noise. The iSCAT contrast C is given by considering the signal detected with (I_d) and without (I_r) the scatterer present,[104] and, due to the dominance of the linear cross-term over the square scattered field term, is well-approximated by:

$$C = \frac{I_d - I_r}{I_r} \approx 2\frac{E_s}{E_r}\cos\phi \tag{4.4}$$

Thus the interferometric cross term, with its linear dependence on the scattered field strength, is key to the ability to image small scatterers with this technique.

4.1.2 Stroboscopic iSCAT, AKA stroboSCAT

Stroboscopic iSCAT, or stroboSCAT, is a time-resolved extension of iSCAT developed in the Ginsberg group that leverages its sensitivity and label-free nature to directly probe populations of a wide variety of photogenerated energy carriers as they evolve in time following photoexcitation. In stroboSCAT, the continuous-wave probe beam is replaced by a pulsed laser source, and a pulsed, colinear pump beam is introduced, shown as a blue striped field in Fig. 4.1(c). Whereas the probe beam is focused onto the back focal plane of the objective, the pump beam is collimated as it enters the objective. Thus, the objective focuses the pump beam to a diffraction-limited spot at the sample plane.

The measurement proceeds in a pump-probe configuration. When a focused pump pulse is incident on the sample, it generates a volume of energy carriers a few hundred nanometers in diameter. Some time delay t later, the widefield probe pulse arrives and is used to collect an iSCAT image of the sample around this volume of excited carriers, which could be excitons or free electrons and holes. This iSCAT image is the "pump-on" measurement I_{on}. The pump pulse passes through an optical chopper that is synced to half the repetition rate ν_{rep} of the camera, such that with every other exposure, the pump is blocked and the probe pulse images the sample in the ground state instead. This iSCAT image is the "pump-off" measurement I_{off}. The stroboSCAT signal is then the difference between these consecutive pump-on and pump-off iSCAT images, termed $\Delta R/R$, as follows:

$$\frac{\Delta R}{R}(t) = \frac{I_{\mathrm{on}}(t) - I_{\mathrm{off}}(t)}{I_{\mathrm{off}}(t)} \tag{4.5}$$

A schematic representation of this calculation is shown in Fig. 4.1(d) to demonstrate a typical stroboSCAT measurement at some positive time t. This subtraction effectively performs the same task of removing the reflected field in a traditional iSCAT measurement. Rather than isolating the signal due to a small scatterer such as a single protein, however, the subtraction isolates the signal due to the small volume of energy carriers. These energy carriers locally modify the optical polarizability of the sample, and thus its scattering response, which is ultimately what gives rise to the contrast observed in stroboSCAT. Crucially, this effect is essentially ubiquitous for any type of excitation, from free carriers and excitons,[58,59] to exciton-polaritons and phonon-polaritons,[107,108] to sound waves, and even to heat,[63] to combinations of these types,[61] and to more exotic quasiparticles,[109] which gives stroboSCAT its wide applicability to a variety of samples.

By varying the time delay t between the pulses, a series of these differential images are collected at different time delays in order to build up a "movie" of the energy carriers' evolution following excitation by the pump pulse. A more complete description of the procedure for taking a stroboSCAT measurement is found below in Section 4.2.5.

4.2 Improving the time resolution of stroboSCAT

In order to apply stroboSCAT to photosynthetic systems, it was necessary to make upgrades to the stroboSCAT system. A main limitation in the original stroboSCAT configuration was the time resolution. To overcome this limitation, major upgrades were implemented in order to couple in an ultrafast laser source, resulting in an increase in time resolution by more than two orders of magnitude. These upgrades were made alongside fellow Ginsberg lab members Dr. Rongfeng Yuan and Dr. Stephanie Hart, with the help of Dr. Hannah Weaver whose graduate work centered on the development and use of the original stroboSCAT system.[110] The resulting setup is modular, allowing the choice between ultrafast pumping and probing via either of two noncollinear optical parametric amplifiers to capture various electronic excitations or diode laser-based measurements with lower time resolution but higher dynamic range helpful to study heat transport. Improvements to the optical path to allow higher repeatability in alignment and greater image quality, as well as updates to the LabVIEW acquisition software, resulted in overall improvement to the data quality in all imaging modes. Details of each of these upgrades are explored below.

4.2.1 The original diode laser setup: high dynamic range, limited temporal resolution

When the project of imaging photosynthetic systems in this apparatus began, the stroboSCAT microscope remained in much the same configuration as when it had first been built. This compact setup relied on two single-wavelength pulsed diode lasers (PicoQuant, LDH Series) as the pump and probe sources, with the time delay, pump modulation, and camera triggering controlled via a Sepia 828 picosecond diode laser (PDL) driver (PicoQuant).

This setup is diagrammed in Fig. 4.2(a). In brief, the pump beam is passed through a spatial filter, which consists of a pair of lenses (a telescope) with a narrow pinhole placed at the focal (Fourier) plane. The telescope expands the beam to the appropriate size to fill the back aperture of the objective, while the pinhole placed in the Fourier plane removes all spatial components except the lowest frequency, approximately Gaussian spatial mode. The probe beam is similarly passed through a spatial filter to achieve a clean Gaussian mode, and then through the widefield lens, which focuses the beam onto the back focal plane of the objective. Following the widefield lens, the pump and probe beams are brought into coaxial alignment by a dichroic mirror. Underneath the home-built sample stage,[59] as diagrammed in Fig. 4.3, a 50/50 beamsplitter reflects the pump and probe into the objective, and the reflected and scattered fields then pass back through the objective and transmit through the beamsplitter. The final lens, the imaging lens, has the same focal length as the widefield lens and is placed at the same distance from the objective as the imaging lens, which focuses the iSCAT image onto the camera. A spectral filter is placed before the camera to block the pump beam.

In this setup, all of the timing is controlled electronically via the Sepia 828 PDL driver, as shown in Fig. 4.2(b). The driver is configured to pulse the pump and probe lasers at a desired repetition rate (up to 40 MHz), with measurements typically performed at 2 to 4 MHz. The driver also controls the time delay t by applying a signal delay to the probe triggering signal relative to the pump. In addition, the driver emulates optical chopping by amplitude-modulating the pump triggering with a square-wave of frequency ν_{chop}. The camera acquisition is then triggered off of a pulse-wave synchronization signal generated by the PDL driver at a frequency of $2\nu_{\text{chop}}$, such that every exposure alternates between pump-on and pump-off. The frequency ν_{chop} is limited by the acquisition frame rate of the camera, which for a typical 192×192 region of interest, is around 690 Hz. In order to ensure sufficient time for readout between exposures, a slightly slower camera triggering rate of 660 Hz is typically used. Thus the typical pump modulation frequency ν_{chop} is 330 Hz. Because

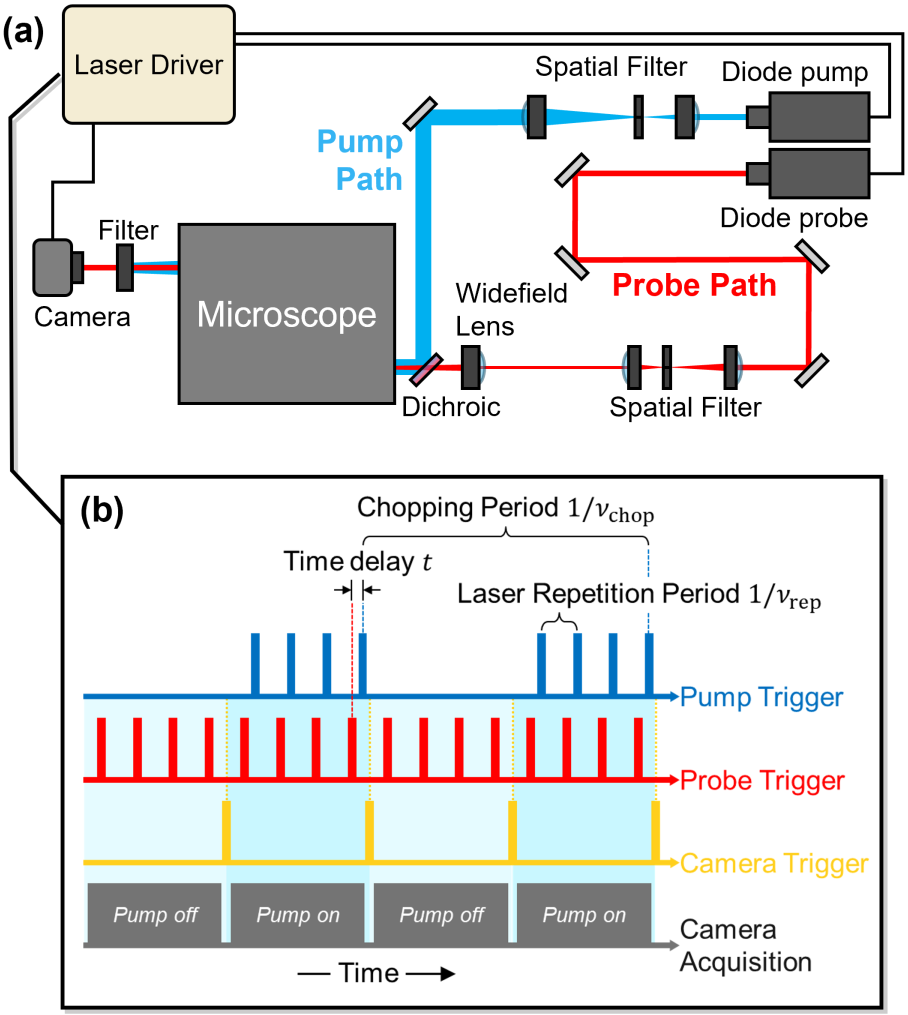

Figure 4.2: Schematic diagram of original diode laser-based stroboSCAT setup. (a) Simplified beam diagram of diode laser-based stroboSCAT microscope, with (b) schematic of timing signals and camera acquisition (times not to scale).

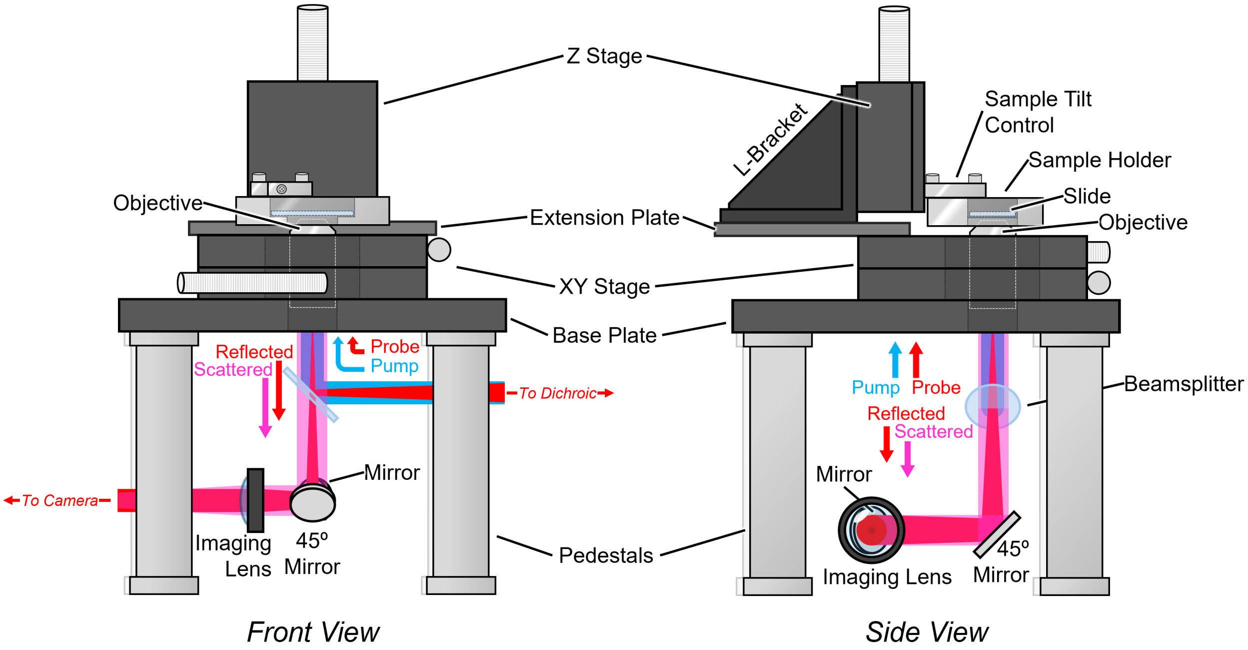

Figure 4.3: Diagram of homebuilt 3-axis microscope stage used in stroboSCAT. Scattered field, shown in magenta, contains both iSCAT scattered signal and scattered pump signal until pump light is filtered by spectral filter placed before camera (see λF in Fig. B.1). Z stage is a manual/piezoelectric micrometer stage, while x- and y-stages are manual micrometer stages.

the camera acquisition rate is much slower than the repetition rate of the laser, exposures are not collected shot-to-shot, and instead many probe pulses are collected and thus averaged for each exposure. While higher repetition rates are generally preferred for increasing the SNR, the choice of repetition rate is usually limited by the robustness of the sample, since higher repetition rates may damage a sample. The excited state lifetime of the sample can also be a limitation on the acquisition rate, since enough time must elapse between successive pump pulses to allow the sample to fully return to the ground state (and dissipate heat, if necessary).

Last, a small amount of the pump beam is "picked off" by a slightly reflective 1 mm glass window, focused to a small spot by a lens, and sent directly into the camera, typically placed at one corner of the exposure area. This spot serves as a reference to encode which frames are pump-on and which are pump-off. When a measurement is taken, a series of exposures are read off the camera in a single stream, and while the synchronization between camera and chopper ensures that each frame will alternate between pump-on and pump-off, the "phase" of this signal is ill-defined, as the first frame in the stream may be either one. Because stroboSCAT signals may be positive or negative, and may even change from positive to negative, the sign of the stroboSCAT signal cannot be used to "phase-lock" this signal.

By directing pump light directly into the camera, a positive "bright" spot will always be present in the pump-on images, allowing proper phase-locking of the signal to ensure the differential contrast is always calculated correctly.

This diode laser-based stroboSCAT configuration has several advantages. For one, its relative compactness reduces the angular degrees of freedom of the optical path, which increases the microscope stability by reducing the impact of vibrations and temperature fluctuations. The diode laser sources are stable and reliable, and the wide range of available wavelengths and ease of swapping out diode sources allows both pumping and probing across a comfortable range of wavelengths, albeit restricted to a discrete set. The high repetition rates of these sources allow high SNR measurements in short acquisition times. Finally, electronic control of the pump-probe delay allows virtually unlimited dynamic range in the time delay, out to hundreds of nanoseconds,[63] with ease. In fact, the delay is limited only by the amount of time between laser pulses, which is also electronically configurable, allowing delays out to microseconds or even milliseconds for lower repetition rates.

Despite these many advantages, the diode laser sources present a considerable limitation due to the laser pulse width, which limits the time resolution of the experiment to about 100 ps, as explained in Section 2.1.2. In order to image the energy carrier expansion at the earliest steps in photosynthesis, which may proceed as fast as 10-100 ps, it was necessary to overcome this limitation in temporal resolution imposed by the diode laser sources.

4.2.2 Coupling in the ultrafast laser source

In order to increase the time resolution of the stroboSCAT microscope, it was necessary to use a laser source with a shorter pulse width than the diode lasers. Thus, an ultrafast laser source was coupled into the microscope, which required some significant re-configuration and which introduces additional trade-offs.

To bring the time resolution from hundreds of picoseconds to hundreds of femtoseconds, the goal was to substitute in a 200 kHz, 1030 nm regenerative amplifier source (Light Conversion, Pharos model) seeding two noncollinear optical parametric amplifiers (NOPA) for the pump and the probe. One NOPA (Light Conversion, Orpheus-N 2H, also known as "2H") is pumped by 515 nm second harmonic generation of the regenerative amplifier fundamental beam, and acts as a tunable source for light of relatively low photon energy (650 - 900 nm) but high pulse energies near 1 µJ/pulse. The second NOPA (Light Conversion, Orpheus-N 3H, also known as "3H") is pumped by 268 nm third harmonic generation of the regenerative amplifier fundamental, enabling it to access higher energies (520 - 900 nm) but with a lower power conversion efficiency, limiting pulse energies to around 0.25 µJ/pulse.

The 2H and 3H beams were picked off of their existing paths by the addition of two mirrors attached to drop-in kinematic mounts, which allows for toggling between their use in stroboSCAT and in the existing time-resolved super-resolution microscope[100,111] on the same laser table. In the "default" configuration, shown in Fig. 4.4(b), the 3H beam is used as the pump, and the 2H beam is used as the probe. Furthermore, four additional drop-in

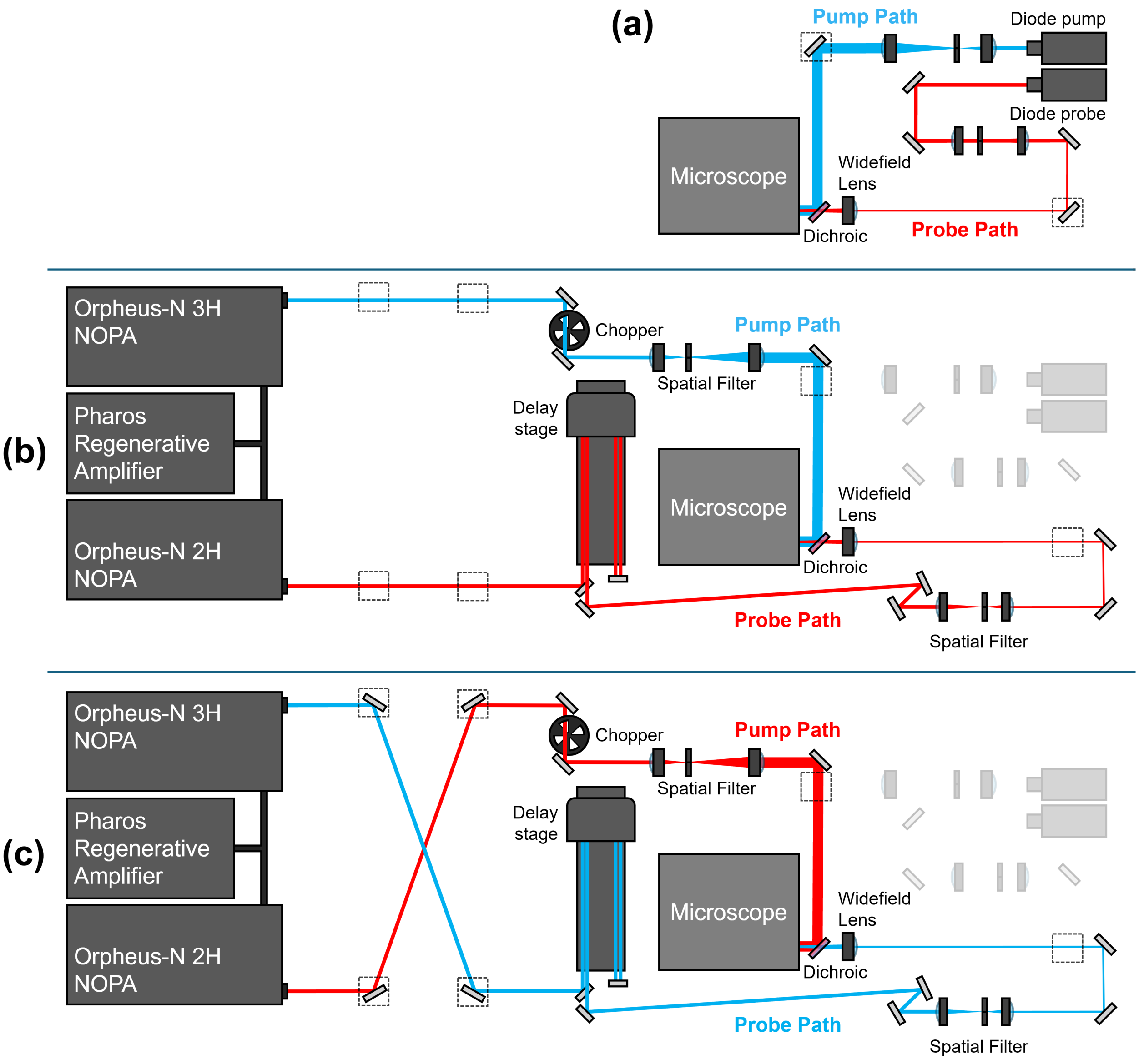

Figure 4.4: Simplified optics diagram of the three stroboSCAT configurations: (a) Diode laser stroboSCAT, (b) Ultrafast stroboSCAT with 3H pump and 2H probe, and (c) Ultrafast stroboSCAT wtih 2H pump and 3H probe. Dashed squares indicate kinematic mirror mounts for swapping between configurations.

kinematic mounts were added to the setup to allow swapping the 2H and 3H if a higher photon energy probe is desired, as shown in Fig. 4.4(c).

In the sub-picosecond domain, electronic control of pump-probe delay is infeasible due to the limited bandwidth of electronic circuits, and thus optical control of the delay is necessary. To this end, near the end of the probe path, the beam is sent into an optical delay stage (Newport Corporation ILS 250 CC) in a double-pass configuration. The beam is directed into the retroreflector by a square mirror; the parallel reflection returning is then sent back into the retroreflector by a roofed mirror that jogs the beam vertically, allowing the reflection out to clear the top of the square mirror and continue down the beam path. This double-pass configuration doubles the dynamic range of the microscope, allowing 4×250 mm total path length extension, equating to 3.33 ns of delay. This does come at the cost of decreased time resolution; however, with a manufacturer-specified minimum incremental motion of 1 µm, corresponding to 13 fs of delay, this cost is negligible compared to the IRF. In contrast to ultrafast spectroscopy, the probe is delayed rather than the pump because in practice it is very difficult to avoid small deviations in the beam propagation direction as a function of delay stage position. Such deviations in the widefield probe position are small compared to the large size of the beam at the sample and are largely cancelled out by the $I_{\text{on}}/I_{\text{off}}$ differential calculation, while even small deviations in the focused pump position would cause the signal spot to change position with delay, which would greatly complicate analysis.

Pump modulation is achieved by use of an optical chopper wheel (Newport Corporation 3502) placed before the pump spatial filter. For timing control of the chopper, the same Sepia 828 driver is used for its high-quality timing electronics. In this configuration, however, the Sepia is just used to generate the 660 Hz pulse-wave synchronization signal, which is split and used both to trigger the camera acquisition and as the reference signal for the chopper controller, which performs the frequency halving internally to reach a chopping frequency of 330 Hz. The chopper controller also has a configurable phase parameter that sets the phase of the modulation relative to the reference signal, which is important to ensure that the chopper and camera are in sync.

After passing the chopper wheel and delay stage, respectively, the pump and probe beams are both passed through spatial filters as described in Section 4.2.1, in order to clean up the beam modes and bring the beam sizes to the same size as the diode beams. Last, the beams were inserted into the same optical path as the diode setup by replacing two existing mirrors with mirrors on drop-in kinematic mounts. These can be removed to allow the 2H and 3H beams to enter the microscope, and placed back in to instead use the diode laser beams. Neutral density (ND) filters are placed in the path of each beam in order to set the pump and probe fluences as desired.

An important improvement was made by moving the probe spatial filter before the last two mirrors in the path and adding two additional mirrors directly before the filter (compare Fig. 4.2(a) and Fig. 4.4(a)). In the original configuration, two mirrors were used to direct the probe beam through the spatial filter and into the microscope. This required the use of only two mirrors (a total of four degrees of freedom including pitch and yaw for each) to align the beam through the center of two lenses and the two input alignment apertures, for a total of eight constraints. The inability to align into the spatial filter and into the microscope independently required imperfect alignment through all four optics, compromising power throughput and image quality. This would not be a problem, in principle, if the lenses and the input alignment apertures were all in alignment with one another. In practice, however, it is not feasible, as the tolerances in pointing demanded by the 25 μm pinhole in the spatial filter are extremely tight, and even small deviations block any light from passing through. This simple change greatly improved image quality, increasing CMOS pixel photon counts by a factor of more than 2.5, by allowing more light to pass through the spatial filter without compromising alignment into the microscope.

In general, an optical setup can be thought of as a set of constraints (e.g., alignment targets) with a number of degrees of freedom (e.g., mirror rotations), and the purpose of aligning the setup is to optimize the path of the laser to fit the constraints by iteratively adjusting the degrees of freedom. From this point of view, it is important to ensure that the number of degrees of freedom equals the number of constraints, or else it may not be possible to satisfy all constraints simultaneously. A countervailing factor in this framework is that increasing the degrees of freedom of the system tends to decrease the overall stability in the presence of environmental noise, such as vibrations or thermal drift. The construction of a stable apparatus thus requires minimization of both the degrees of freedom and the constraints. Ideally, then, a short optical path length with as few kinematically-mounted optics as possible would be ideal to ensure the most robust apparatus.

4.2.2.1 LabVIEW integration

Finally, changes had to be made to the custom LabVIEW program that runs the stroboSCAT microscope. The most significant change required was to replace the electronic delay control with the optical delay stage. Previous LabVIEW code had been written to control the same model of optical delay stage, so fortunately many functions could be reused. The delay stage is controlled via a Newport XPS-C6 Motion Controller / Driver, which communicates via TCP/IP with the stroboSCAT computer. The Newport XPS Labview library provides motion control functionality, such as initialization and positioning. Using this library, our set of custom LabVIEW functions allow the following:

- Absolute and relative positioning of the retroreflector, either in position units (i.e., millimeters) or temporal units (i.e., picoseconds)
- A persistent time-zero value that can be set before each measurement
- Programmatic positioning of the delay stage, to allow a scan over several pre-set delays

Several further improvements were made, such as the ability to randomize time delays to prevent real-time drift (e.g., slow fluctuations in laser power, or lab temperature/mechanical drift, etc.) from imprinting on the time delays in the measurement. In addition, a custom

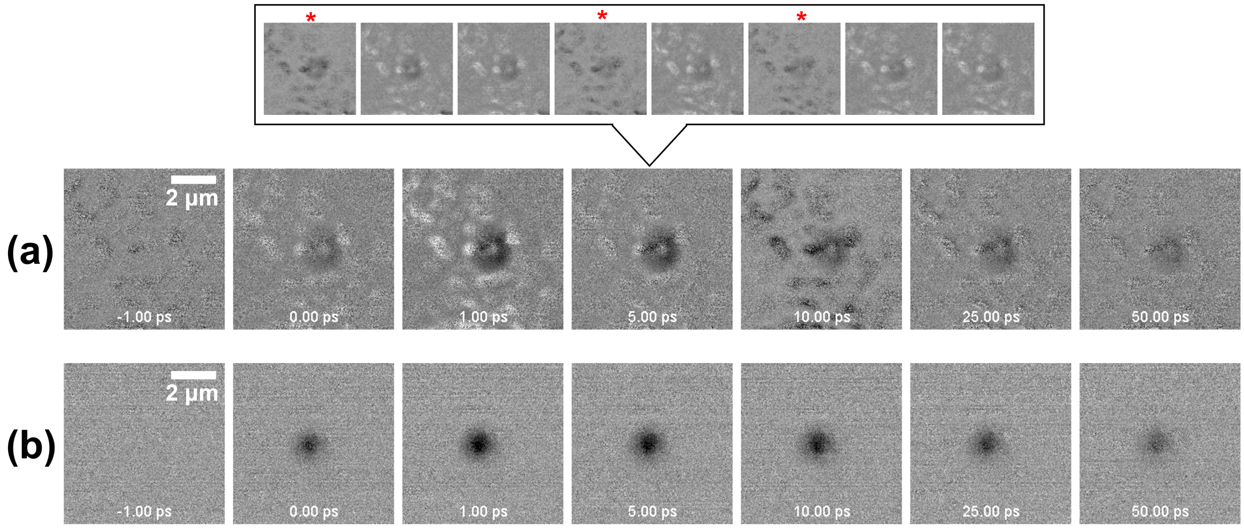

Figure 4.5: StroboSCAT images of thylakoid membrane (a) before and (b) after changing LabVIEW averaging routine. Callout box shows the individual measurements averaged together to form the 5 ps time point in (a), demonstrating the issue with averaging the arithmetic mean (brighter images) and the harmonic mean (darker images, asterisked) interchangeably.

LabVIEW program was written for aligning the system, which allows toggling between full-field-of-view untriggered mode and a small-ROI triggered mode, with GUI placement of the stroboSCAT ROI. A suite of ImageJ macros for averaging scans and performing background subtraction was also written, which allow near-real-time viewing of scan progress, such as monitoring the SNR, performing peak-fitting analyses mid-scan, and identifying and fixing issues such as defocusing.

An important improvement was also made to the stroboSCAT LabVIEW program's approach to the processing of the $I_{\text{on}}/I_{\text{off}}$ differential calculation. As described previously in Section 4.2.1, in a single stroboSCAT measurement, a large number of camera exposures, alternating pump-on and pump-off, are read off of the camera, and in order to determine which half are pump-on, a small amount of pump light is focused into one corner of the exposure region. Originally, the algorithmic workflow proceeded as follows:

1. Collect an array of images of length $2n$ from the camera, consisting of alternating pump-on and pump-off frames

2. De-interlace this array of frames into two image arrays of length n: I_1 and I_2

3. Compute the differential image array I_D of length n by dividing I_1 by I_2 element-wise, i.e., $I_{D,i} = I_{1,i}/I_{2,i}$

4. Compute the average differential contrast $\langle I_D \rangle$ by averaging the differential image array, i.e., $\langle I_D \rangle = \frac{1}{n} \sum_{i=1}^{n} \frac{I_{1,i}}{I_{2,i}}$

5. Compare the average values D_r and D_b of two ROIs in $\langle I_D \rangle$ containing the reference beam spot and pure background, respectively:
   a) If $D_r > D_b$, this is expected behavior as the reference should always be brighter, so return $\langle I_D \rangle$, or
   b) If $D_r < D_b$, this means the phase was incorrectly matched, so return the reciprocal of the differential contrast $\frac{1}{\langle I_D \rangle}$.

This workflow contains a flaw, however, in the final step. The value we wish to compute is the arithmetic average of the frame-to-frame differential contrasts:

$$\left\langle \frac{I_{\text{on}}}{I_{\text{off}}} \right\rangle = \frac{1}{n} \sum_{i=1}^{n} \frac{I_{\text{on},i}}{I_{\text{off},i}}. \tag{4.6}$$

Yet, because the average is taken *before* the algorithm decides whether or not I_1 corresponds to I_{on} or I_{off} (and vice versa for I_2), what is returned in case (b) of Step 5 is in fact the following:

$$\frac{n}{\sum_{i=1}^{n} \frac{I_{\text{off},i}}{I_{\text{on},i}}}, \tag{4.7}$$

which is the harmonic mean (the reciprocal of the mean of the reciprocals, commonly encountered in the calculation of reduced mass) of the frame-to-frame differential contrasts. Both the arithmetic mean and harmonic mean are linearly homogeneous, and thus this error does not impact the linear response to the differential signal besides adding some unwanted stochastic variance in the signal amplitude. However, according to the mean inequality chain,[112] for any population of values, the harmonic mean is always less than or equal to the arithmetic mean, with equality only holding when the population is entirely equal to one. When the background is not noisy (such as when measuring a smooth piece of silicon), the background value of $\frac{I_{\text{on}}}{I_{\text{off}}}$ is nearly uniformly unity, and the different averaging approaches result in the same background, presenting no issue. But when the background subtraction is imperfect, as for a rough and bumpy thylakoid membrane, these quantities differ significantly. This situation results in the background artifacts in each measurement changing in amplitude depending on whether the harmonic or arithmetic mean was taken. The result is that in the final scan for any time point, obtained from averaging these measurements, the background amplitude will randomly vary based on what portion was arithmetically versus harmonically averaged, which makes removal of the background practically impossible. If background artifacts overlap the signal, the excitation population appears distorted, compromising the quantitative analysis of energy transport and other time-dependent properties. This issue can be seen in the callout box above in Fig. 4.5(a), which shows the individual measurements to be averaged to obtain the called out stroboSCAT scan. These images show that the background features randomly present as dark (marked with red asterisks) or bright (unmarked), depending on whether the harmonic or arithmetic mean was taken, respectively. Because the type of mean taken depends on whether the first frame collected was pump-on or pump-off, which is random, the background of the resulting averaged frame varies wildly as seen in Fig. 4.5(a). To fix this issue, the routine above was modified by swapping steps 4 and 5, such that the arithmetic mean is always returned. This single change lead to the improvement shown between Fig. 4.5(a) and (b).

4.2.3 Characterizing time resolution of ultrafast configuration

To characterize the IRF of the newly set-up ultrafast stroboSCAT microscope, the first measurements were made on a tried and true benchmark sample, a spin-cast film of 6,13-Bis(triisopropylsilylethynyl) pentacene, or, TIPS pentacene, an organic semiconductor. TIPS pentacene serves as an excellent benchmark because it has a long-lived excited state, is robust to laser exposure, and has been characterized extensively previously.[59,70,113,114]

A film of TIPS pentacene was spin-cast onto a coverslip and solvent-vapor annealed at 60°C, as described previously.[59] The sample is placed on the microscope and a crystalline region is located by inserting a half-wave plate into the probe path and rotating the polarization of the probe. The iSCAT signal of the crystal will vary between a light and dark state as the polarization is rotated. The half-wave plate is then rotated to maximize the iSCAT signal from the crystallite. A stroboSCAT scan was then taken with a pump wavelength of 540 nm and probe wavelength of 740 nm, with small time steps near time-zero in order to fully resolve the onset of the signal. Fig. 4.6(a) shows several differential images from this measurement, where the stroboSCAT signal is visible as a positive feature with a peak $\Delta R/R$ of 6×10^{-3}.

In order to determine the IRF from this measurement, a reconvolution fit is performed. As explained above, the stroboSCAT signal $S(t)$ is the convolution of the IRF and the "true" impulsive excited state decay of the sample. In the case of a Gaussian IRF and an exponential decay, this expression has an analytical solution:

$$S(t) = \frac{1}{2} S_0 \cdot e^{-\frac{(t-t_0)}{\tau}} \cdot e^{\frac{\sigma^2}{4\tau^2}} \cdot \left(1 + \mathrm{erf}\left(\frac{t-t_0}{\sigma} - \frac{\sigma}{2\tau}\right)\right), \tag{4.8}$$

where S_0 is the "true" initial amplitude of the signal, τ is the decay lifetime, σ is the width (standard deviation) of the IRF, and t_0 is the time delay at which the pump and probe are perfectly overlapped—in the experiment, the experimental delay is calibrated such that $t_0 \approx 0$, but the term is included in the fit to account for small deviations from this ideal. Because the convolution is a linear operator, multiexponential decay will lead to a signal that is a sum of terms resembling the expression above, with the same IRF parameters σ and t_0 but different amplitudes and lifetimes, i.e., for an N-exponential decay:

$$S(t) = \sum_{i=1}^{N} \frac{1}{2} S_{0,i} \cdot e^{-\frac{(t-t_0)}{\tau_i}} \cdot e^{\frac{\sigma^2}{4\tau_i^2}} \cdot \left(1 + \mathrm{erf}\left(\frac{t-t_0}{\sigma} - \frac{\sigma}{2\tau_i}\right)\right) \tag{4.9}$$

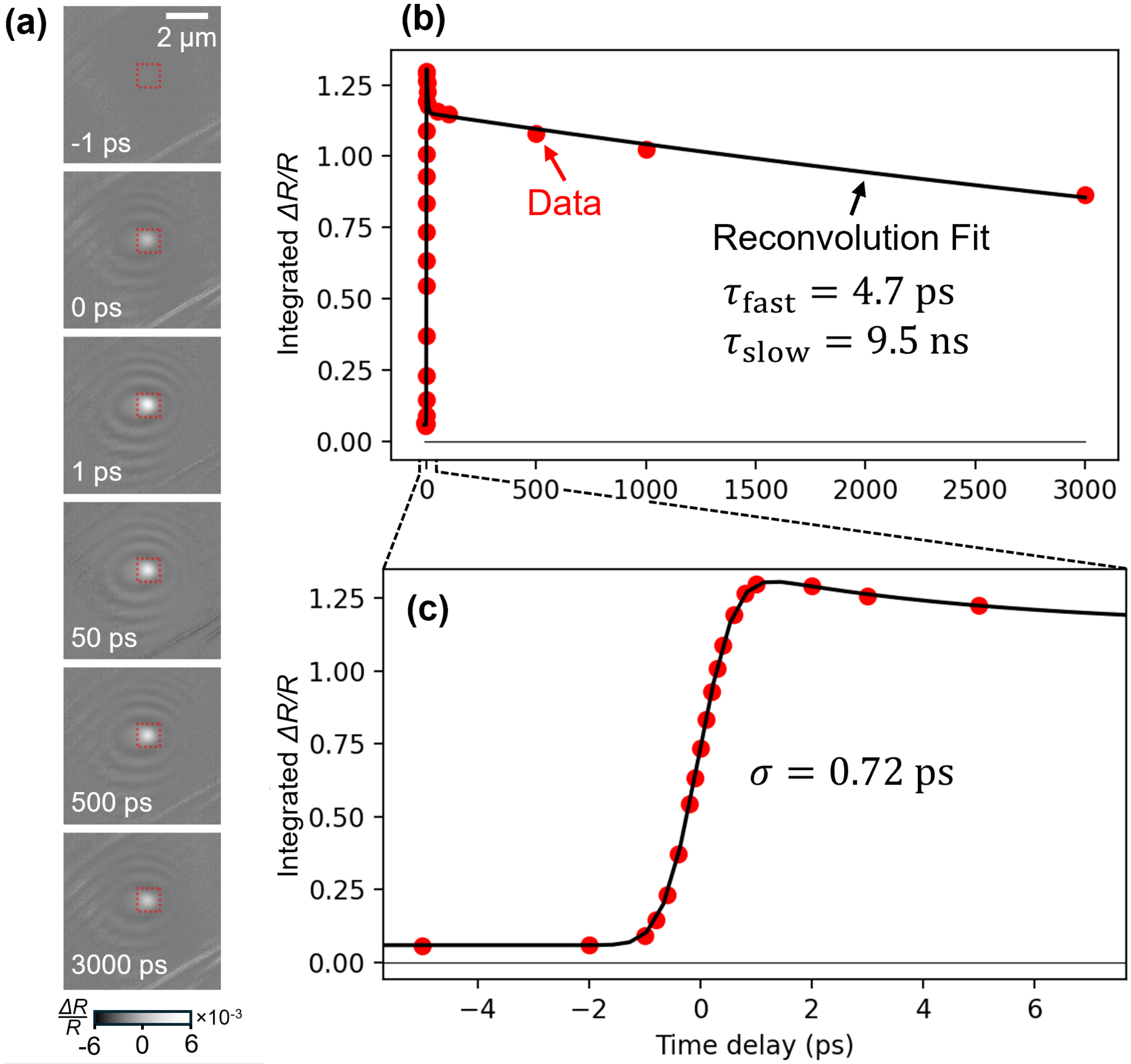

Figure 4.6: Benchmark stroboSCAT measurement on TIPS pentacene crystal domain, with pump and probe wavelengths of 540 nm and 740 nm, respectively. (a) Select frames from stroboSCAT scan showing signal onset and long lifetime, with peak integration region outlined in red dotted boxes. (b) Integrated differential signal plotted as a function of time (red dots) with biexponential reconvolution fit (black curve), and (c) zoom in on data and fit near time zero showing signal onset and IRF width.

This equation can thus be used to fit the time evolution of the stroboSCAT signal when it is able to be represented by a set of exponential decays.

To remove effects due to spatial migration of the photogenerated carriers, the positive signal in the red dotted boxes in Fig. 4.6(a) is summed, giving the integrated $\Delta R/R$ values as a function of time plotted as red points in Fig. 4.6(b). From this data it is clear that, following the signal onset, there is a very fast decay within the first 10 ps, followed by a much slower decay up to 3000 ps. The data were then fitted to a biexponential decay convolved with a Gaussian IRF, yielding the black curve. The fast decay is fit with a lifetime τ_{fast} of 4.7 ps and amplitude of 0.2, while the slow decay is fit with a lifetime τ_{slow} of 9.5 ns and amplitude of 1.1. Already, this benchmark measurement had revealed a decay feature that was fundamentally unresolvable in the previous iteration of stroboSCAT, demonstrating the newly unlocked capabilities that we could therefore access.

The IRF that gives rise to the signal onset shown in Fig. 4.6(c), is fit with a width of 0.72 ps, or a full width at half maximum of 1.7 ps. Thus, we achieved an increase in time resolution by two orders of magnitude over what had been possible previously. Still, further improvement could be possible by pulse compression. For the 500-800 nm, 20 nm bandwidth pulses produced by the 2H and 3H NOPAs, the transform limit for pulse width is in the 10s of femtoseconds, suggesting theoretical IRF limit of under 100 fs. In stroboSCAT, the main causes of dispersion are likely the lenses in the spatial filters and the microscope objective, the two of which likely contribute approximately equally to dispersion, considering the approximately equal amounts of glass presented by each. Dispersion is also introduced by the optics in the NOPAs, and the pulses output by the NOPAs are likely not transform-limited, though this could be fixed by optimizing the prism compressor in each NOPA. While the lenses could in theory be replaced by parabolic mirrors, the objective is inescapable and contains several centimeters of glass that both the pump and probe must pass through. In order to reach the transform limit, then, compressor arms would need to be added to both the pump and probe paths to pre-chirp the pulses and counteract the dispersion of the objective. Indeed, our IRF width is comparable to other ultrafast stroboSCAT microscopes that do not employ pre-compression,[115] while more recently others have reported stroboSCAT IRF widths as low as 129 fs by use of pre-compression via a pair of chirped mirrors.[108] Chirped mirrors would be an ideal approach to compress the pump and probe pulses in this setup due to the relatively few degrees of freedom a pair of such mirrors would introduce compared to a prism or grating compressor. While the dynamics of excitations in photosynthetic samples take place on the scale of few picoseconds or more, such high time resolution is not required; the option still remains for future improvement of the microscope's capabilities to measure even faster phenomena.

4.2.4 Modular setup addresses trade-offs

The new setup allows a high degree of modularity to accommodate a wide variety of measurements. The microscope can now be used in several configurations, to perform an ultrafast measurement with a higher-energy 3H pump and lower-energy 2H probe, an ultrafast measurement with a lower-energy 2H pump and higher-energy 3H probe, and a measurement with the original diode laser pump / diode laser probe configuration, with any combination of available diode laser sources. It would also be possible to perform the measurement with mixed sources (e.g., 2H pump and diode laser probe), with the timing of the diode laser source controlled by triggering it off of the ultrafast laser's synchronization signal, delayed by a digital signal delay generator, though a use case for such a configuration has not been found yet.

This modularity is important to address the various strengths and weaknesses of each configuration. As noted previously, the diode laser configuration has several advantages, including few degrees of freedom, high repetition rates up to 40 MHz affording high SNR, a wide array of available wavelengths spanning near UV to near IR, and electronic delay control affording virtually unlimited dynamic range out to microseconds or longer. On the other hand, the diode laser configuration suffers from limited time resolution around 150 ps, and while the range of available wavelengths is broad, the choices are limited to a discrete set.

In comparison, the ultrafast configuration benefits from much higher time resolution of <1 ps across a continuous range of wavelengths between 540-800 nm, but suffers from several drawbacks. For one, the repetition rate of the regenerative amplifier is 200 kHz, one order of magnitude below the typical diode laser measurement repetition rate of 2 MHz. Together with the need to limit the probe power to avoid damaging the objective (see below), this limits the single-shot SNR significantly in comparison to the diode laser configuration, with CMOS pixel photon counts typically 10× lower, corresponding to a $1/\sqrt{10}$ reduction in SNR. This is compounded by the instability of the ultrafast laser source, which is also much more sensitive to vibrations due to the long path length, though plans are underway to relocate the microscope and ameliorate this issue. In addition, the time delay dynamic range of the ultrafast configuration is limited by the delay line, to a maximum of around 3 ns. This could be increased by use of a longer delay stage and/or further doubled via a quadruple pass through the delay stage, though the benefit (3-4 additional nanoseconds of delay) is limited. In practice, it is much easier to measure long-lived signals using the diode laser configuration and short-lived ones on the ultrafast, and the two can and have be combined to measure both ranges on a single sample.

4.2.5 Details of a stroboSCAT measurement

StroboSCAT measurements begin with selection of an appropriate pump and probe source and wavelength. For diode laser stroboSCAT measurements, this consists of selecting the appropriate diode laser source, mounting it on the table, and aligning the setup. For ultrafast measurements, wavelength selection is performed by internal motorized mounts in the commercial 2H and 3H NOPAs, and placement of kinematic mounts (see Fig. 4.4(b) and (c)) to decide between each as pump and probe sources.

The objective in stroboSCAT is a 1.4 NA 63× high numerical aperture oil-immersion objective (Leica, HC PL APO 63×/1.40 OIL CS2). Before mounting the sample, power measurements may be taken at the sample position with a large-area microscope slide power sensor (Thorlabs, S170C), and pump and probe powers are set appropriately, either using electronic control for diode laser sources or by insertion of ND filters for ultrafast sources. With the ultrafast sources, additional care must be taken to limit the pulse energies allowed into the objective to avoid damaging it, due to the high peak field strength of the compressed pulses. The greatest risk is for the probe pulses, which are focused inside the objective (on the back focal plane) and thus present the greatest risk for optics damage. The objective has no manufacturer rating for maximum pulse energy for ultrafast pulses, but we have found experientially that pulse energies around 50 pJ (and sometimes as high as hundreds of pJ), as typically used in these measurements, are safe. Due to one tragic incident, it is known that an unattenuated 2H beam (around 5 nJ/pulse at the sample position) can destroy the objective, and pulse energies as high as that have since been avoided. The highest pulse energy we have used since is approximately 150 pJ, measured at 820 nm.

For compatibility with the high NA objective, samples must be prepared on #1.5 coverslips (Thermo-Fisher), and mounted on the objective with a drop of immersion oil. The sample is lowered until the objective just makes contact with the immersion oil. Then, the sample-substrate interface is brought into focus. Time-zero, when the pump and probe pulses exactly overlap, varies on a day-to-day basis due to various factors, such as slight differences in the exact path of both beams and the number of ND filters inserted into each path. Thus, time-zero must therefore be calibrated for each measurement by monitoring the differential signal while dialing in the delay time (either via electronic control or delay stage position) until the time of signal onset is found. This task is accomplished by beginning at a positive time delay (1̃0 ps) in order to see signal, then reducing the time delay with coarse (1 ps) steps until the signal disappears, after which the delay is increased by 0.1 or 0.05 ps steps until the time delay at which the signal is at approximately 50% of its maximum intensity is found.

A full stroboSCAT measurement consists of differential measurements at a set of delay times. At each delay time, a configurable number of alternating pump-on and pump-off exposures are taken (typically between 3500 and 7000 1.52 ms exposures), de-interlaced, divided, and averaged to produce a single differential frame. A set of differential frames for all delay times is referred to as a "scan," and typically several scans (from as few as 5 to over 100, depending on the differential signal strength and desired SNR) are taken and averaged together to produce the final measurement. The typical region of interest in a stroboSCAT measurement is 192 px × 192 px, with the position on the 1920 px × 1200 px detector set to place the stroboSCAT signal near the ROI center. This ROI size allows a maximum acquisition rate of around 690 Hz and captures a large enough image to view the stroboSCAT signal and pump reference spot (which is usually placed in the corner furthest from the stroboSCAT peak) with enough distance in between to fully separate them. To remove the pump reference spot, the image is typically cropped after a measurement to the largest size possible in order to simutaneously remove the pump reference and center the stroboSCAT spot, resulting in square image sizes typically 80 - 160 px on each side for analysis and presentation. Last, one scan is always taken with a negative time delay early

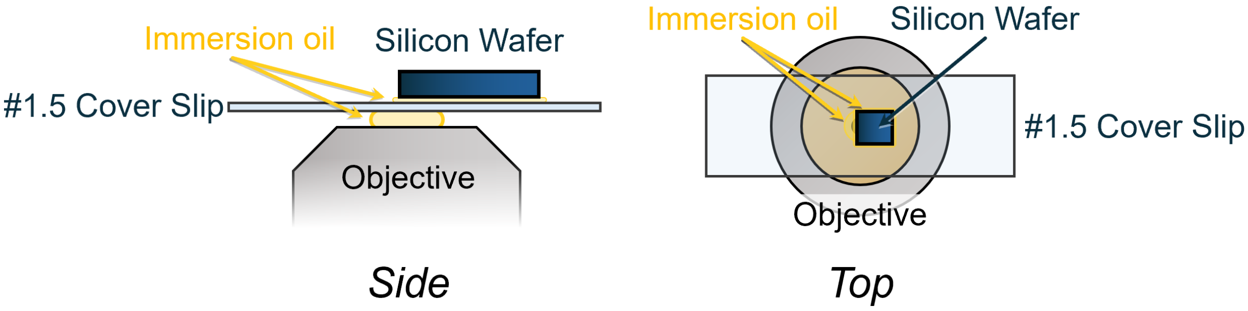

Figure 4.7: Top and side view of "sandwich" sample geometry for silicon measurements.

enough to precede any stroboSCAT signal (e.g., -10 ps, for ultrafast measurements), which is subtracted from all other time points in the dataset. Typically, we aim for a SNR of around 20-50 ((peak signal)/(standard deviation of the noise), the convention used to report SNR hereafter). To generate a dataset of this quality typically takes between 30 minutes to several hours, depending on the stroboSCAT signal strength.

4.3 Ultrafast investigation of energy flow in silicon

Before applying these new ultrafast stroboSCAT capabilities to photosynethic systems, it was necessary to test out the changes on a simpler system. Ideally, such a system would be easy to prepare and well-understood, and it would need to demonstrate some measurable energy carrier migration on picosecond timescales. Crystalline silicon stood out as an ideal candidate. Beyond being one of the most widely-used and characterized semiconductors, silicon had previously been measured with stroboSCAT[59,115] as an early demonstration of the technique's ability to measure both charge carriers and heat. While TIPS pentacene serves as an excellent benchmark for the IRF due to its long-lived signal, silicon's short-lived and rapidly expanding charge carrier signal, present only in the first few hundreds of picoseconds, was an ideal target for benchmarking the new capabilities afforded by the ultrafast laser source.

4.3.1 Sample preparation

P-doped and intrinsic silicon wafers (WaferNet, Inc.) were used in these measurements. The samples were prepared in a "sandwich" configuration, as shown in Fig. 4.7. A small (several millimeters across) piece of the silicon wafer was cut with a diamond scribe, and placed polished-side-down onto a #1.5 coverslip with a thin layer of immersion oil between the two. This configuration ensures that the light exiting the objective travels only through index-matched immersion oil and coverslip glass until it reaches the silicon (as seen from the side view), while allowing repeatable alignment of the sample position thanks to the transparent substrate (as shown in the top view), a major benefit over directly mounting an opaque silicon wafer onto the objective, as was originally done in diode laser measurements.

4.3.2 Spatiotemporal thermometry of silicon - diode laser measurements

Silicon had been shown previously[59] to exhibit a particular signal when probed with diode laser stroboSCAT—specifically, an initially negative (or "dark") signal that rapidly expands and decays gives way to a much longer-lived and slowly expanding positive (or "bright") signal. Fig. 4.8 shows a diode laser stroboSCAT measurement of crystalline p-doped silicon with a 440 nm (2.8 eV) pump that demonstrates this progression most clearly, with the initial dark signal decaying within 1 ns and the subsequent bright signal lasting beyond 5 ns. The initial dark signal was assigned to excited charge carriers (i.e., electrons and holes), which are able to rapidly diffuse through the crystal, owing to silicon's high charge carrier mobility, and also quickly decay due to recombination. The bright signal is attributable then to heat generated by this process, which is much slower to diffuse and dissipate. Repeating this measurement with a 640 nm (1.9 eV) pump supports this assignment. The 440 nm and 640 nm measurements were both performed with a 780 nm probe, with pump fluences of 1.2 J cm^{-2} and 1.5 J cm^{-2}, respectively, in order to match the carrier densities to approximately 10^{20} cm^{-3}. As seen in Fig. 4.8(b), pumping closer to the band gap results in less heat being generated and a fainter bright signal.

We quantify this difference by fitting the peaks at 1 ns (representing the charge carrier signal) and 5 ns (representing the heat signal) to azimuthally symmetric 2D Gaussians, as shown in Fig. 4.8(c) and (d), respectively, and by integrating over the volume under the fit peaks. The results of these fits are shown in Table 4.1.[†] The integrated peak volume should be proportional to the total population of energy carriers present; thus, we take the volume of the 5 ns heat peak (a long enough time delay to ensure no charge carrier signal remains) with the 440 nm pump to that with the 640 nm pump, and we find a value of 1.9(2). It is important to integrate the volume under the peaks when comparing total carrier populations, rather than just comparing the peak value, because initial peak widths differ due to the different diffraction-limited widths of the two pump laser wavelengths, so peak density may be higher due to a narrower peak width while the carrier population generated by the pump laser pulse may be lower. While the pump fluences were selected to approximately match the number of carriers generated, we can see from Table 4.1 that around 15% more signal is present at time 0 in the 640 nm pump measurement. We can account for this differing carrier density by scaling the heat peak volume ratio by this initial charge peak volume ratio, which gives a corrected ratio of 1.6(2). This is within error of the ratio of the pump photon energies, giving a good indication that the bright signal is indeed heat. This treatment assumes that all of

---

[†] Uncertainties are reported in this work in parenthetical notation, where the number in parentheses denotes the uncertainty in the least significant digit displayed, with uncertainties reported as one standard deviation.

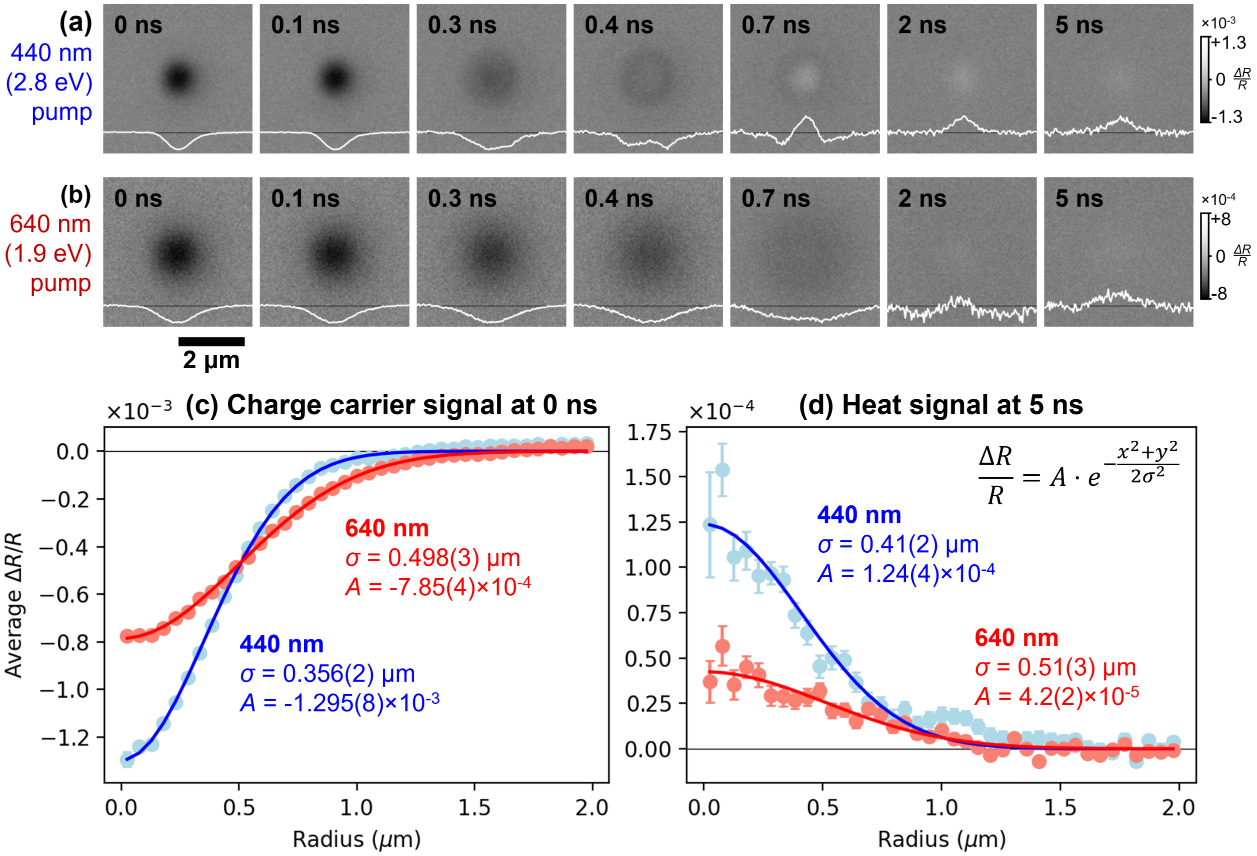

Figure 4.8: Diode laser stroboSCAT measurements (with 780 nm probe) of charge carriers and heat in p-doped silicon. StroboSCAT images with (a) 440 nm (2.8 eV) pump and (b) 640 nm (1.9 eV) pump with normalized center horizontal linecuts overlaid (white curves) demonstrate rapidly expanding and decaying dark signal (charge carriers) giving way to slowly expanding and long-lived bright signal (heat). Azimuthally averaged stroboSCAT data (dots) and Gaussian fits (curves) for signal at (c) 0 ns, showing charge carrier signal, and (d) 5 ns, showing heat signal, for 440 nm pump (blue) and 640 nm pump (red).

the deposited energy is converted into heat, which is a safe assumption given that silicon is an indirect band-gap semiconductor,[116] making radiative recombination unlikely.

Using the absorbance, density, and heat capacity of silicon, we can also convert these heat energies to temperature changes, and find a peak temperature increase of 164 K and 22 K for the 440 nm pump and 640 nm pump, respectively. Given the SNR of approximately 4 for the heat signal at 5 ns in the 640 nm measurement,[‡] temperature increases as low as 10 or below 10 K should be resolvable in silicon with additional averaging and accepting a reduction in SNR to 2, and indeed such temperature differences have been observed via stroboSCAT in

---

[‡] Signal-to-noise ratios are reported in this work as amplitude/amplitude, i.e., (peak of signal)/(standard devation of noise)

	0 ns (charge)		**5 ns (heat)**	
	440 nm	**640 nm**	**440 nm**	**640 nm**
σ (µm)	0.356(2)	0.498(3)	0.41(2)	0.51(3)
A (10^{-4} AU)	-12.95(8)	-7.85(4)	0.124(4)	4.2(2)
Volume (10^{-4} AUµm^2)	-10.32(1)	-12.22(1)	1.31(8)	0.69(6)

Table 4.1: Results of Gaussian peak fits to diode laser stroboSCAT data shown in Fig. 4.8(c) and (d), and resulting calculation of integrated peak volumes.

few-layer MoS_2.[61] In fact, temperature changes as low as 0.1 K have been observed in MoS_2 with diode laser stroboSCAT, which gave a signal near the limit of a $\Delta R/R$ of one pixel count in the 12-bit CMOS well camera (a minimum resolvable change of $1/2^{12}$), setting a lower bound for the detectable temperature change with this method.[110] This spatiotemporally-resolved thermometry is a unique and underexplored strength of stroboSCAT, with many potential applications including in photosynthetic systems, where nonradiative decay pathways play an important role in the photoregulation mechanisms of these systems.

Of similar interest, of course, is the initial signal due to charge carriers. Attempting to quantify the spatial expansion and decay of this signal using stroboSCAT data proved difficult due to its short-lived nature. Within a few hundreds of picoseconds the signal has already decayed, and the expansion occurs so fast that much of the interesting behavior is almost certainly obscured by the IRF. Furthermore, the overlapping and opposing heat signal makes unambiguous quantification difficult. The best strategy in this case has been to fit the heat signal evolution at late times after the charge carrier signal has decayed, then extrapolate back to time-zero to subtract out its effect; however, this requires making assumptions about how the heat signal behaves at early times. As we will see, the ultrafast stroboSCAT configuration provides the solution to these issues.

4.3.3 Ultrafast characterization of charge transport in silicon

Following the ultrafast upgrade to the stroboSCAT microscope, measurement of the early-time charge carrier signal of silicon was selected as a straightforward benchmark measurement to test out the new capabilities and demonstrate the benefits of higher time resolution. Ultrafast stroboSCAT measurements were performed on a polished undoped crystalline silicon wafer with a 540 nm pump and 740 nm probe. The first of these data can be seen in Fig. 4.9(a), with a pump pulse energy of 220 fJ/pulse, corresponding to an approximate carrier density of 1.1×10^{18} cm^{-3}.

Immediately it is notable looking at the longer time delays in Fig. 4.9(a) and comparing to the longer time delays in the diode laser data in Fig. 4.8(a) and (b) that the heat signal is considerably suppressed, if not undetectable. The 540 nm pump is between 440 nm and 640 nm in terms of photon energy, and yet the heat signal present in this measurement is less than in the 640 nm diode laser data. The reason is not immediately obvious; indeed, these

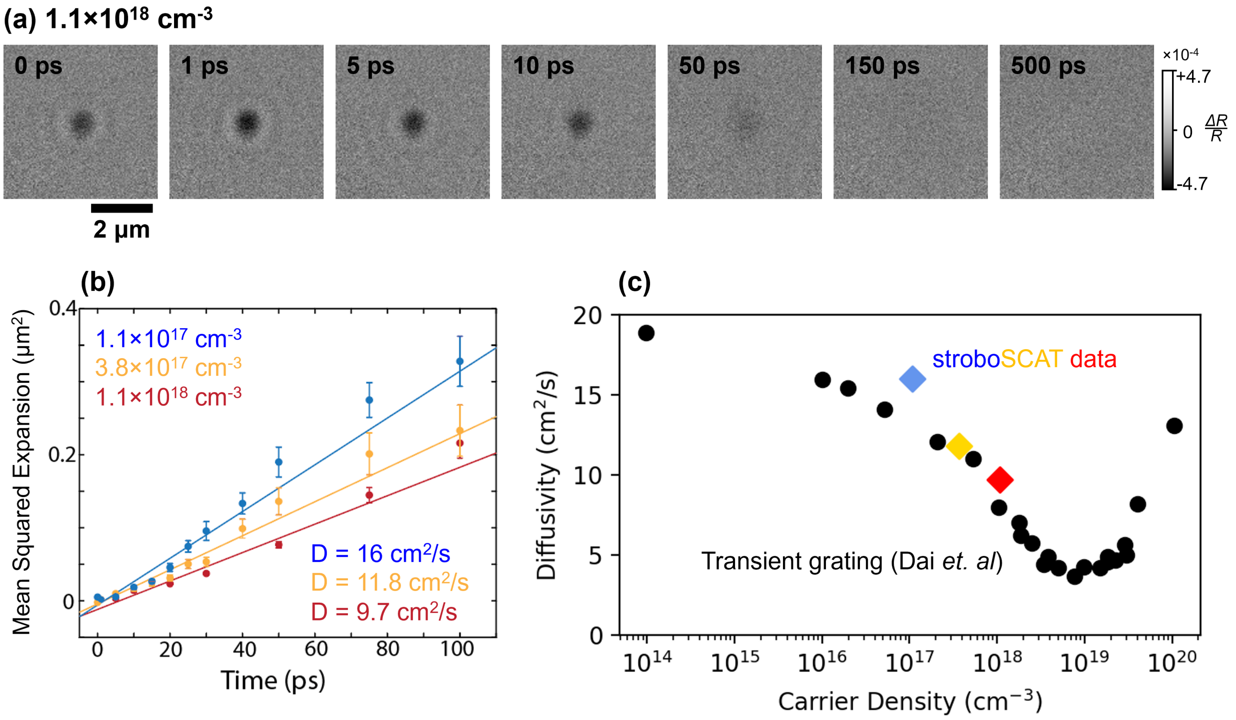

Figure 4.9: Ultrafast stroboSCAT measurement of charge carriers in undoped silicon. (a) stroboSCAT signal in undoped silicon at a carrier density of 1.1×10^{18} cm^{-3}. (b) Mean squared expansion over time from stroboSCAT measurements at three carrier densities, and (c) diffusivity versus carrier concentration, comparing this work (colored diamonds) to previous measurement by Dai *et al.* (black dots).[117]

measurements are operated at a lower fluence by approximately two orders of magnitude, yet the peak charge carrier signal is of the same order of magnitude as that of the diode laser data, and the heat signal ought to be proportional to this signal. To understand this discrepancy one must note the very short lifetime of the charge carrier signal. Whereas we are now able to resolve this decay properly, in the previous measurements the signal was in fact decaying much faster than the diode laser stroboSCAT IRF. When observing this quickly decaying signal with the broad IRF of diode laser stroboSCAT, the temporal averaging results in this short signal being spread out broadly over time, reducing the peak signal much more significantly than the longer-lived heat signal. This principle is demonstrated in Fig. 4.10, which shows the computed signal measured for a hypothetical fast-decaying but high-contrast population (red) and slow-decaying but low contrast population (blue) as the width of the IRF increases. As seen there, the peak intensity of the short-lived component diminishes much more rapidly. Thus the middle case is analogous to this ultrafast measurement, while the bottom case is analogous to the diode laser measurement. With this detail in mind, it's clear that in the ultrafast measurement, we are more truly resolving the charge carrier signal,

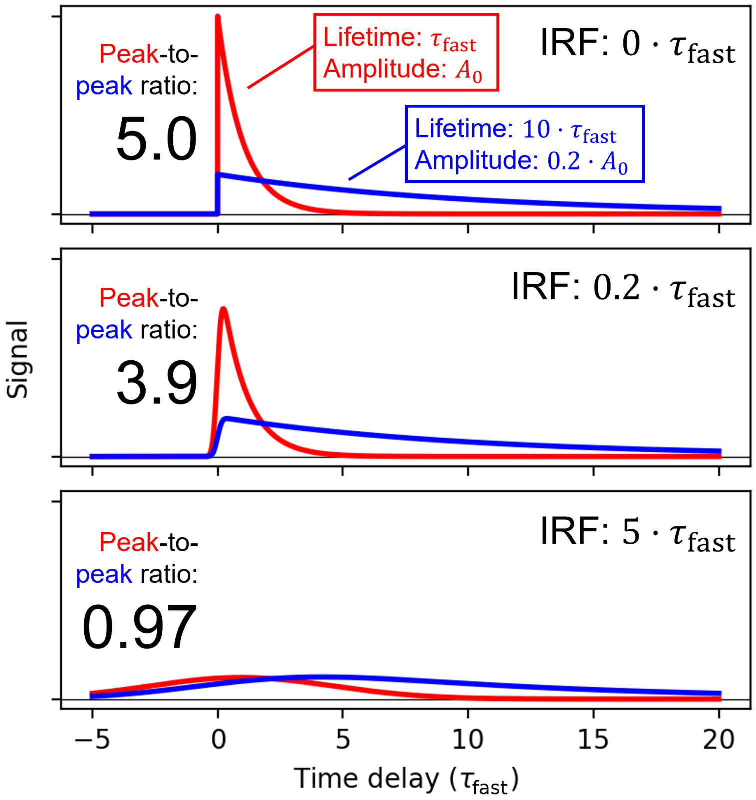

Figure 4.10: Comparison of the relative amplitudes of a short-lived (red) and long-lived (blue) signal as IRF width increases (top to bottom).

which enhances its contrast relative to the heat signal (which we can expect to be around two orders of magnitude weaker than in the diode laser measurement and thus practically undetectable). This highlights an added benefit of the new ultrafast capabilities—namely, the ability to separate short-lived species more effectively from long-lived heat, which has been a challenge in diode laser stroboSCAT when a clear separation of time scales is lacking.[61]

Returning to the charge carrier signal, when we fit the expanding Gaussian population, as shown in the red, we recover a linear mean squared expansion as a function of time, from which we extract a diffusivity of 9.7 cm^2/s. While an impressive figure by most comparisons, this is lower than the reported diffusivity of 39 cm^2/s for electrons in silicon.[118] In fact, the photogenerated population that we observe is not purely electrons, but pairs of electrons and holes that attract one another. This attraction slows the expansion of the carrier populations, leading to a lower overall diffusivity, i.e., the ambipolar diffusivity. The ambipolar diffusivity of such a mixed population is given by the expression:[119]

$$D_a = \frac{D_n D_p (n+p)}{D_n n + D_p p}, \tag{4.10}$$

where D_n and D_p are the electron and hole diffusivities, respectively, and n and p are the photogenerated electron and hole concentrations, respectively. The result of this is an expected ambipolar diffusivity of 19 cm^2/s,[117] which we can consider the intrinsic diffusivity of our electron-hole mixture. This still leaves a large discrepancy that can be explained by carrier-carrier scattering, which in non-negligible at our carrier concentrations. Indeed, as seen in Fig. 4.9(b), stroboSCAT measurements performed at lower carrier concentrations of 3.8×10^{17} (yellow) and 1.1×10^{17} (blue) cm^{-3} demonstrate increasing diffusivity with decreasing carrier concentration, which is plotted (colored diamonds) alongside Dai *et al.*'s transient grating data (black dots),[117] showing good agreement. While this quantity has been measured previously, these previous measurements relied on fitting the transient grating decay to a model to extract the diffusivity, whereas stroboSCAT is capable of directly imaging the population evolving over time. This ability to directly probe carrier populations, which is generally applicable to a broad range of samples, combined with the newly improved time resolution, allows us to access heretofore inaccessible measurements, and paves the way for studying photosynthetic systems with stroboSCAT. It does also confirm that stroboSCAT measures ambipolar diffusivities, which must be taken into account when comparing to other transport measurements, such as field-effect transistor-based or Hall-based bulk probes.[120]

4.3.4 Limitations in resolving early-time expansion due to point spread function

One aspect of note in the mean squared expansion of charge carriers in silicon as shown in Fig. 4.9(c) is the behavior observed in the first 25 ps, where at all three carrier densities the rate of the expansion appears be reduced relative to that observed at longer time delays, giving a concave-up appearance. To further understand the cause of this upward concavity, an additional set of measurements were taken with the same pump and probe energies (540 nm pump, 740 nm probe) but with finer time steps near time-zero. As seen in Fig. 4.11(a), while the same trend of increasing diffusivity with decreasing charge carrier density is demonstrated beginning at 20 ps, prior to that there is a period of time just following excitation when all datasets exhibit an apparent diffusivity of 6.3 cm^2/s.

We find that this effect is the result of the choice of pump and probe wavelengths. Because the pump wavelength is shorter than the probe wavelength, the initial charge carrier population is sub-diffraction limited with respect to the probe, which obscures the expansion at short time delays.[61] This explanation becomes clear upon inspection of the data itself. As shown in Fig. 4.11(b), with deliberately heightened positive contrast, a particular ring-shaped artifact is apparent around the initial spot prior to 20 ps. When azimuthally averaged and plotted, as in Fig. 4.11(c), it becomes clear both that this artifact decays in the first 17.5 ps (blue-to-green dots) and that the signal does not measurably expand until after 20 ps (yellow-to-red dots). This artifact is the same imaging artifact seen when imaging small scatterers with iSCAT - namely, it is caused by the point spread function (PSF) of the microscope. The PSF is the spatial component of the instrument response function that was

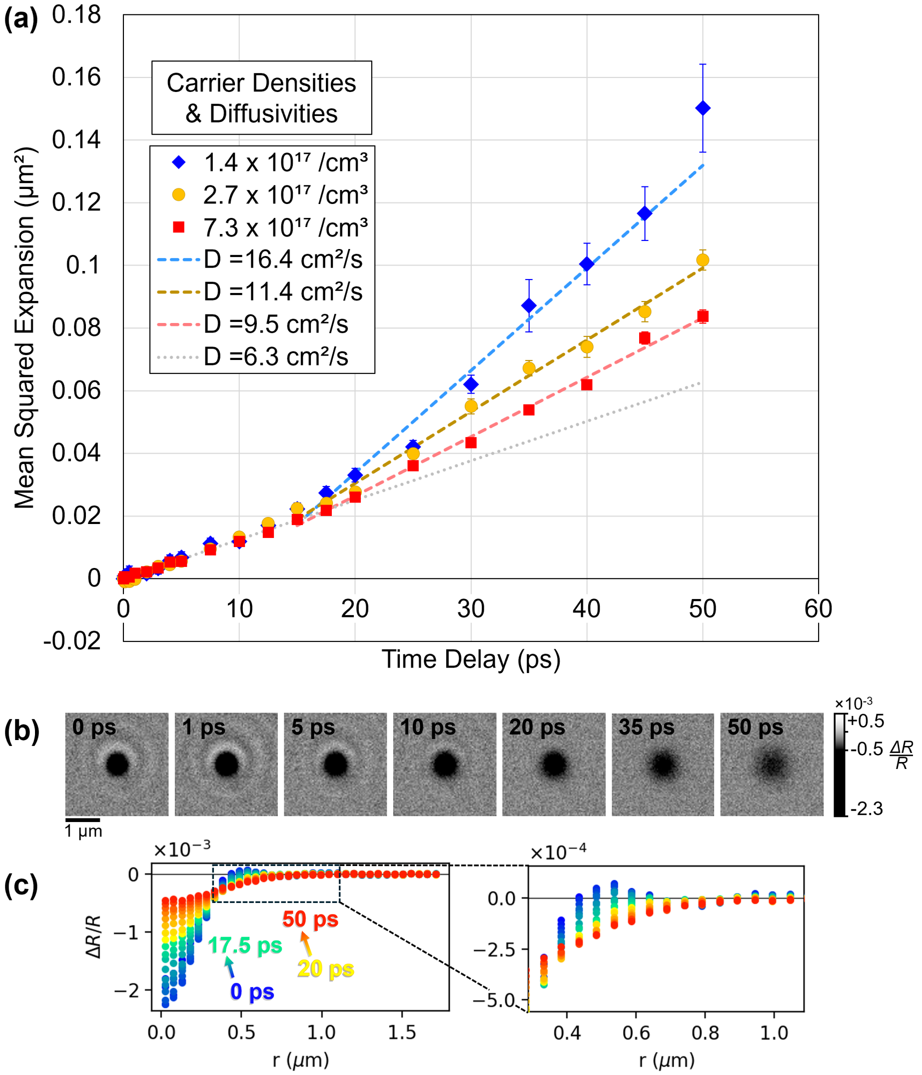

Figure 4.11: Early-time stroboSCAT data on undoped silicon. (a) Mean squared expansion plots over time for three charge carrier densities in silicon (points), and diffusive fits to later-time data (17.5 ps onward, dashed curves), as well as "common" diffusivity fit to short time delays (grey dotted curve). (b) Selected stroboSCAT images from the 7.3×10^{17} cm^{-3} series demonstrating the disappearance of the ring-shaped PSF artifact at 20 ps (contrast heightened for emphasis), and (c) azimuthal averages of same dataset, with two color scales separating "early" and "late" time domains.

discussed in detail in Section 2.1.2. In fact, while the description in Section 2.1.2 focused only on temporal response of the instrument, in full the IRF of the stroboSCAT microscope is a four-dimensional function $IRF(x, y, z, t)$ that describes the signal measured for a stimulus that is perfectly impulsive not only in time but also in x and y (in the focal plane) and z (above and below the focal plane). For the same reasons described previously, knowing this IRF allows us to compute the signal we would expect to measure for any spatiotemporal stimulus by convolving the stimulus with the IRF, as such a stimulus could be "broken apart" into a linear combination of impulsive stimuli, and their responses summed would give the expected signal.

We expect the spatial response of the stroboSCAT microscope to be separable from the temporal response—in other words, the quality of the image does not change as the delay time between the pump and probe is changed (though the population being imaged may). In mathematical terms:

$$IRF(x, y, z, t) = PSF(x, y, z) \cdot IRF_t(t), \tag{4.11}$$

where $IRF_t(t)$ is the temporal instrument response described previously (see Equation 2.8 and accompanying explanation in Section 2.1.2). The PSF is then a spatial function in three dimensions, which for iSCAT has been characterized thoroughly and can be described as the interference of a plane wave and a spherical wave, collected by the circular aperture of the objective and propagated through the transfer function of the $4f$ imaging system via the Richards-Wolf integral.[121,122] The upshot is that at the focus ($z = 0$) the two-dimensional PSF comprises a peak with a set of diffraction rings around it, which is how small scatterers appear in an iSCAT image.

For objects much larger than the diffraction limit, these rings destructively interfere except at sharp edges, which is the key to understanding the cause of this phenomenon. In these measurements the pump is at a considerably shorter wavelength than the probe. The minimum size of the point spread function is limited by the Abbé diffraction limit, the minimum resolvable distance d between two point sources (or equivalently the smallest object that can be resolved):

$$d = \frac{\lambda}{2\mathrm{NA}}, \tag{4.12}$$

where λ is the wavelength of light and NA is the numerical aperture of the objective. By the Helmholtz reciprocity, this is likewise the smallest size to which a beam of light, i.e., the pump, can be focused to by the objective. Putting these together, the 540 nm pump beam is focused by the objective to a spot that is $540/740 = 73\%$ of the diffraction limit of the 740 nm probe. As a result, the initial carrier population is itself sub-diffraction limited, resulting in the ring-shaped artifacts observed in Fig. 4.11(b) and (c). Thus, the initial carrier expansion is not resolvable by the microscope in this configuration, resulting in the apparent low diffusivity before 20 ps, this being the time at which the population has expanded above the size of the 740-nm diffraction limit. And indeed, as can be seen in Fig. 4.11(a), the population with the highest diffusivity (blue) “departs” from the initial diffusive line earlier, around 15 ps, than the population with the lowest diffusivity (red), which does not deviate until at least 20 ps.

One approach to addressing this issue would be to incorporate a full reconvolution analysis into the data utilizing the four dimensional IRF, to recapitulate the artifacts observed at early times and reconstruct the carrier migration underlying it. Recent development of such an analysis workflow for iSCAT imaging of nano-objects has yielded exciting results such as three-dimensional localization of nanoparticles on the surface of a giant unilamellar vesicle,[122] and more work will be required to develop a similar approach for the stroboSCAT analysis workflow. Another option exists, however: to swap the pump and probe sources. By probing at a shorter wavelength than the pump, the initial population will not be sub-diffraction-limited, and the issue is avoided entirely. In recent work, following a laser service visit to restore full wavelength range to the 2H and 3H sources, the ability to swap the 2H and 3H sources was fully operationalized, paving the way for taking this approach. This ability will evidently be invaluable for studying the very early time behavior of systems while retaining the ability to probe red of the pump, as experiments require.

Chapter 5

Quantifying Diffusion and Exciton-Exciton Annihilation in Thylakoid Membranes via stroboSCAT

As has been detailed previously, photosynthesis is a fascinating process that occurs over a wide range of length scales. In the first steps of photosynthesis, a photon is absorbed by a chlorophyll or other pigment molecule, and that energy is transferred to a reaction center containing a special pair of chlorophyll molecules that undergo oxidation,[123] i.e., charge separation, converting the energy from an electronic excitation to a chemical potential. In plants and green algae, this first step of energy transport largely involves two protein complexes. The first is light-harvesting complex II (LHCII), a trimeric protein complex densely packed with light-absorbing chlorophyll *a*, chlorophyll *b*, and carotenoids molecules, which acts as an antenna to absorb light and transport that energy to the second complex, photosystem II (PSII). PSII is a larger protein complex that, in addition to its own chlorophylls and carotenoids, contains the aforementioned reaction center as well as subunits for subsequently performing water splitting and reduction of plastoquinone, which shuttles the chemical potential to the next steps of photosynthesis that ultimately fix the inorganic carbon in CO_2 into bioavailable forms such as starch and sugar. LHCII is also found in the so-called PSII supercomplex,[39] consisting of a PSII core complexed with several LHCII trimers and other minor light harvesting subunits, as well as in discrete units separate from any PSII core but still active in absorbing sunlight and transferring energy towards nearby PSII supercomplexes.[9] These transmembrane proteins, along with others involved in photosynthesis, are embedded in the thylakoid membrane, a structure that separates the aqueous lumen on the interior of the thylakoid from the exterior aqueous stroma within the chloroplast.

Remarkably, in this heterogeneous, room-temperature, constantly changing, and seemingly disordered environment, this energy transfer process can proceed with near unity quantum efficiency in some conditions, with nearly every absorbed photon reaching a reaction center.[2] Furthermore, in high light conditions, a variety of regulatory mechanisms, from quenching of chlorophyll excitations to conformational changes of the thylakoid membrane structure itself, activate to limit this efficiency and protect the cell from oxidative stress.[124] Understanding what factors give rise to this efficiency, and which exact mechanisms are involved in this regulation (and how they might be modified) is therefore of great interest.

Decades of study of photosynthetic systems have uncovered much about about the nano- and meso-scale structure-function relationships that give rise to efficient light harvesting in photosynthesis.[34] Much of the work, however, has focused on measuring energy transfer within individual protein complexes or subunits using novel, often multidimensional spectroscopic techniques, or applying theoretical models[8,125] to structural models of the protein complexes determined from increasingly precise X-ray and cryo-EM characterization.[126–128] Such studies represent remarkable advances in technical capabilities and have built up a detailed understanding of energy transport within and, to an extent, between protein complexes. Spectroscopic studies, whether relying on absorption or, more commonly, fluorescence, are limited by the need for spectral signatures to differentiate exciton migration between different species. While this is somewhat tractable for the various spectrally distinct pigments within the LHCII and PSII complexes, the long-range energy transfer occurring over multiple LHCII complexes has no such spectral signature, and thus remains a relatively under-studied aspect of photosynthetic light harvesting.

With the ultrafast capabilities fully implemented on the stroboSCAT microscope, stroboSCAT measurement of energy transport within natural light harvesting membranes have become possible for the first time. Imaging energy transport in photosynthetic membranes requires picosecond temporal resolution and sub-micron spatial sensitivity, both of which can be attained by the newly configured ultrafast stroboSCAT microscope.[59] With this new capability, we aim to explore outstanding questions about the nature of light-harvesting in photosynthetic membranes. One such question is regarding the role of PSII and the reaction center in the energetic landscape. As excitons migrate through the membrane, to what degree reaction centers attract or trap them is unclear. Unlike bacterial photosynthetic systems, there is no strong downhill energy gradient from LHCII to the reaction center in PSII,[2] and yet the high quantum efficiency of energy transfer indicates that excitations are very successfully transported towards the reaction center. Previous studies of the kinetics of trapping have utilized time-resolved fluorescence,[8,129] which relies on an indirect approach of kinetic modeling to recapitulate fluorescence decays without true spatial resolution. We aim to fill this gap in knowledge to support or refute these models by resolving exciton transport spatiotemporally.

One major open question about the mechanisms that give rise to efficient energy transfer in thylakoid membranes is the role of the reaction center. Compared to the short-range energy funnels in cyanobacteria, in green plants the energy landscape is comparably flat.[35] Efficient energy transfer could be achieved by a rapid, random walk around the chromophore network, or if the reaction centers act as attractive traps for excitons.[34] stroboSCAT will help to study this effect, by directly imaging how exciton migration changes when parameters of the thylakoid membrane are modified. It has been hypothesized that diffusion length is a key parameter governing photosynthetic efficiency in plants[8,57] and stroboSCAT's capability to image diffusion directly will enable further exploration of this hypothesis.

Herein we report the first direct spatiotemporal measurement of excitons in natural thylakoid membranes via stroboSCAT. First, in Section 5.1, we detail the efforts to develop appropriate sample parameters for our apparatus. Then, in Section 5.2, we report the effect of chemical closure of the reaction centers on the observed exciton population behavior and quantify exciton-exciton annihilation occurring in the membrane with a spatiotemporal model. Finally, in Section 5.3 we explore the feasibility of direct measurement of diffusion in these samples with our apparatus and provide recommendations for future stroboSCAT studies on these systems.

5.1 Addressing challenges in preparing biological samples for stroboSCAT microscopy

Beyond increasing the time resolution of the instrument, there were several challenges associated with making stroboSCAT measurements on biological samples that had to be overcome before meaningful results could be acquired. To begin with, there was the question of sample preparation. Until now, stroboSCAT samples had largely consisted of semiconductor materials, often either macroscopic single crystals adhered to a substrate or polycrystalline thin-films deposited directly on a substrate. How to appropriately prepare a biological sample for a stroboSCAT measurement was then a significant open question at the beginning of this work, and much work was done alongside Dr. Stephanie Hart to be able to successfully perform stroboSCAT on these systems.

5.1.1 Developing appropriate thylakoid sample preparation

De-enveloped wild-type spinach (*S. oleracea*) chloroplasts were prepared by Dr. Masa Iwai, in a pH 7.8 1mM Tricine-NaOH buffer solution with 100 mM Sorbitol and 5 mM EDTA. By de-enveloping the chloroplast, the contiguous network of grana stacks and stromal lamellae formed by the thylakoid membrane is exposed, which we refer to simply as the "thylakoid." Samples were flash-frozen in 20 uL aliquots and stored at -80° C, and individual aliquots were thawed and used within 24 hours of thawing. In total, two batches of samples were studied, with the first batch (Batch 1) having a slightly higher chlorophyll (Chl) concentration of 4.11 mg/mL and a slightly higher chlorophyll a to chlorophyll b ratio of 2.87, and the second batch (Batch 2) having a Chl concentration of 3.41 mg/mL and a Chl a/b ratio of 2.67. Chl a/b ratios vary with the season, growth, and line of spinach, but both fall within the expected range.

There are a number of challenges that arise in preparing a biological sample for use in a microscope primarily heretofore used to study metallic and semiconductor materials. For example, most inorganic semiconductors are robust to high pump fluences, whereas photo-bleaching of chromophores is a major consideration in bio-imaging. It is relatively

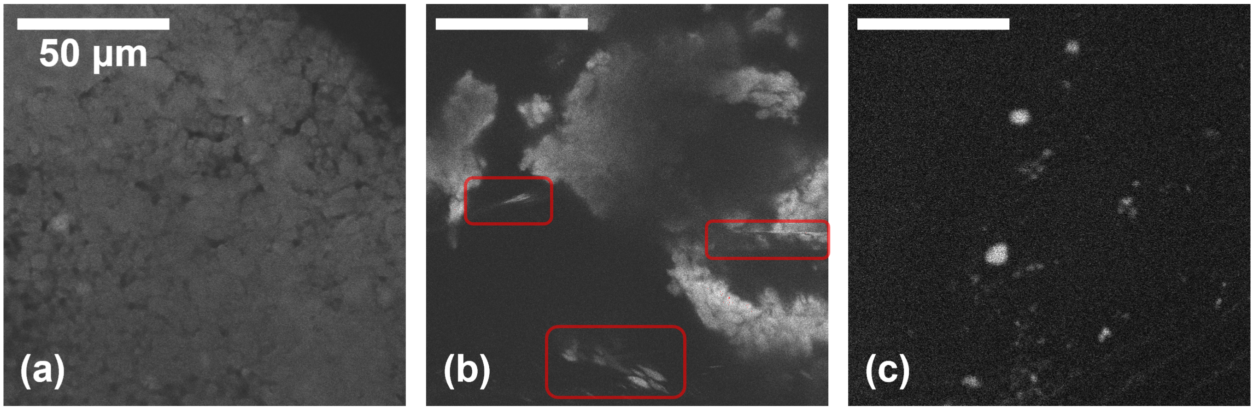

Figure 5.1: Confocal fluorescence microscopy images of thylakoid samples on glass coverslips. Films prepared by dropping (a) full-concentration and (b) 1:10 diluted sample onto substrate and allowing passive deposition, with artifacts from sample motion highlighted with red boxes. (c) Individual e-enveloped chloroplasts deposited via strong adsorption buffer method.

straightforward to imagine an ideal sample preparation for this experiment. The sample would be:

- sparsely distributed, to allow probing of individual de-enveloped chloroplasts,
- immersed in buffer, to emulate biological conditions,
- immobilized on time scales of at least 30 minutes, to allow stable measurements on that time scale, and
- protected against photobleaching.

Regrettably, while it is easy to imagine such an ideal, in reality there are trade-offs that must be contended with. Much of the sample in Batch 1 was used in developing appropriate sample preparation protocol for this measurement in order to best achieve these goals. The initial, naive approach was to simply drop a 5 µL aliquot of sample onto a #1.5 coverslip. These first films were characterized via scanning confocal fluorescence microscopy on an Olympus FLUOVIEW FV4000 microscope with 405 nm excitation. As can be seen in Fig. 5.1(a), this method results in a thick, continuous film of thylakoid membrane, which forms within minutes of drop casting. This thick film is not ideal due to the goal of studying individual thylakoid membrane structures. Diluting the sample 1:10 in buffer before dropcasting results in a non-contiguous film as seen in Fig. 5.1(b), but the structures that form are clearly still aggregates of multiple de-enveloped chloroplasts (which typically are no larger than a few microns across). Furthermore, these structures are not bound to the substrate in any way, and due to Brownian motion and flow (e.g., due to evaporation and convection) in the buffer solution, tend to drift significantly, as evidenced by the smearing artifacts highlighted in red boxes.

The approach for preparing samples that are sparsely distributed yet immobilized is adapted from a method reported by Onoa *et al.*[130] for performing atomic force microscopy on thylakoid membranes. The sample is diluted in a high ionic strength adsorption buffer and then deposited on the substrate and allowed to adsorb for 1 hour. The high ionic strength buffer thermodynamically drives individual de-enveloped chloroplasts to adsorb strongly to the substrate surface. After one hour, rinsing the substrate removes any weakly bound membranes. A confocal fluorescence microscopy image of a sample prepared as such and then re-immersed in buffer is shown in Fig. 5.1(c), where the large aggregates seen previously have been replaced by individual de-enveloped chloroplasts that no longer show the same movement artifacts as in the previous sample preparation protocol.

With the sparsity and immobilization goals largely met, a greater problem loomed: regardless of sample preparation method, thylakoid samples did not initially give any signal when probed with stroboSCAT. Pump and probe wavelengths were tuned to optimize for the sample, with the pump moved to 670 nm to pump resonantly with the chlorophyll a and b peaks, and the probe moved far red to 820 nm to avoid the long tail of the chlorophyll's fluorescence spectrum. In stroboSCAT, fluorescence contaminates the data by introducing a positive differential feature that is not gated and thus appears across all time points. While in some cases such a signal can be subtracted off of all data points, in the limit of low SNR this operation can introduce significant errors. Even so, at these seemingly optimized measurement parameters, no stroboSCAT signal could be observed.

As it turned out, the cause of this absence of signal was photobleaching, which was occurring rapidly upon exposure to the focused pump beam in the presence of oxygen. A simple solution to this issue was to remove the oxygen, which could be done by encapsulation of the sample under nitrogen in a glovebox. Using the glovebox antechamber necessitated the removal of water as well, which unfortunately presents a trade-off between the goal of emulating biological conditions with the goal of preventing photobleaching.

Removing the buffer immersion had an added upside, however, which was to increase the SNR of the measurement. This byproduct was because the refractive index of water (1.33) is much closer to the refractive index of glass (1.5) than of air (1), which significantly reduces the amplitude of the reflected reference field generated at the glass-sample interface. By a simple Fresnel coefficient of reflection calculation, the water-glass interface results in a 30% decrease of the reflected field amplitude compared to a water-glass interface. When the reflected field amplitude is decreased, the detector shot noise (i.e., the noise introduced due to the Poisson statistics of detecting photons in an electromagnetic field) increases relative to the number of photons N detected with a $\sqrt{N}$ dependence.[110,131] The iSCAT contrast, per Eqn. 4.4, is, however, inversely proportional to the reflected field amplitude, which exactly counteracts this square root dependence. Thus, in the optimal case of a shot-noise-limited laser beam (i.e., when all other sources of noise are dominated by shot noise at the detector), reducing the amplitude of the reflected field does not impact the stroboSCAT SNR, but rather trades off contrast for total detected photons.[105,132] In the case of these ultrafast stroboSCAT experiments at 820 nm detection wavelength, we are limited in the total incident photon flux allowable because of the damage threshold of the objective, which causes photon counts to

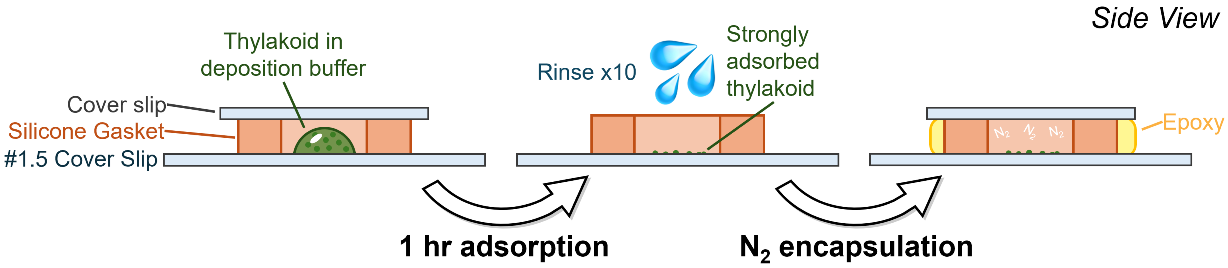

Figure 5.2: Thylakoid sample preparation for stroboSCAT.

fall too low in the case of the glass-water reflection, to the point where dark counts (i.e., thermal noise) become a significant factor, and the measurement is no longer in the shot noise limit. Typical dark counts for our exposure times are around 10-100, and for the glass-water interface signal counts fall below 2000, placing the shot noise level below the noise due to dark counts. Furthermore, as will be discussed in Section 5.3.2, there are a number of additional sources of noise in the experiment that may further contribute to this issue. So, while this dehydration did remove some biological realism from the sample configuration, for the first time it allowed the collection stroboSCAT data on thylakoid membranes, and future improvements to the apparatus will ameliorate this trade-off. In particular, a shift toward detecting at a shorter wavelength around 540 nm would increase the quantum efficiency of the detector by close to four times, in addition to potentially strengthening the stroboSCAT signal response, which would accommodate the lowered reflectivity.

5.1.2 Sample preparation for N_2-encapsulated dehydrated thylakoids for stroboSCAT

The standard sample preparation procedure developed for dehydrated thylakoid samples is as follows. First, a 20 uL aliquot of de-enveloped chloroplast is thawed, and a 1:10 dilution is performed in a high ionic strength aqueous deposition buffer (pH 8.0 10 mM Tris-HCl, 150 mM KCl, 25 mM $MgCl_2$). A clean 22×50 mm^2 #1.5 glass coverslip is prepared by affixing to it a flat, 0.6 mm thick silicone gasket (Grace Bio-Labs, Inc.) with a 4.5 mm inner diameter placed at the center of the coverslip. Then a 3.5 µL droplet of the deposition mixture is dropped onto the coverslip in the center of the silicone gasket, avoiding the edges of the well to prevent wicking. A 22×22 mm^2 coverslip is then placed on top of the silicone gasket and pressed to form a seal, preventing evaporation. This is diagrammed in the left panel of Fig. 5.2. The sample is placed in a dark drawer for 1 hour to allow deposition to occur. Then, the top coverslip is removed, and the sample is washed ten times with 100 µL aliquots of pH 7.8 1 mM Tricine-NaOH buffer and blown completely dry with a gentle stream of nitrogen. The sample is then immediately moved into the antechamber of an N_2 glovebox and put under vacuum for 30 minutes. It is important that the sample is completely dry before placing it in the antechamber, or else remaining water may boil and cause the thylakoids to detach from the coverslip surface. After pumping down for 30 minutes, the sample is moved into the glovebox and encapsulated under N_2 by surrounding the gasket with a UV-cured epoxy, pressing a fresh coverslip on top of the gasket, covering the center with a small piece of black paper (to prevent UV damage to the sample), and exposing the epoxy to ultraviolet light for three minutes. See the rightmost panel of Fig. 5.2 for a diagram of a sample prepared via this method.

As discussed later in Section 5.3.2, a goal of future experiments is to encapsulate the thylakoid samples under N_2 while still hydrated, to increase biological relevance of the measurement. To that end we would recommend modifying the above procedure by use of a N_2 glove bag rather than the glove box. After rinsing the deposition buffer and drying the sample, the sample could be transferred to a glove bag and re-immersed in a droplet of imaging buffer (10 mM pH 8.0 Tris-HCl, 5 mM MgCl2, and 150 mM KCl)[130] that has been degassed by bubbling with N_2 gas. The sample could then be encapsulated under a coverslip following the same procedure as above.

5.2 Direct imaging of excitons in thylakoid membranes

For the first time, we report wide-field stroboSCAT measurements of photoexcitations in natural photosynthetic membranes. We performed initial measurements with a 670 nm pump laser pulse and a 820 nm probe. The data shown below represent an exciting culmination of much effort to refine the sample preparation and measurement protocols, as well as a promising stepping stone toward future spatiotemporal investigation of energy migration in these systems.

We begin in Section 5.2.1 by describing experiments in which we aimed to measure the impact of chemical closure of the reaction centers on exciton migration. We aimed to do so by comparing the migration observed via stroboSCAT of native systems and those dosed with an herbicide to deactivate the reaction centers. We found, however, that the herbicide was not useful for this purpose on the time scales that we probe. In Section 5.2.2 we explore evidence for exciton-exciton annihilation in the stroboSCAT measurements and detail a spatiotemporal model for simultaneously describing annihilation and diffusion in order to extract a realistic exciton diffusivity. We conclude with recommendations to reduce annihilation and to more directly obtain the diffusivity.

5.2.1 Investigating the role of reaction center closure on exciton dynamics

We investigate the effect of chemical closure of the reaction centers on the exciton migration observed via stroboSCAT. 3-(3,4-dichlorophenyl-1,1,-dimethylurea (DCMU) is an herbicide which acts primarily by binding to the secondary quinone receptor of Photosystem II,[133] the protein complex containing the reaction where the exciton is first converted into chemical energy by oxidation of a "special pair" of chlorophyll molecules, resulting in charge separation. This energy is then transported through the electron chain via oxidized plastoquinone molecules to drive the synthesis of ATP and NADPH.[134] By blocking the quinone binding site, DCMU disrupts the electron transport chain, effectively closing the reaction center, as the oxidized chlorophyll special pair in the reaction center is unable to transfer its energy to plastoquinone. This chemical closure has been used extensively to study energy transport in photosynthesis. We attempted to image the effects of reaction center closure on the expansion of excitons in thylakoid membranes by measuring stroboSCAT of spinach thylakoid membranes with and without DCMU exposure.

For this study, dehydrated wild-type thylakoid samples were prepared following the standard sample preparation procedure detailed in Section 5.1.2 to prepare thylakoid membranes with (+) and without (-) DCMU. For the samples dosed with DCMU, however, additional steps were added. A 10 mM DCMU stock solution was prepared by diluting DCMU (Fisher Scientific) in dimethyl sulfoxide (Millipore). In the standard sample preparation procedure, the deposition buffer and the rinsing buffer for the (+) DCMU samples were both brought to a concentration of 10 µL DCMU by serial dilution of the stock solution.

stroboSCAT measurements of thylakoid membranes, some of the first of their kind, can be seen in Fig. 5.3(a). Interestingly, when we fit these data to Gaussian peaks and observe their width over time, we find no effect of DCMU on the expansion of the exciton population. We consider possibilities for why this may be the case. First, we recognize this could be a limitation of the current use of dehydrated thylakoid membranes in this measurement. As explained above, DCMU "closes" the reaction centers by binding to the secondary quinone receptor where plastoquinone leaves after being reduced. In the dehydrated thylakoid, it is ambiguous whether this could occur in any case, regardless of the presence of DCMU. Second, while DCMU closes the reaction center, it does not affect the ability of the chlorophyll network to continue to support energy transfer. As such, the closed reaction center may indeed not have a significant effect on the ability of excitons to freely diffuse, and we may expect no change. On the other hand, in these measurements we resolve only the first 50 picoseconds, due to SNR limitations. On this time scale, we expect only a few hops between chromophores, and the electron transfer processes following charge separation and leading to plastoquinone reduction are much slower. In effect, the initial absorption of the pump laser pulse may effectively close most of the reaction centers in any case. Therefore, we expect that the first 50 ps may be too short to observe the impact of DCMU on energy transfer. For these reasons, as will be discussed, improving the stability of the apparatus to eliminate background artifacts and improve data quality are of great importance.

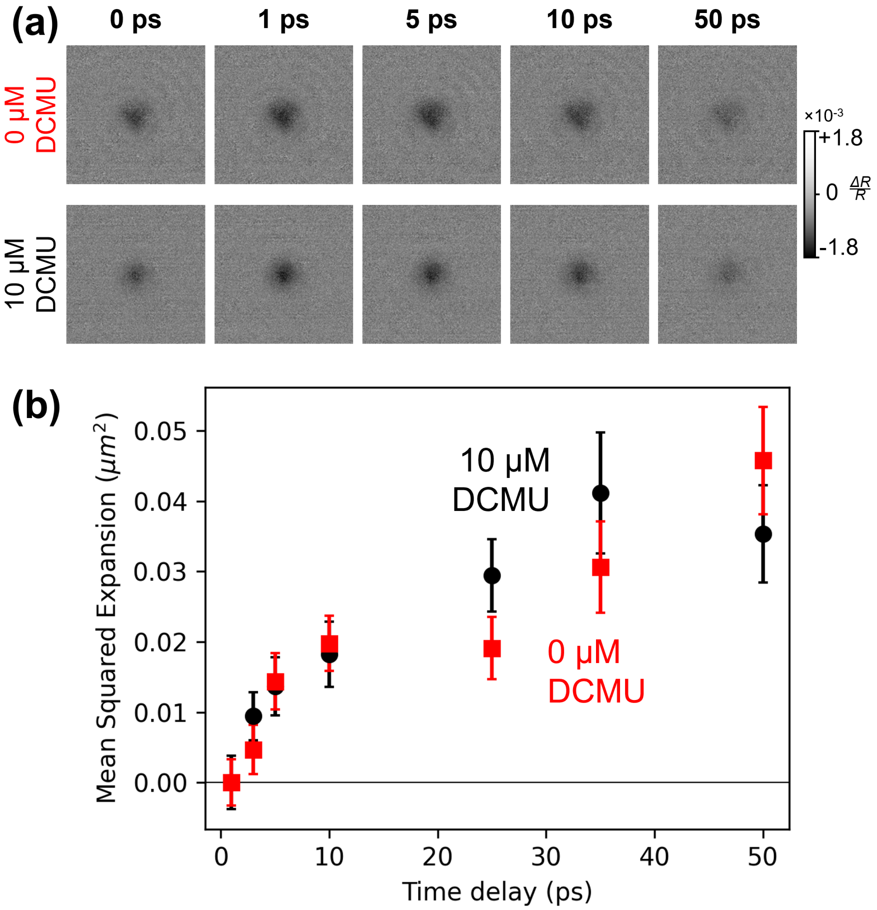

Figure 5.3: StroboSCAT study on thylakoid membranes with and without DCMU. (a) selected stroboSCAT images of excitons in thylakoids with (bottom) and without (top) DCMU, and (b) fits of peak width plotted over time.

5.2.2 Modeling exciton-exciton annihilation in exciton migration stroboSCAT measurements in thylakoids

To better understand the exciton behavior observed via stroboSCAT, a pump fluence series was performed, working with Dr. Siddhartha Sohoni, by measuring stroboSCAT with three different pump fluences: $36\,\mu\mathrm{J/cm^2}$, $17\,\mu\mathrm{J/cm^2}$, and $2.9\,\mu\mathrm{J/cm^2}$, which can be seen in Fig. 5.4(a). When analyzed via the standard (in this context, perhaps naïve) stroboSCAT approach, the thylakoid samples seems to demonstrate remarkably fast diffusion before tapering off around 50 ps. Examining the images in Fig. 5.4(a), however, little if any expansion of the population is apparent. For comparison, refer to Fig. 4.11(b), where the charge carrier population in silicon, with a similar diffusivity, can be seen expanding clearly. Key to understanding this behavior are the mean squared expansions plotted in Fig. 5.4(b) for the

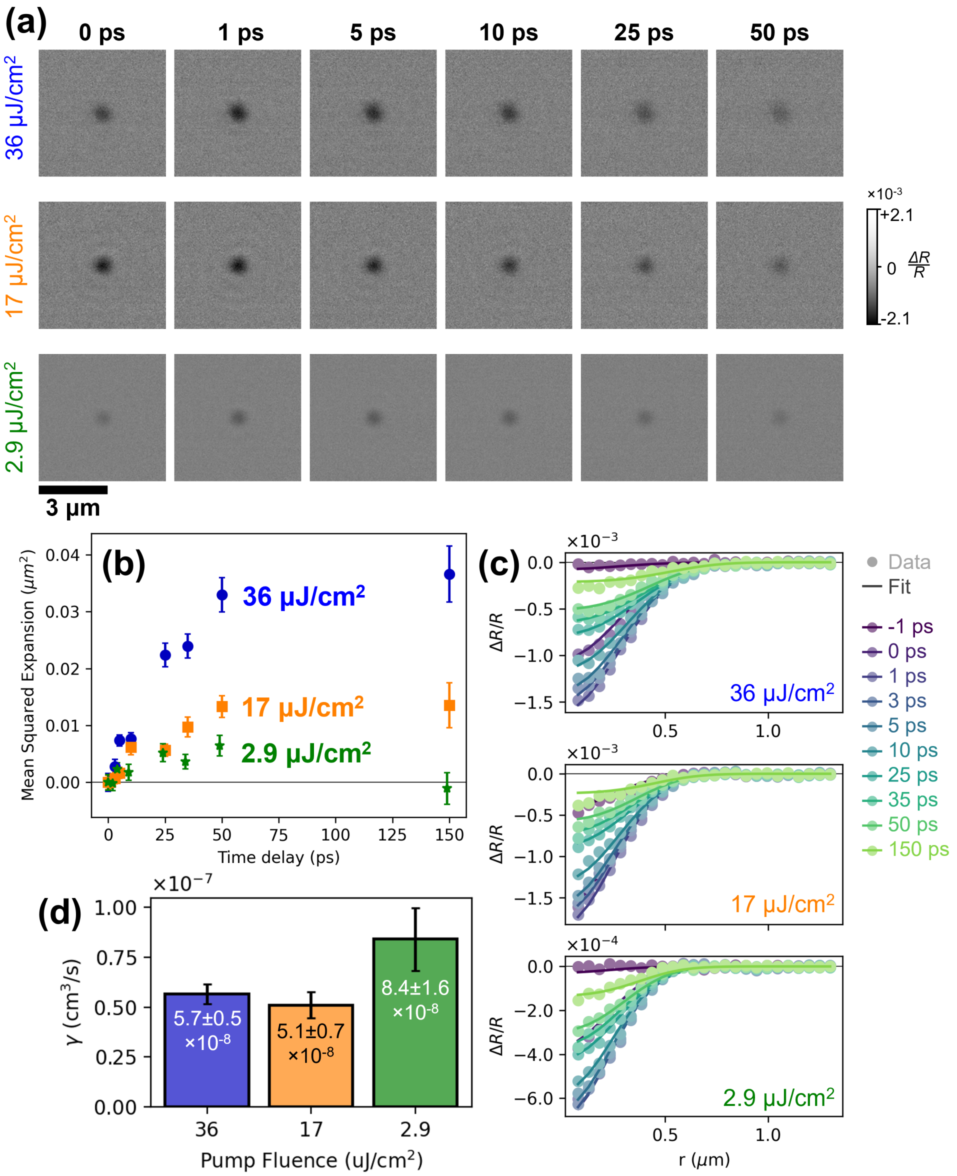

Figure 5.4: stroboSCAT pump fluence series showing annihilation dominating exciton diffusion to varying degrees in thylakoid membranes. (a) stroboSCAT images at the three pump fluences measured. (b) Mean squared expansion versus time for Gaussian fits of the stroboSCAT data. (c) Azimuthally averaged data (circles) plotted atop fitting results of partial differential equation fit (line) for the three fluences measured. (d) Annihilation constants recovered from partial differential equation fits.

three pump fluences measured. As shown, the apparent early time "expansion" decreases as pump fluence increases. This hints that the apparent widening of the peak is not due to diffusion.

Exciton-exciton annihilation (EEA) is a process in which two excitons (in this case, molecular excitations) interact, and one exciton is destroyed, with its energy and momentum transferred to the other. It is analogous to Auger-Meitner recombination in semiconductors, an effect previously modeled and studied via stroboSCAT in two dimensional semiconductors.[61] Because EEA is a bimolecular process, it occurs faster in regions of higher exciton density, i.e, the center of the Gaussian exciton distribution. This density dependent depletion results in the profile flattening over time, leading to apparent expansion when continuing to fit to a Gaussian profile and when continuing to assume strictly diffusive behavior. The net result of this naïve analysis is what is erroneously described as an expanding width when fit as in Fig. 5.4(b). Based on this model, a new model for the analysis of thylakoid stroboSCAT was developed, where rather than treat the signal expansion as purely diffusive, the population density $\rho(r,t)$ at radius r and time t following excitation is evolved over time by solving the partial differential equation that incorporates both diffusion and EEA:

$$\frac{\partial \rho}{\partial t} = D\frac{\partial^2 \rho}{\partial r^2} - \gamma \rho^2. \tag{5.1}$$

In essence, the above equation is the standard diffusion equation $\frac{\partial \rho}{\partial t} = D\frac{\partial^2 \rho}{\partial r^2}$ with diffusivity D with an added EEA term $-\gamma\rho^2$ parameterized by the EEA rate constant γ. To proceed with solving this differential equation, the initial condition is defined as a Gaussian on r, $\rho(r,0) = \rho_0 e^{-r^2/2\sigma_0^2}$, and boundary conditions are set such that $\frac{\partial \rho}{\partial r} = 0$ as $r \to \infty$ and by fixing the flux at $r = 0$ by virtue of the system being treated in cylindrical coordinates. A fine spatiotemporal grid is then defined, with r extending out three times as far as the maximum radius measured (in order to avoid boundary effects), a step size of one fourth the true pixel size, and t extending out to 250 ps in 25 fs steps. The partial differential equation is then solved numerically using MATLAB's `pdepe` PDE solver on this fine grid. Then, the transfer function of the microscope is approximated with a one-dimensional Gaussian temporal IRF of width σ_{IRF} and time zero t_0, and a Gaussian PSF in r with a width σ_{PSF} of 124 nm computed from the diffraction limit of the 820 nm probe and the 1.4 NA objective. The transfer function is applied to the numerical solution by convolution to obtain the signal $S(r,t)$:

$$S(r,t) = \rho(r,t) * IRF(t) * PSF(r). \tag{5.2}$$

Finally, the signal computed on the fine grid is interpolated to the values of r and t matching those collected in the experiment. MATLAB's nonlinear least squares optimizer `lsqnonlin` is then used to iteratively solve the PDE to minimize the residuals of $S(r,t)$ by varying the parameters D, γ, ρ_0, σ_0, σ_{IRF} and t_0. The results of these fits are shown in Table 5.1.

The optimized fits for each fluence are also plotted in Fig. 5.4(c), with quite good agreement between the data and the fits. Of note, in all cases the fits report diffusivities of

Fluence (µJ/cm^2)	D (µm^2/ps)	γ (10^{-8} cm^3/s)	ρ_0 (10^{-4} AU)	σ_0 (µm)	σ_{IRF} (ps)	t_0 (ps)
36	0.0(6)	5.7(5)	18.8(2)	0.242(2)	0.1(1)	0.49(3)
17	0.0(7)	5.1(7)	22.6(4)	0.205(3)	0.55(9)	0.54(2)
2.9	0.0(6)	8(2)	8.7(2)	0.187(3)	0.1(2)	0.57(4)

Table 5.1: Parameters from partial differential equation fits for pump fluence stroboSCAT series.

0 cm^2/s , implying that the apparent "expansion" is in fact entirely due to EEA. As will be explored below, it would still be possible to extract a diffusivity from such measurements with some improvements to the stability of the apparatus and the measurement configuration, but in the current regime, the effect of annihilation dominates the relatively smaller effect of diffusion. Now, in practice the quantity ρ fit in this scheme is not the veritable exciton density, but rather the "true" $\Delta R/R$ signal corresponding to a given exciton density ρ, prior to spatiotemporal averaging caused by the IRF and PSF. The exact exciton density is difficult to determine exactly, but by using the reported[135] chlorophyll concentration in the thylakoid membrane of approximately 240 mM and the peak molar absorption coefficient[136] of chlorophyll *a* of 31441 cm^{-1}M^{-1}, the fluences can be converted to exciton densities, with an approximate conversion factor of 4.9 × 10^{16} cm^{-3}. From this estimate we express the value of γ from the fit in units of cm^3/s, as shown in Fig. 5.4(d), recovering values between 5.1-8.4×10^{-8} cm^3/s.

The exciton-exciton annihilation rate constant in thylakoid membranes has been reported previously to be as low as 2.5×10^{-10} cm^3/s (in isolated LHCII complexes),[137] to 5-15×10^{-9} cm^3/s,[138,139] and as high as 1-1.6×10^{-7}cm^3/s.[140] Our values lie exactly within this range, promisingly indicating that stroboSCAT is capable of accurately measuring this rate in thylakoid membranes. Of course, we have made several assumptions in arriving at this value, particularly in the estimation of charge carrier densities, yet the literature has hardly established a single undisputed value for this rate. stroboSCAT has an added advantage over previous techniques, however, which is its spatial resolution. As shown here, stroboSCAT allows us to distinguish the effects of EEA and diffusion separate from one another, without having to infer from, e.g., a signal's decay, how the excitations are evolving in space and time.

The current set of measurements are, of course, in the EEA-dominated regime and do not spatially resolve the pure diffusion of the excitons. In fact, one common approach to measuring the exciton diffusivity in non-spatially-resolved measurements relies on measuring EEA and inferring the diffusion coefficient from it. This approach makes the assumption that the true EEA rate γ is much faster than the diffusion rate D, such that EEA proceeds as a diffusion-limited reaction. Then, the quantity measured is not in fact γ, but a diffusion-dependent rate $k = 4\pi r_{\mathrm{rxn}} D$,[140,141] where r_{rxn} is the reaction radius, or the distance beneath which any two excitons will undergo annihilation (almost) immediately. Typically r_{rxn} is taken to be the average distance between chlorophyll molecules in the thylakoid. If we make this approximation in our system, using a reaction radius of 1.5 nm (chlorophyll distances vary between 0.5-2 nm across the various proteins in the light harvesting complex) we arrive at diffusion coefficients of 6-9$\times 10^{-2}$ cm^2/s, which is close to previously reported values.[138]

It is exciting to report the first such direct images of excitons in thylakoid membranes, and at the same time there is much still to explore in these systems. The holy grail would be to directly measure exciton diffusion in thylakoid membranes, without relying on secondary reporters such as annihilation, and with these initial measurements made such a measurement is in reach.

5.3 Feasibility study and recommendations for future experiments

We attempt now to lay out a roadmap for future experiments on this system, including a set of simulations to model the feasiblity of directly measuring the diffusion in thylakoid membranes. We find that, while certainly a challenging experiment, we expect the diffusion to be resolvable and quantifiable with our apparatus, and we identify key improvements to the microscope and measurement that will assist in achieving this difficult task.

5.3.1 On the feasibility of resolving diffusivity in thylakoid membranes on small scales

To predict whether or not the stroboSCAT microscope is capable of resolving diffusion in thylakoids as we seek to do, we constructed a set of simulations to model the response of our apparatus to realistic expectations of diffusion in these samples. We use a diffusivity of 7×10^{-2} cm^2/s to match the values extracted from our annihilation model above (6-9$\times 10^{-2}$ cm^2/s) as a starting point.

First, there is the question of whether diffusion on the scale expected is resolvable in our microscope. To answer this question, we construct a simple diffusion simulation. 40,000 "particles" meant to represent excitons are initialized on a 2D plane with an initially Gaussian distribution by sampling 40,000 x and y coordinates from a normal distribution with a width given by the diffraction limit of the 540 nm pump laser pulse, i.e., a full width at half maximum of $\lambda/(2NA)$ with a numerical aperture of 1.4. The particles are then evolved via a Wiener process, i.e., for each time step Δt each particle is offset by normally distributed distances Δx and Δy with a distribution width in each dimension of $\sigma = \sqrt{2D\Delta t}$. Then, this distribution of points can be "imaged" in two steps. First, a 2D histogram of the pixel positions over a 2 µm × 2 µm area is taken and multiplied by a biexponential decay in time with parameters derived from the biexponential fit to the integrated intensity decay of the stroboSCAT data taken at 36 µJ/cm^2, as shown in Fig. 5.5(a). Finally, this histogram is convolved with a Gaussian spatiotemporal instrument response function, with a PSF width

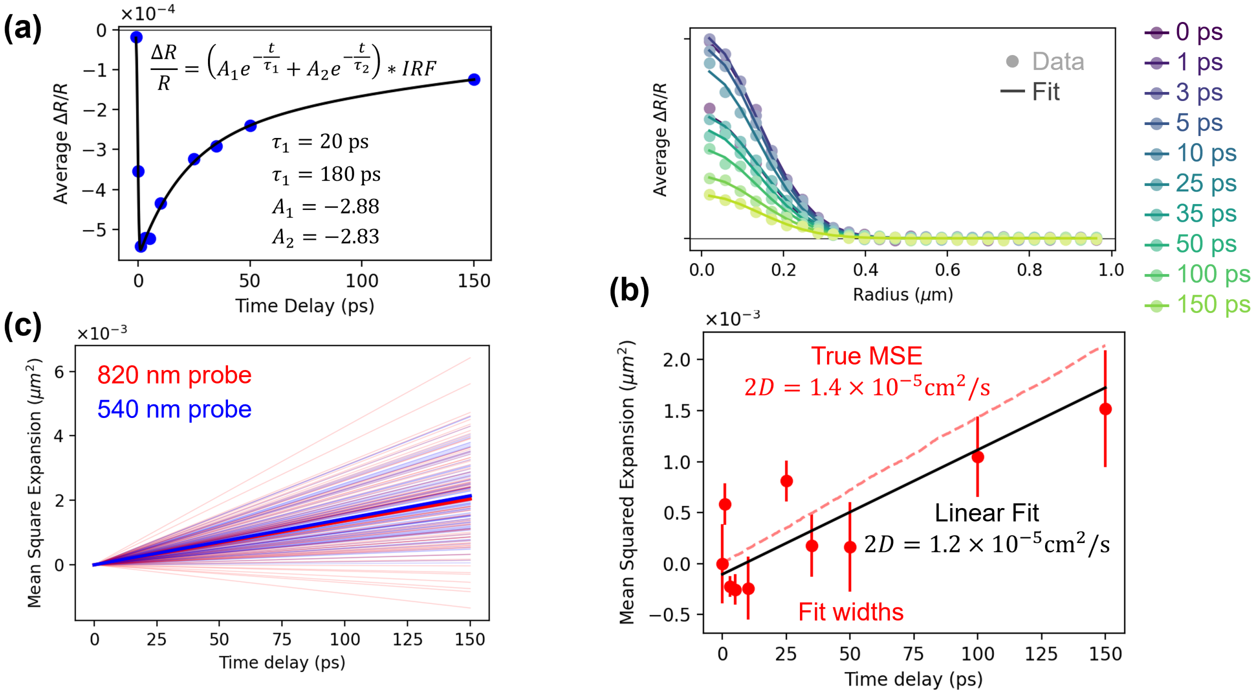

Figure 5.5: Simulated stroboSCAT data based on simple diffusion model. (a) Integrated intensity of the thylakoid stroboSCAT data taken at 36 μJ/cm^2 pump fluence (blue dots) and biexponential reconvolution fit (black curve). (b) Top: Fits (colored curves) to azimuthally averaged simulated data (colored dots) Bottom: Widths of fits above plotted over time for selected time points (red dots, error bars $\pm 1\sigma$ fit error), with linear fit (black curve) compared to actual mean squared expansion extracted from simulated points (light red dashed curve, shown divided by two to normalize out dimensionality). (c) 100× repeated simulation results with 820 nm probe (red translucent curves) and 540 nm probe (blue translucent curves) as well as averages of both sets (red and blue solid curves).

given by the diffraction limit of the probe and a temporal IRF width of 0.7 ps, matching the experimentally measured IRF, likewise obtained from fitting the experimental data. We note that this is a first-order approximation, as the EEA contributes to this decay and likely contributes significantly to the faster, 20 ps decay component. EEA itself has spatial effects (peak flattening) noted above, that are not captured by this model, but it serves as a first approximation. Finally, the histogram is downsampled to a pixel size of 37.2 nm × 37.2 nm to match the camera in the apparatus, and Gaussian noise is added to achieve a specified SNR to match SNRs achieved thus far.

As expected, this results in a 2D Gaussian signal that expands with time, which when azimuthally averaged and fit to a Gaussian expands with the characteristic $\sigma^2(t) = \sigma_0^2(t) + 2Dt$ of diffusion. As shown in Fig. 5.5(b), through this process we are able to measure a diffusivity of 6.0(7)$\times 10^{-2}$ cm^2/s, close to the true diffusivity of 7 $\times 10^{-2}$ cm^2/s though

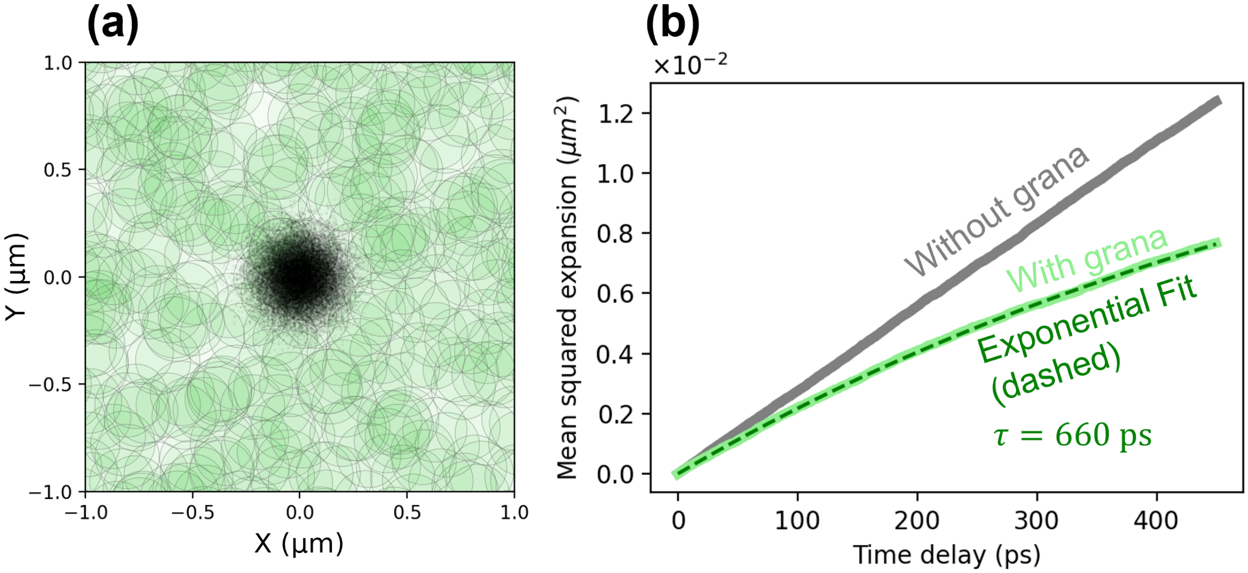

Figure 5.6: Diffusion simulation with circular "grana" domains. (a) Snapshot of simulation, with grana depicted as translucent green circles and diffusing particles depicted as black points. (b) Mean squared expansion from simulation, compared without grana (gray curve) and with grana (light green curve), as well as exponential fit (dashed green curve).

with considerable uncertainty. Part of this uncertainty arises due to the artificial noise introduced in the simulation, and increasing the SNR of the measurement will be important for accurately resolving diffusion, as detailed below. An additional important aspect is the point spread function of the probe. While probing at 820 nm, the initially excited population is sub-diffraction limited, which limits our ability to resolved diffusion in early times, as was explored previously in silicon. If, instead, we probe with a shorter wavelength than the probe, this would no longer be the case and we would expect to be able to fully resolve the diffusion. This is explored by re-doing the simulation with a 540 nm probe, as shown in Fig. 5.5(c), where the fits from individual realizations are shown in translucent curves, with 820 nm (red) and 540 nm (blue) probe wavelengths. While both give an average value of $2D = 1.4 \times 10^{-2}$ cm^2/s as expected, the increased uncertainty is visible in the translucent red curves owing to the lower spatial sensitivity.

Second, there is the question of how the spatial configuration of the thylakoid membrane would affect the expected signal. Thylakoid membranes in green plants are arranged in stacks of disk-shaped structures known as grana (singular: granum) approximately 300 nm across, connected by helical stroma lamellae.[142] As an exciton is unlikely to leave the thylakoid disk that it begins on, there is a question of whether the size of the thylakoid grana would limit the observed expansion by an unresolvable amount. To test this possibility, the simulation is modified by generating a set of "grana" in the form of randomly-distributed circular domains of diameter 300 nm, as depicted in the snapshot of the simulation in Fig. 5.6(a).

Each particle is assigned a granum at the outset by randomly selecting one granum from the set of grana that overlap the particle. Then, during the simulation, the particles are restricted from exiting their grana by rejecting any step that would exit the circular domain and by re-drawing from the normal distribution.

As shown in Fig. 5.6, in comparison to the previous simulation, which demonstrated a linear mean squared expansion in time, the mean squared expansion when diffusing particles are restricted to the granum that they begin on has an exponential decay in time, which is fit to the form $\sigma^2(t) - \sigma^2(0) = \sigma^2_\infty - e^{t/\tau}$ with a time constant τ of 660 ps. Intuitively, this gradual slowing is caused by the finite domain that each particle is permitted to explore. However, as is shown, this effect should only become relevant on timescales of 660 ps or more, and while it does further limit the resolvable diffusion, it does not limit it below our limit of detection. Indeed, the degree to which we observe such a decay may report on how restricted the excitations truly are to their original grana.

5.3.2 Recommendations for future stroboSCAT experiments on thylakoid membranes

A good number of recommendations for future study of thylakoid membranes via stroboSCAT microscopy have become apparent, which we now wish to identify and explore.

The first set of recommendations can be categorized as broad improvements to the stroboSCAT microscope that would be a boon to all measurements performed on the apparatus but would be of particular value to thylakoid measurements, where achieving acceptable SNR is currently possible yet challenging. We note that while the pixel noise is not particularly high after sufficient averaging, the main source of background noise is due to improper background subtraction as a result of shot-to-shot instability in the sample resulting in background artifacts. These artifacts can most clearly be seen in the data in Fig. 5.3(a), with the uneven shape of the stroboSCAT signal caused by incorrect background subtraction. Eliminating this instability will be important for improving data quality.

One such improvement to address this challenge would be to relocate the stroboSCAT microscope stage closer to the laser sources. Currently, the microscope stage is placed far away (a total path length of around 8 meters) from the 2H and 3H NOPAs, as can be seen in the beam diagram in Fig. B.1 in Appendix B. Originally a necessary compromise due to the initial distance of the diode laser-based microscope from the ultrafast laser source, this distance likely contributes to the poor SNR in thylakoid measurements. For one, the long path length includes a large number of mirrors, each of which is susceptible to environmental noise (e.g., vibrations and thermal drift). In addition, a longer path length creates a longer "lever arm," as small changes in the pointing of the beam are amplified over long distances. Together these effects result in noticeable fluctuation of the probe beam spot on the sample and on the camera, which is unideal for background subtraction. Last, even an ideal Gaussian beam can only remain collimated over a distance of twice the Raleigh length, or $2\pi w_0^2/\lambda$, where w_0 is the $1/e^2$ radius at the beam waist and λ is the wavelength of light. In our case,

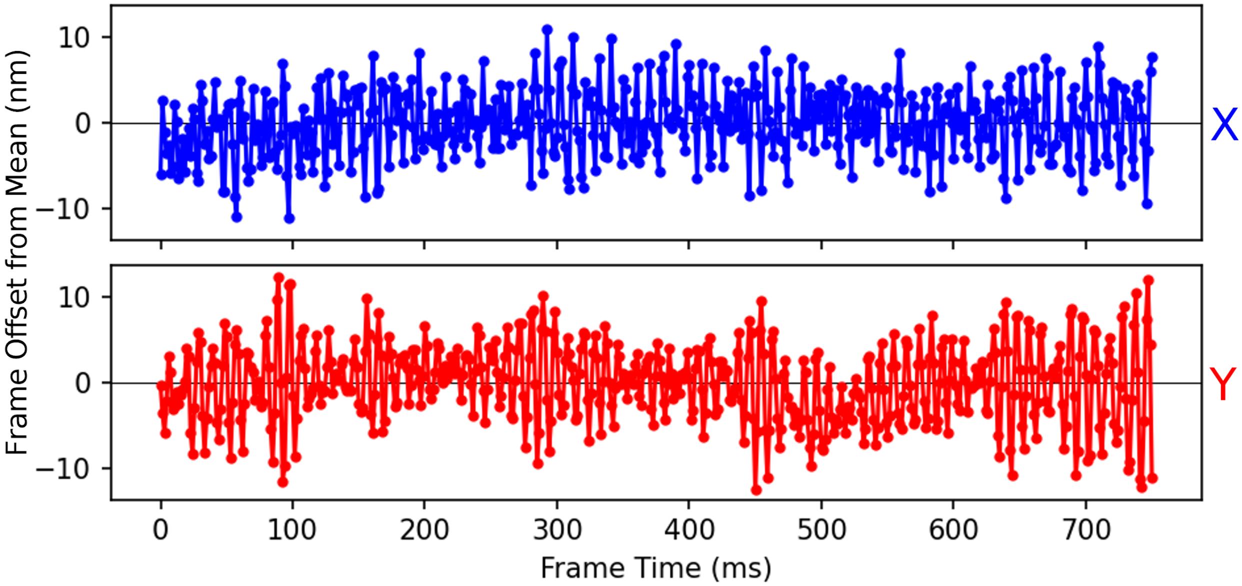

Figure 5.7: Sample vibration in x and y directions extracted from a 500-frame iSCAT movie of a thylakoid sample.

with beam waists around 1-2 mm and wavelengths in the 500-800 nm range, this distance is around 8-40 m, which is on the same order of magnitude as the ∼8-meter path length between laser source and microscope and thus presents difficulty in keeping the beam from diverging on this scale.

To address this problem, we would recommend moving the microscope closer to the laser sources, and a proposed configuration for this setup is shown in Fig. B.2 in Appendix B. This proposed setup would eliminate two mirrors from the probe path and five mirrors from the pump path, and significantly reduce the path length of both paths by approximately 3 ± 1 meters, improving overall stability. Considering that the angular deviation of the beam scales approximately linearly with the distance from the vibrating optic, we expect a roughly linear improvement in beam stability as a result of path shortening. Of note, some excess path length is unavoidable due to the time delay inherent to the different path lengths in the two NOPAs, which causes the 2H pulses to be delayed by approximately 2.3 ns (or 70 cm of path length) relative to the 3H. In fact, this is the reason for the circuitous path taken by the 3H beam when routed to the probe path (i.e., the 3HPr mirrors in Fig. B.2), as the swap must add twice this distance to the 3H path (approximately 140 cm), first to match the added path length in the pump path and again to account for the inherent delay. For this reason, the proposed reconfiguration would allow the arbitrary addition of path length to the pump path by movement of mirrors Pu-M3 and Pu-M4. The new configuration would also maintain the ability to swap between laser sources by use of removable mirrors on kinematic mounts.

In addition to the long path causing instability in the pointing of the probe beam, the sample stage presents issues in high quality imaging of thylakoids, as the sample itself is prone to vibration. This can be seen in Fig. 5.7, where the frame-by-frame displacement was extracted by registering to the first frame every frame of a 500 frame iSCAT movie of a thylakoid membrane, revealing vibrations with a standard deviation in the sample plane of 9.2 nm, or about a quarter of a pixel. These frame-to-frame vibrations create an uneven baseline in the calculation of the differential signal $I_{\text{on}}/I_{\text{off}}$, as the background features are not perfectly overlapping. While this is not an issue when imaging a smooth sample such as silicon, thylakoid membranes have many features that make this vibration issue particularly challenging. The home-built stage used in stroboSCAT is diagrammed in Fig. 4.3. Of note, the sample stage is currently mounted to the z-stage by way of an L-bracket attached to an extension plate bolted onto the edge of the y-stage, which creates a large cantilevered mass that exacerbates sample vibration. Replacing this homebuilt stage with an integrated xyz stage would significantly ameliorate this issue. Currently, the xy-stage is a manual micrometer stage (OptoSigma TSD-1202SHUU), while the z-stage is a piezoelectric micrometer stage (Thorlabs NFL5DP20) typically operated manually by use of a micrometer screw. An integrated xyz stage designed for microscopy would eliminate the large lever arm presented by the current setup. If further stabilization is required, sub-pixel image registration before performing the differential calculation is another option. In this approach, before taking the differential measurement, every image is shifted to overlap the initial image, by subpixel amounts if necessary, removing spurious background subtraction artifacts. We developed an implementation of this strategy in LabVIEW that exists as a toggleable option in the microscope software for future measurements.

The second set of recommendations are for experimental parameters. Perhaps most importantly, we recommend pumping with a longer wavelength than the probe. As shown previously, while we expect diffusion to be resolvable on a sub-nanosecond time scale, the scale of diffusion is expected to be quite small. As demonstrated previously in Section 4.3.4, when probing red of the pump, we are limited in our ability to resolve small early-time diffusion because it is occurring below the diffraction limit of the probe. Thus, by pumping redder than the probe, we can resolve all diffusion that is occurring because the initial pump spot will be larger than the diffraction limit of the probe. The trade-off here is that the initial pump spot will be larger, though this could be minimized by probing as close to the pump as possible. In practice, the only limitation is the need to filter out pump light from the measurement, which would require separating the pump and probe wavelengths by around twice their bandwidths of around 10 nm. After some reconfiguration of the setup and laser tune-up, we have prepared the setup for such future thylakoid measurements, with the ability to pump at 670 nm using the 2H NOPA and probe near 540 with the 3H NOPA. Probing at this wavelength will have an added benefit that the camera's quantum efficiency peaks at 80% at 500 nm and is above 70% at 540 nm, whereas the previous probe wavelength (820 nm) is at under 20%. 540 nm is also closer to the excited state resonances of chlorophyll,[143] which should correspond to a stronger stroboSCAT signal. A higher quantum efficiency and stronger stroboSCAT signal will increase SNR effectively for free.

After improving SNR and reducing background artifacts, measuring hydrated samples must become a priority. Hydrated samples (i.e., strongly adsorbed thylakoids re-immersed in imaging buffer), as discussed previously, present one challenge in terms of sample preparation—how to remove oxygen without removing water—and one in terms of the measurement—the lower SNR caused by reduced reflection at the glass-water interface as compared to glass-air. From a sample preparation perspective, we would recommend a procedure of encapsulating the sample immersed in degassed buffer within a water-free environment such as an N_2 glovebag. With the improvements discussed above, it should be possible to overcome the lower SNR. In case it is not, another option to explore would be to artificially increase the strength of the reflected field, e.g., by sandwiching the sample between the substrate and a reflective material such as silicon to reference, instead, to the stronger reflection of the water-silicon interface.

Last, we recommend taking annihilation-free stroboSCAT measurements of thylakoid membranes. Based on a transient absorption technique recently developed by Malý *et al.*,[144] it is possible to eliminate the effects of higher-order processes from pump-probe measurements by measuring at multiple pump fluences in a specific set of ratios. Applying this technique to stroboSCAT would allow the unambiguous extraction of pure unimolecular processes, such as diffusion and linear decay, in the absence of exciton-exciton annihilation.

Taken together, despite the notable data collected on thylakoid membranes thus far, there are many routes to explore toward improving these measurements. To perform a brief cost-benefit analysis, we believe that taking measurements with a probe laser bluer (540 nm) than the pump laser will afford significant improvement to the data quality with little cost and should be attempted first and foremost. Second, replacing the homebuilt stage with an integrated xyz-stage will require more investment to configure, but the potential gains afforded in preventing sample vibration are great. Relocation of the sample stage has the highest cost, with a significant overhaul of the optical path requiring considerable effort, for relatively lower potential gains. The remaining recommendations, such as measuring hydrated samples and attempting annihilation-free stroboSCAT, contain too many unknowns to analyze their costs and benefits at this stage, but exploring these routes will no doubt yield exciting findings along the way.

Chapter 6

Concluding Remarks

In this work, we have explored photosynthetic light-harvesting through a variety of lenses that allowed us to understand how the underlying structural factors impacted the emergent energy transfer behavior exhibited by these systems. Chapter 1 introduced these systems and the various challenges associated with characterizing them. We ask the central question: what factors of these systems' designs lead to efficient light-harvesting, and we motivate our approaches in the subsequent chapters to answer this question.

Chapter 2 described ultrafast transient absorption and transient absorption anisotropy spectroscopy in theory and practice. TAA spectroscopy proved invaluable for studying energy transfer between spectrally indistinguishable chromophores in our model LHC, but achieving the requisite signal-to-noise ratio proved challenging. We nevertheless successfully implemented a high SNR TAA apparatus by using a balanced photodetector and lock-in amplification, capable of performing single-wavelength TAA spectroscopy measurements suitable to the study of artificial LHCs.

Chapter 3 presented a study of the role of disorder in energy transfer in an artificial LHC consisting of a protein scaffold based on the tobacco mosaic virus coat protein with covalently-attached chromophores. By developing a kinetic Monte Carlo model of the system, we found that though we had eliminated dynamic disorder by the engineering of rigid linker molecules. The measurements and model together also revealed that considerable static disorder in the chromophore orientation, energy, and degree of coupling were key factors presenting barriers to long-range energy transfer in these complexes. We were able to quantify the relative amounts of each type of disorder and their effects on energy transfer and anisotropy decay, and we identified a size-dependent effect suggesting that smaller ring-shaped structures present higher equilibrium exciton diffusivity in the presence of such disorder. We concluded that control over these sources of disorder will be key in the development of efficient artificial light harvesting complexes.

Chapter 4 introduced stroboSCAT, a time-resolved, label-free, widefield microscopic technique for imaging the migration of photogenerated energy carriers. We detailed the implementation of a major improvement in the time resolution of our apparatus by introduction of an ultrafast pulsed laser source, which brought the time resolution of the instrument down from 150 ps to ≤ 1 ps. We used this capability to measure the migration of photogenerated charge carriers in silicon, and characterized a density-dependent charge carrier diffusivity in this material due to carrier-carrier scattering at high densities. Furthermore, we identified an artifact of the instrument that arises when pumping blue of the probe wavelength due to an initially sub-diffraction limited volume. This effect is little discussed in the literature, but as demonstrated in silicon can result in spurious results and thus must be considered carefully.

Chapter 5 presented the first-ever stroboSCAT measurements of exciton migration in natural LHCs in green plants. These measurements were made possible by development of an appropriate sample preparation protocol for stroboSCAT, which, for these early measurements, necessitated encapsulation under nitrogen, and dehydration as an unintended consequence, to remove oxygen which was causing near-instant photobleaching. We recommend to improve this sample preparation in future experiments by encapsulating the samples under nitrogen but without dehydration, to increase the biological relevance of the measurement. Analysis of the stroboSCAT data revealed the measurable dynamics are presently dominated by exciton-exciton annihilation, which we are able to model spatiotemporally using a partial differential equation model that can fit both diffusion and annihilation at the same time. An initial study of the impact of chemical closure of the reaction centers via DCMU revealed no effect on the observed behavior, likely indicating that other methods of controlling reaction center closure will be important in the future. We recommended a number of other improvements to the setup and the measurement parameters to maximize signal-to-noise ratio and to better elucidate subtle effects.

Together, these studies highlight the value in developing high signal-to-noise spectroscopies and microscopies for studying energy transfer in artificial and natural photosynthetic light-harvesting systems. These systems present some of the most challenging light-matter interactions to study, yet the wealth of knowledge provided by hundreds of millions of years of evolution is worth the effort. There is still much to understand in terms of how plants acheive efficient energy transfer, and these large steps in spatiotemporally resolving this process lay the groundwork for exciting future exploration.

Bibliography

(1) Blankenship, R. E. In *Molecular Mechanisms of Photosynthesis*; Blackwell Science Ltd: 2002, pp 61–94.

(2) Blankenship, R. E., *Molecular Mechanisms of Photosynthesis*; Blackwell Science Ltd: 2002.

(3) Li, X.; Hou, W.; Lei, J.; Chen, H.; Wang, Q. *International Journal of Molecular Sciences* **2023**, *24*, Number: 11 Publisher: Multidisciplinary Digital Publishing Institute, 9733.

(4) Hu, X.; Damjanović, A.; Ritz, T.; Schulten, K. *Proceedings of the National Academy of Sciences* **1998**, *95*, Publisher: Proceedings of the National Academy of Sciences, 5935–5941.

(5) Sturgis, J. N.; Niederman, R. A. *Photosynthesis Research* **2008**, *95*, 269–278.

(6) Liu, Z.; Yan, H.; Wang, K.; Kuang, T.; Zhang, J.; Gui, L.; An, X.; Chang, W. *Nature* **2004**, *428*, Publisher: Nature Publishing Group, 287–292.

(7) Schneider, A. R.; Geissler, P. L. *Biophysical Journal* **2013**, *105*, Publisher: Elsevier, 1161–1170.

(8) Amarnath, K.; Bennett, D. I. G.; Schneider, A. R.; Fleming, G. R. *Proceedings of the National Academy of Sciences* **2016**, *113*, Publisher: Proceedings of the National Academy of Sciences, 1156–1161.

(9) Croce, R.; van Amerongen, H. *Journal of Photochemistry and Photobiology B: Biology* **2011**, *104*, 142–153.

(10) Müh, F.; Zouni, A. *Protein Science* **2020**, *29*, 1090–1119.

(11) Kouřil, R.; Oostergetel, G. T.; Boekema, E. J. *Biochimica et Biophysica Acta (BBA) - Bioenergetics* **2011**, *1807*, 368–374.

(12) Tao, M.-J.; Zhang, N.-N.; Wen, P.-Y.; Deng, F.-G.; Ai, Q.; Long, G.-L. *Science Bulletin* **2020**, *65*, 318–328.

(13) Olaya-Castro, A.; Nazir, A.; Fleming, G. R. *Philosophical transactions. Series A, Mathematical, physical, and engineering sciences* **2012**, *370*, 3613–3617.

(14) Caruso, F.; Chin, A. W.; Datta, A.; Huelga, S. F.; Plenio, M. B. *The Journal of Chemical Physics* **2009**, *131*, 105106.

(15) Fassioli, F.; Dinshaw, R.; Arpin, P. C.; Scholes, G. D. *Journal of The Royal Society Interface* **2014**, *11*, Publisher: Royal Society, 20130901.

(16) Förster, T. *Annalen der Physik* **1948**, *437*, 55–75.

(17) Renger, T. *The Journal of Physical Chemistry B* **2021**, *125*, Publisher: American Chemical Society, 6406–6416.

(18) Zhang, W. M.; Meier, T.; Chernyak, V.; Mukamel, S. *The Journal of Chemical Physics* **1998**, *108*, 7763–7774.

(19) Mukai, K.; Abe, S.; Sumi, H. *The Journal of Physical Chemistry B* **1999**, *103*, Publisher: American Chemical Society, 6096–6102.

(20) Dexter, D. L. *The Journal of Chemical Physics* **1953**, *21*, 836–850.

(21) Laible, P. D.; Knox, R. S.; Owens, T. G. *The Journal of Physical Chemistry B* **1998**, *102*, Publisher: American Chemical Society, 1641–1648.

(22) Nagae, H.; Kakitani, T.; Katoh, T.; Mimuro, M. *The Journal of Chemical Physics* **1993**, *98*, 8012–8023.

(23) Jimenez, R.; Dikshit, S. N.; Bradforth, S. E.; Fleming, G. R. *The Journal of Physical Chemistry* **1996**, *100*, 6825–6834.

(24) Ginsberg, N. S.; Tisdale, W. A. *Annual Review of Physical Chemistry* **2020**, *71*, 1–30.

(25) Akselrod, G. M.; Prins, F.; Poulikakos, L. V.; Lee, E. M. Y.; Weidman, M. C.; Mork, A. J.; Willard, A. P.; Bulović, V.; Tisdale, W. A. *Nano Letters* **2014**, *14*, Publisher: American Chemical Society, 3556–3562.

(26) Lee, E. M. Y.; Tisdale, W. A.; Willard, A. P. *The Journal of Physical Chemistry B* **2015**, *119*, Publisher: American Chemical Society, 9501–9509.

(27) Chenu, A.; Scholes, G. D. *Annual Review of Physical Chemistry* **2015**, *66*, Publisher: Annual Reviews, 69–96.

(28) Beljonne, D.; Curutchet, C.; Scholes, G. D.; Silbey, R. J. *The Journal of Physical Chemistry B* **2009**, *113*, Publisher: American Chemical Society, 6583–6599.

(29) Van Niel, C. B. *Archiv für Mikrobiologie* **1932**, *3*, 1–112.

(30) Fleming, G. R.; Grondelle, R. v. *Current Opinion in Structural Biology* **1997**, *7*, 738–748.

(31) Berera, R.; van Grondelle, R.; Kennis, J. T. M. *Photosynthesis Research* **2009**, *101*, 105–118.

(32) Cheng, Y.-C.; Fleming, G. R. *Annual Review of Physical Chemistry* **2009**, *60*, 241–262.

(33) Fleming, G. R.; Schlau-Cohen, G. S.; Amarnath, K.; Zaks, J. *Faraday Discussions* **2012**, *155*, Publisher: The Royal Society of Chemistry, 27–41.

(34) Scholes, G. D.; Fleming, G. R.; Olaya-Castro, A.; van Grondelle, R. *Nature Chemistry* **2011**, *3*, 763–774.

(35) Croce, R.; van Amerongen, H. *Nature Chemical Biology* **2014**, *10*, Publisher: Nature Publishing Group, 492–501.

(36) Fiebig, O. C.; Harris, D.; Wang, D.; Hoffmann, M. P.; Schlau-Cohen, G. S. *Annual Review of Physical Chemistry* **2023**, *74*, Publisher: Annual Reviews, 493–520.

(37) Berman, H. M.; Westbrook, J.; Feng, Z.; Gilliland, G.; Bhat, T. N.; Weissig, H.; Shindyalov, I. N.; Bourne, P. E. *Nucleic Acids Research* **2000**, *28*, 235–242.

(38) Carpenter, E. P.; Beis, K.; Cameron, A. D.; Iwata, S. *Current Opinion in Structural Biology* **2008**, *18*, 581–586.

(39) Caffarri, S.; Kouril, R.; Kereïche, S.; Boekema, E. J.; Croce, R. *The EMBO journal* **2009**, *28*, 3052–3063.

(40) Croce, R.; van Amerongen, H. *Science* **2020**, *369*, Publisher: American Association for the Advancement of Science, eaay2058.

(41) Iwai, M.; Patel-Tupper, D.; Niyogi, K. K. **2024**, Publisher: Annual Reviews, DOI: `10.1146/annurev-arplant-070623-015519`.

(42) Renaud, J.-P.; Chari, A.; Ciferri, C.; Liu, W.-t.; Rémigy, H.-W.; Stark, H.; Wiesmann, C. *Nature Reviews Drug Discovery* **2018**, *17*, Publisher: Nature Publishing Group, 471–492.

(43) Wu, M.; Lander, G. C. *Biophysical Journal* **2020**, *119*, 1281–1289.

(44) Niyogi, K. K.; Grossman, A. R.; Björkman, O. *The Plant Cell* **1998**, *10*, 1121–1134.

(45) Armbruster, U.; Labs, M.; Pribil, M.; Viola, S.; Xu, W.; Scharfenberg, M.; Hertle, A. P.; Rojahn, U.; Jensen, P. E.; Rappaport, F.; Joliot, P.; Dörmann, P.; Wanner, G.; Leister, D. *The Plant Cell* **2013**, *25*, 2661–2678.

(46) Miller, R. A.; Presley, A. D.; Francis, M. B. *Journal of the American Chemical Society* **2007**, *129*, 3104–3109.

(47) Noriega, R.; Finley, D. T.; Haberstroh, J.; Geissler, P. L.; Francis, M. B.; Ginsberg, N. S. *The Journal of Physical Chemistry B* **2015**, *119*, 6963–6973.

(48) Delor, M.; Dai, J.; Roberts, T. D.; Rogers, J. R.; Hamed, S. M.; Neaton, J. B.; Geissler, P. L.; Francis, M. B.; Ginsberg, N. S. *Journal of the American Chemical Society* **2018**, *140*, 6278–6287.

(49) Hamerlynck, L. M.; Bischoff, A. J.; Rogers, J. R.; Roberts, T. D.; Dai, J.; Geissler, P. L.; Francis, M. B.; Ginsberg, N. S. *The Journal of Physical Chemistry B* **2022**, *126*, Publisher: American Chemical Society, 7981–7991.

(50) Bischoff, A. J.; Hamerlynck, L. M.; Li, A. J.; Roberts, T. D.; Ginsberg, N. S.; Francis, M. B. *Journal of the American Chemical Society* **2023**, *145*, Publisher: American Chemical Society, 15827–15837.

(51) Oliver, T. A. A.; Lewis, N. H. C.; Fleming, G. R. *Proceedings of the National Academy of Sciences* **2014**, *111*, Publisher: Proceedings of the National Academy of Sciences, 10061–10066.

(52) Pan, J.; Gelzinis, A.; Chorošajev, V.; Vengris, M.; Senlik, S. S.; Shen, J.-R.; Valkunas, L.; Abramavicius, D.; Ogilvie, J. P. *Physical Chemistry Chemical Physics* **2017**, *19*, Publisher: The Royal Society of Chemistry, 15356–15367.

(53) Dong, H.; Lewis, N. H. C.; Oliver, T. A. A.; Fleming, G. R. *The Journal of Chemical Physics* **2015**, *142*, 174201.

(54) Lewis, N. H. C.; Gruenke, N. L.; Oliver, T. A. A.; Ballottari, M.; Bassi, R.; Fleming, G. R. *The Journal of Physical Chemistry Letters* **2016**, *7*, Publisher: American Chemical Society, 4197–4206.

(55) Massey, S. C.; Ting, P.-C.; Yeh, S.-H.; Dahlberg, P. D.; Sohail, S. H.; Allodi, M. A.; Martin, E. C.; Kais, S.; Hunter, C. N.; Engel, G. S. *The Journal of Physical Chemistry Letters* **2019**, *10*, Publisher: American Chemical Society, 270–277.

(56) Yang, S.-J.; Arsenault, E. A.; Orcutt, K.; Iwai, M.; Yoneda, Y.; Fleming, G. R. *Proceedings of the National Academy of Sciences* **2022**, *119*, Publisher: Proceedings of the National Academy of Sciences, e2208033119.

(57) Bennett, D. I. G.; Fleming, G. R.; Amarnath, K. *Proceedings of the National Academy of Sciences* **2018**, *115*, Publisher: Proceedings of the National Academy of Sciences, E9523–E9531.

(58) Delor, M.; Slavney, A. H.; Wolf, N. R.; Filip, M. R.; Neaton, J. B.; Karunadasa, H. I.; Ginsberg, N. S. *ACS Energy Letters* **2020**, *5*, Publisher: American Chemical Society, 1337–1345.

(59) Delor, M.; Weaver, H. L.; Yu, Q.; Ginsberg, N. S. *Nature Materials* **2020**, *19*, 56–62.

(60) Folie, B. D.; Tan, J. A.; Huang, J.; Sercel, P. C.; Delor, M.; Lai, M.; Lyons, J. L.; Bernstein, N.; Efros, A. L.; Yang, P.; Ginsberg, N. S. *The Journal of Physical Chemistry A* **2020**, *124*, Publisher: American Chemical Society, 1867–1876.

(61) Weaver, H. L.; Went, C. M.; Wong, J.; Jasrasaria, D.; Rabani, E.; Atwater, H. A.; Ginsberg, N. S. *ACS Nano* **2023**, *17*, Publisher: American Chemical Society, 19011–19021.

(62) Guzelturk, B. et al. *ACS Nano* **2020**, *14*, Publisher: American Chemical Society, 4792–4804.

(63) Utterback, J. K.; Sood, A.; Coropceanu, I.; Guzelturk, B.; Talapin, D. V.; Lindenberg, A. M.; Ginsberg, N. S. *Nano Letters* **2021**, *21*, Publisher: American Chemical Society, 3540–3547.

(64) Lakowicz, J. In *Principles of Fluorescence Spectroscopy*, 3rd; Springer: 2006, pp 353–382.

(65) In *Principles of Fluorescence Spectroscopy*, Lakowicz, J. R., Ed.; Springer US: Boston, MA, 2006, pp 383–412.

(66) Bradforth, S. E.; Jimenez, R.; van Mourik, F.; van Grondelle, R.; Fleming, G. R. *The Journal of Physical Chemistry* **1995**, *99*, 16179–16191.

(67) Gaab, K. M.; Bardeen, C. J. *The Journal of Physical Chemistry B* **2004**, *108*, Publisher: American Chemical Society, 4619–4626.

(68) Vogel, S. S.; Nguyen, T. A.; Meer, B. W. v. d.; Blank, P. S. *PLOS ONE* **2012**, *7*, Publisher: Public Library of Science, e49593.

(69) Van Stokkum, I. H. M.; Larsen, D. S.; van Grondelle, R. *Biochimica et Biophysica Acta (BBA) - Bioenergetics* **2004**, *1657*, 82–104.

(70) Wong, C. Y.; Penwell, S. B.; Cotts, B. L.; Noriega, R.; Wu, H.; Ginsberg, N. S. *The Journal of Physical Chemistry C* **2013**, *117*, Publisher: American Chemical Society, 22111–22122.

(71) Folie, B. Extremely Small and Incredibly Fast: Combining Spectroscopy and Microscopy to Reveal Local Excited State Dynamics in Disordered Semiconductors, Ph.D. Thesis, UC Berkeley, 2018.

(72) Proppe, A. H. et al. *Nature Reviews Materials* **2020**, *5*, Number: 11 Publisher: Nature Publishing Group, 828–846.

(73) Schlau-Cohen, G. S. *Interface Focus* **2015**, *5*, 20140088.

(74) Remelli, R.; Varotto, C.; Sandonà, D.; Croce, R.; Bassi, R. *Journal of Biological Chemistry* **1999**, *274*, Publisher: Elsevier, 33510–33521.

(75) Sandonà, D.; Croce, R.; Pagano, A.; Crimi, M.; Bassi, R. *Biochimica et Biophysica Acta (BBA) - Bioenergetics* **1998**, *1365*, 207–214.

(76) Steen, C. J.; Morris, J. M.; Short, A. H.; Niyogi, K. K.; Fleming, G. R. *The Journal of Physical Chemistry B* **2020**, *124*, Publisher: American Chemical Society, 10311–10325.

(77) Sturgis, J. N.; Olsen, J. D.; Robert, B.; Hunter, C. N. *Biochemistry* **1997**, *36*, Publisher: American Chemical Society, 2772–2778.

(78) Hart, S. M.; Chen, W. J.; Banal, J. L.; Bricker, W. P.; Dodin, A.; Markova, L.; Vyborna, Y.; Willard, A. P.; Häner, R.; Bathe, M.; Schlau-Cohen, G. S. *Chem* **2021**, *7*, 752–773.

(79) Kumar, C. V.; Duff, M. R. *Journal of the American Chemical Society* **2009**, *131*, Publisher: American Chemical Society, 16024–16026.

(80) Kundu, S.; Patra, A. *Chemical Reviews* **2017**, *117*, Publisher: American Chemical Society, 712–757.

(81) Song, Q.; Goia, S.; Yang, J.; Hall, S. C. L.; Staniforth, M.; Stavros, V. G.; Perrier, S. *Journal of the American Chemical Society* **2021**, *143*, Publisher: American Chemical Society, 382–389.

(82) Ziessel, R.; Harriman, A. *Chemical Communications* **2010**, *47*, Publisher: The Royal Society of Chemistry, 611–631.

(83) Fassioli, F.; Olaya-Castro, A.; Scheuring, S.; Sturgis, J. N.; Johnson, N. F. *Biophysical Journal* **2009**, *97*, 2464–2473.

(84) Herz, L. M.; Daniel, C.; Silva, C.; Hoeben, F. J. M.; Schenning, A. P. H. J.; Meijer, E. W.; Friend, R. H.; Phillips, R. T. *Physical Review B* **2003**, *68*, 045203.

(85) Kennis, J. T. M.; Streltsov, A. M.; Vulto, S. I. E.; Aartsma, T. J.; Nozawa, T.; Amesz, J. *The Journal of Physical Chemistry B* **1997**, *101*, 7827–7834.

(86) Marcus, A. H.; Diachun, N. A.; Fayer, M. D. *The Journal of Physical Chemistry* **1992**, *96*, Publisher: American Chemical Society, 8930–8937.

(87) Dedeo, M. T.; Duderstadt, K. E.; Berger, J. M.; Francis, M. B. *Nano Letters* **2010**, *10*, Publisher: American Chemical Society, 181–186.

(88) On, C.; Tanyi, E. K.; Harrison, E.; Noginov, M. A. *Optical Materials Express* **2017**, *7*, Publisher: Optical Society of America, 4286–4295.

(89) Burghardt, T. P.; Lyke, J. E.; Ajtai, K. *Biophysical Chemistry* **1996**, *59*, 119–131.

(90) Smith, T. A.; Irwanto, M.; Haines, D. J.; Ghiggino, K. P.; Millar, D. P. *Colloid & Polymer Science* **1998**, *276*, 1032–1037.

(91) Papiz, M. Z.; Prince, S. M.; Howard, T.; Cogdell, R. J.; Isaacs, N. W. *Journal of Molecular Biology* **2003**, *326*, 1523–1538.

(92) Ahn, T.-S.; Wright, N.; Bardeen, C. J. *Chemical Physics Letters* **2007**, *446*, 43–48.

(93) Gillespie, D. T. *Journal of Computational Physics* **1976**, *22*, 403–434.

(94) Gillespie, D. T. *The Journal of Physical Chemistry* **1977**, *81*, Publisher: American Chemical Society, 2340–2361.

(95) Gillespie, D. T. *Annual Review of Physical Chemistry* **2007**, *58*, 35–55.

(96) Casella, G.; Robert, C. P.; Wells, M. T. In *A Festschrift for Herman Rubin*; Institute of Mathematical Statistics: 2004; Vol. 45, pp 342–348.

(97) Penzkofer, A.; Wiedmann, J. *Optics Communications* **1980**, *35*, 81–86.

(98) Scholes, G. D. *Annual Review of Physical Chemistry* **2003**, *54*, 57–87.

(99) In *Principles of Fluorescence Spectroscopy*, Lakowicz, J. R., Ed.; Springer US: Boston, MA, 2006, pp 413–441.

(100) Penwell, S. B.; Ginsberg, L. D. S.; Noriega, R.; Ginsberg, N. S. *Nature Materials* **2017**, *16*, 1136–1141.

(101) Renger, T.; May, V.; Kühn, O. *Physics Reports* **2001**, *343*, 137–254.

(102) Sarovar, M.; Whaley, K. B. **2013**, *15*, Publisher: IOP Publishing, 013030.

(103) Piliarik, M.; Sandoghdar, V. *Nature Communications* **2014**, *5*, Publisher: Nature Publishing Group, 4495.

(104) Taylor, R. W.; Mahmoodabadi, R. G.; Rauschenberger, V.; Giessl, A.; Schambony, A.; Sandoghdar, V. *Nature Photonics* **2019**, *13*, Publisher: Nature Publishing Group, 480–487.

(105) Lindfors, K.; Kalkbrenner, T.; Stoller, P.; Sandoghdar, V. *Physical Review Letters* **2004**, *93*, Publisher: American Physical Society, 037401.

(106) Kashkanova, A. D.; Blessing, M.; Gemeinhardt, A.; Soulat, D.; Sandoghdar, V. *Nature Methods* **2022**, *19*, Publisher: Nature Publishing Group, 586–593.

(107) Cheng, S.-W.; Xu, D.; Su, H.; Baxter, J. M.; Holtzman, L. N.; Watanabe, K.; Taniguchi, T.; Hone, J. C.; Barmak, K.; Delor, M. *Nano Letters* **2023**, *23*, Publisher: American Chemical Society, 9936–9942.

(108) Xu, D.; Mandal, A.; Baxter, J. M.; Cheng, S.-W.; Lee, I.; Su, H.; Liu, S.; Reichman, D. R.; Delor, M. *Nature Communications* **2023**, *14*, Publisher: Nature Publishing Group, 3881.

(109) Tulyagankhodjaev, J. A.; Shih, P.; Yu, J.; Russell, J. C.; Chica, D. G.; Reynoso, M. E.; Su, H.; Stenor, A. C.; Roy, X.; Berkelbach, T. C.; Delor, M. *Science* **2023**, *382*, Publisher: American Association for the Advancement of Science, 438–442.

(110) Weaver, H. On Light Scattering from Photoexcitations: Making Movies of Nanoscale Energy Transport in Emerging Semiconductors, Ph.D. Thesis, UC Berkeley, 2023.

(111) Penwell, S. B.; Ginsberg, L. D. S.; Ginsberg, N. S. *The Journal of Physical Chemistry Letters* **2015**, *6*, Publisher: American Chemical Society, 2767–2772.

(112) Sedrakyan, H.; Sedrakyan, N. In *Algebraic Inequalities*, Sedrakyan, H., Sedrakyan, N., Eds.; Springer International Publishing: Cham, 2018, pp 21–43.

(113) Sharifzadeh, S.; Wong, C. Y.; Wu, H.; Cotts, B. L.; Kronik, L.; Ginsberg, N. S.; Neaton, J. B. *Advanced Functional Materials* **2015**, *25*, 2038–2046.

(114) Wong, C. Y.; Folie, B. D.; Cotts, B. L.; Ginsberg, N. S. *The Journal of Physical Chemistry Letters* **2015**, *6*, Publisher: American Chemical Society, 3155–3162.

(115) Lyu, P.-T.; Li, Q.-Y.; Wu, P.; Sun, C.; Kang, B.; Chen, H.-Y.; Xu, J.-J. *Journal of the American Chemical Society* **2022**, *144*, Publisher: American Chemical Society, 13928–13937.

(116) Collaboration: Authors and Editors of the LB Volumes III/17A-22A-41A1b In *Group IV Elements, IV-IV and III-V Compounds. Part b - Electronic, Transport, Optical and Other Properties*, Madelung, O., Rössler, U., Schulz, M., Eds., Series Title: Landolt-Börnstein - Group III Condensed Matter; Springer-Verlag: Berlin/Heidelberg, 2002; Vol. b, pp 1–6.

(117) Li, C.-M.; Sjodin, T.; Dai, H.-L. *Physical Review B* **1997**, *56*, Publisher: American Physical Society, 15252–15255.

(118) Jacoboni, C.; Canali, C.; Ottaviani, G.; Alberigi Quaranta, A. *Solid-State Electronics* **1977**, *20*, 77–89.

(119) Linnros, J.; Grivickas, V. *Physical Review B* **1994**, *50*, Publisher: American Physical Society, 16943–16955.

(120) Zhang, Y.; Ye, J.; Matsuhashi, Y.; Iwasa, Y. *Nano Letters* **2012**, *12*, Publisher: American Chemical Society, 1136–1140.

(121) Richards, B.; Wolf, E.; Gabor, D. *Proceedings of the Royal Society of London. Series A. Mathematical and Physical Sciences* **1997**, *253*, Publisher: Royal Society, 358–379.

(122) Mahmoodabadi, R. G.; Taylor, R. W.; Kaller, M.; Spindler, S.; Mazaheri, M.; Kasaian, K.; Sandoghdar, V. *Optics Express* **2020**, *28*, Publisher: Optica Publishing Group, 25969–25988.

(123) Narzi, D.; Bovi, D.; De Gaetano, P.; Guidoni, L. *Journal of the American Chemical Society* **2016**, *138*, Publisher: American Chemical Society, 257–264.

(124) Müller, P.; Li, X.-P.; Niyogi, K. K. *Plant Physiology* **2001**, *125*, 1558–1566.

(125) Novoderezhkin, V.; Marin, A.; Grondelle, R. v. *Physical Chemistry Chemical Physics* **2011**, *13*, Publisher: Royal Society of Chemistry, 17093–17103.

(126) Umena, Y.; Kawakami, K.; Shen, J.-R.; Kamiya, N. *Nature* **2011**, *473*, Publisher: Nature Publishing Group, 55–60.

(127) Van Bezouwen, L. S.; Caffarri, S.; Kale, R. S.; Kouřil, R.; Thunnissen, A.-M. W. H.; Oostergetel, G. T.; Boekema, E. J. *Nature Plants* **2017**, *3*, Publisher: Nature Publishing Group, 1–11.

(128) Standfuss, J.; Terwisscha van Scheltinga, A. C.; Lamborghini, M.; Kühlbrandt, W. *The EMBO Journal* **2005**, *24*, Num Pages: 928 Publisher: John Wiley & Sons, Ltd, 919–928.

(129) Schatz, G. H.; Brock, H.; Holzwarth, A. R. *Biophysical Journal* **1988**, *54*, 397–405.

(130) Onoa, B.; Fukuda, S.; Iwai, M.; Bustamante, C.; Niyogi, K. K. *Biophysical Journal* **2020**, *118*, 1876–1886.

(131) Bunch, R. M. In *Optical Systems Design Detection Essentials: Radiometry, photometry, colorimetry, noise, and measurements*; IOP Publishing: 2021.

(132) Cole, D.; Young, G.; Weigel, A.; Sebesta, A.; Kukura, P. *ACS Photonics* **2017**, *4*, Publisher: American Chemical Society, 211–216.

(133) Hsu, B.-D.; Lee, J.-Y.; Pan, R.-L. *Biochemical and Biophysical Research Communications* **1986**, *141*, 682–688.

(134) Rochaix, J.-D. *Biochimica et Biophysica Acta (BBA) - Bioenergetics* **2011**, *1807*, 375–383.

(135) Lawlor, D. W. In *Photosynthesis: molecular, physiological, and environmental processes*, 2nd; Longman Scientific & Technical: 1993, p 54.

(136) Taniguchi, M.; Lindsey, J. S. *Photochemistry and Photobiology* **2018**, *94*, 290–327.

(137) Bittner, T.; Irrgang, K.-D.; Renger, G.; Wasielewski, M. R. *The Journal of Physical Chemistry* **1994**, *98*, Publisher: American Chemical Society, 11821–11826.

(138) Swenberg, C. E.; Geacintov, N. E.; Breton, J. *Photochemistry and Photobiology* **1978**, *28*, 999–1006.

(139) Geacintov, N. E.; Breton, J.; Swenberg, C. E.; Paillotin, G. *Photochemistry and Photobiology* **1977**, *26*, 629–638.

(140) Lee, T.-Y.; Lam, L.; Patel-Tupper, D.; Roy, P. P.; Ma, S. A.; Lucas-DeMott, A.; Karavolias, N. G.; Niyogi, K. K.; Fleming, G. R. Chlorophyll to Zeaxanthin Energy Transfer in Non-Photochemical Quenching: An Exciton Annihilation-free Transient Absorption Study, Pages: 2023.10.11.561813 Section: New Results, 2023.

(141) Barzda, V.; Gulbinas, V.; Kananavicius, R.; Cervinskas, V.; Amerongen, H. v.; Grondelle, R. v.; Valkunas, L. *Biophysical Journal* **2001**, *80*, Publisher: Elsevier, 2409–2421.

(142) Bussi, Y.; Shimoni, E.; Weiner, A.; Kapon, R.; Charuvi, D.; Nevo, R.; Efrati, E.; Reich, Z. *Proceedings of the National Academy of Sciences* **2019**, *116*, Publisher: Proceedings of the National Academy of Sciences, 22366–22375.

(143) Zamzam, N.; Rakowski, R.; Kaucikas, M.; Dorlhiac, G.; Viola, S.; Nürnberg, D. J.; Fantuzzi, A.; Rutherford, A. W.; van Thor, J. J. *Proceedings of the National Academy of Sciences* **2020**, *117*, Publisher: Proceedings of the National Academy of Sciences, 23158–23164.

(144) Malý, P.; Lüttig, J.; Rose, P. A.; Turkin, A.; Lambert, C.; Krich, J. J.; Brixner, T. *Nature* **2023**, *616*, Publisher: Nature Publishing Group, 280–287.

Appendix A

Practical guide to alignment and taking measurements on TAA apparatus

A detailed diagram of the high-SNR TAA apparatus is shown in Fig. A.1. We now describe the alignment and operation procedures for this apparatus in as much practical detail as possible. Except when noted otherwise, we refer to directions in the following frame of reference: z-axis in the direction of beam propagation, x-axis parallel to the table surface, and y-axis normal to the table surface.

A.1 Probe path alignment

Alignment of the probe path should be undertaken first. Typically, experiment duration is limited by the stability of the pump beam due to the tendency of the output power and beam quality of the homebuilt NOPA to remain stable only on the order of an hour or two. The probe path is generally stable on longer time scales, so alignment of the probe path first usually affords a longer time to collect data. Before proceeding, it is important to ensure all beam blocks are in place, and in particular a block should be placed directly before the CaF_2 white light generation (WLG) crystal (R-WLG) to avoid burning this optic.

Up until the neutral density (ND) wheel (R-ND), the optical path of the probe beam simply meanders back and forth in order to match the path lengths of the two beams. So, alignment of this path is not as critical as the portion closer to the sample. As such, alignment simply proceeds with R-M1 up through R-M12 by aligning each mirror to the next iris position marked in the figure (red dots), with the exceptions of R-M3, R-M5, and R-M7, which are placed so close before the next mirrors in the path that they may be left as-is. R-M13 and R-M14 are then aligned to the two irises following the retroreflector (R-RR). Astigmatism in the 800 nm fundamental beam is not unusual, and may result in elongation of the beam into an elliptical shape by the time the beam reaches R-M15. This could be

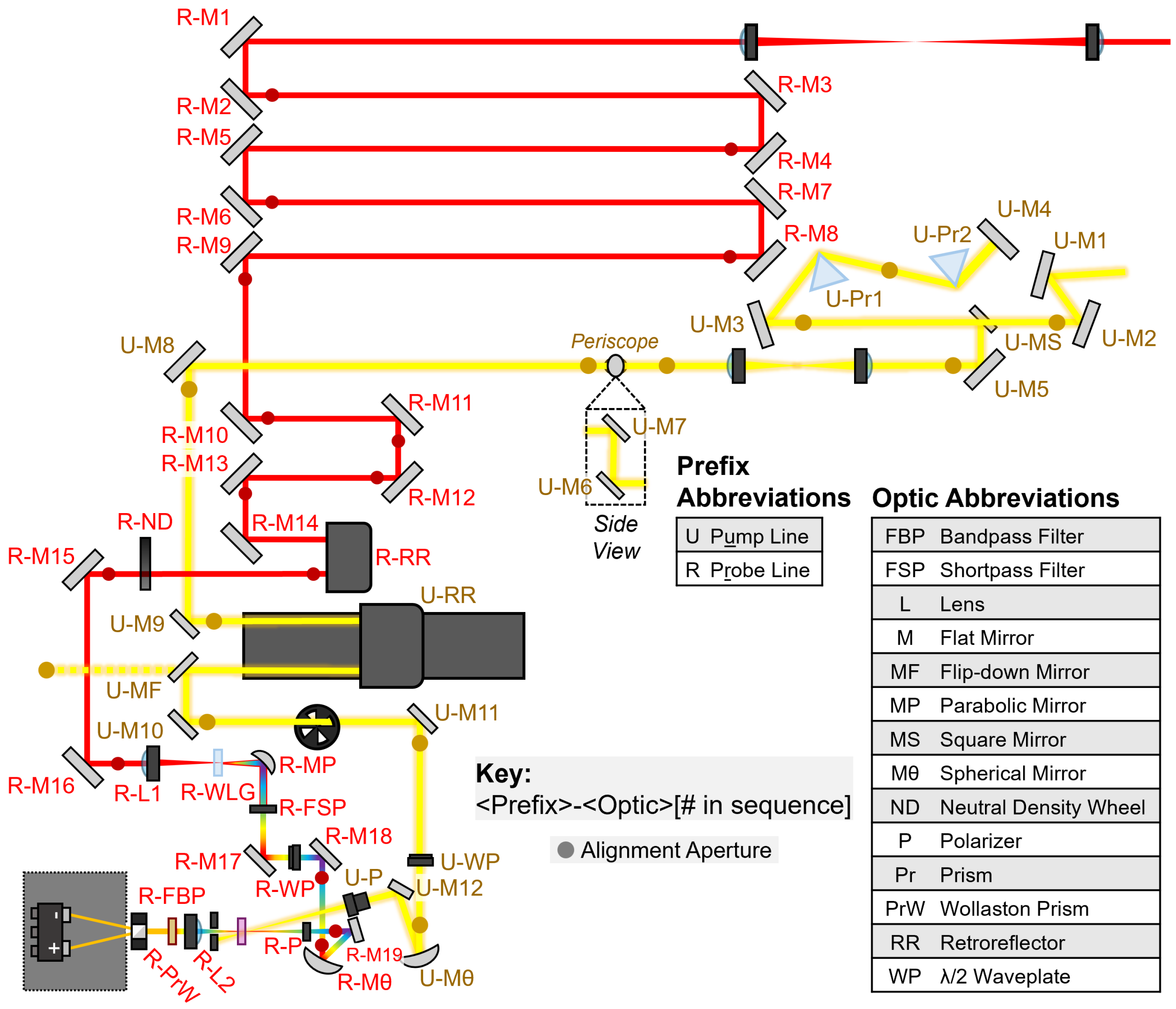

Prefix Abbreviations

U	Pump Line
R	Probe Line

Optic Abbreviations

FBP	Bandpass Filter
FSP	Shortpass Filter
L	Lens
M	Flat Mirror
MF	Flip-down Mirror
MP	Parabolic Mirror
MS	Square Mirror
Mθ	Spherical Mirror
ND	Neutral Density Wheel
P	Polarizer
Pr	Prism
PrW	Wollaston Prism
RR	Retroreflector
WP	λ/2 Waveplate

Figure A.1: Optics diagram of high signal-to-noise ratio transient absorption anisotropy apparatus. All mirrors shown are protected silver. All mounted transmissive optics have a circular aperture diameter of 25 mm, with the exceptions of R-P (12.5 mm diameter), U-P and R-PrW, which have 10 mm × 10 mm square apertures, and R-ND which is a 100 mm diameter wheel.

corrected by addition of cylindrical lenses into the beam path, but such a fix has not as of yet been necessary to achieve high-quality data.

R-M15 should then be aligned to the iris immediately before the WLG focusing lens (R-L1). To aid in this it is useful to reduce the ND wheel to minimum attenuation, but it is important to ensure a beam block is placed before R-WLG before allowing the full beam power through. The microcontroller that controls the translation mount of R-WLG should now be powered on by turning on the connected 5V DC power supply to proceed with alignment of the WLG stage. This will begin rastering the CaF_2 crystal back and forth laterally, to prevent burning by the high intensity focused 800 nm beam. The key to achieving stable white light is to find the correct combination of neutral density (that purely controls the power) and the size of the iris before R-L1 (that controls both power and beam mode) to the point just above the threshold of stable WLG. To begin, with the input beam blocked, it is best to clamp down the input iris to just small enough to give the beam a circular shape. Then the ND wheel can be set to maximum attenuation and the beam unblocked. At this point, input power will be too low for WLG to occur; the attenuation can then be gradually decreased via the ND wheel up until the point that WLG is observed. Then, iterative adjustment of the ND wheel and the input iris allow optimization of the white light quality. Generally, the power should be high enough to avoid unstable output, but not so high as to produce heterogeneous output (such as a bright spot in the center) or excessive 400 nm second harmonic generation. A spectrometer may be placed in the path to monitor the quality of the white light spectrum, with an ideal spectrum demonstrating no wavelength-dependent fluctuations (i.e., the spectrum may fluctuate in total intensity, but the shape of the spectrum is constant over time).

Following WLG, the white light probe beam is collimated by an off-axis parabolic mirror (R-MP), and can then be aligned to the two irises following R-M18 with R-M17 and R-M18. Finally, the probe beam is aligned through the sample (magenta rectangle) by aligning the spherical focusing mirror and R-M19 through the removable iris directly after R-M19 and the iris immediately before R-L2. With the probe path aligned, it is best to block the beam before the WLG stage to protect the CaF_2 crystal from burning while aligning the pump path.

A.2 Pump path alignment

The pump path alignment proceeds through three stages: the compressor, the delay stage, and the sample. First, the pump pulses are compressed in time by use of a dual prism compressor, which adds negative group delay dispersion to compensate for dispersive optics stretching the pulses along the beam path. The beam is aligned through the two irises following U-M2 using U-M1 and U-M2. U-M3 is then aligned to pass the beam through tip of the first prism (U-Pr1), which should also pass it through the center of the iris between the two prisms (if it does not, the iris should be moved). U-M4 then reflects the beam back through the prisms and is aligned horizontally onto the same center iris with a small downward vertical offset. Due to this offset, the outgoing beam is picked off by the square mirror (U-MS), which along with U-M5 can be used to align through the two irises around the telescope. Following the telescope, the periscope translates the beam up into sample plane, and can be aligned by use of U-M6 and U-M7 to the following two irises. U-M8 is then aligned to the iris immediately before the delay stage.

Alignment of the delay stage can be counterintuitive. The key to understanding this process is understanding that any beam incident on the retroreflector (U-RR), which is composed of three mirrors meeting at right angles, *always* emerges parallel to the incoming beam, regardless of the direction of the incoming beam. Thus, when the retroreflector moves on the delay stage, the outgoing beam is guaranteed to not change direction (i.e., pitch or yaw). However, if the incoming beam is not parallel to the direction of the delay stage's translation, then the incoming beam will strike the retroreflector at a different position depending on the delay stage's position, resulting in a translation of the outgoing beam. To align U-M9 into the delay stage, the flip mirror U-MF is flipped down, allowing the beam to propagate to the far iris behind it (path indicated by dashed yellow line). Then, starting with U-RR all the way forward, U-RR is moved all the way back, noting the magnitude and direction of any movement by the laser spot on the far iris. Such motion indicates that the incoming beam is not parallel to the axis of movement. To correct a deviation in x, U-RR is brought all the way forward again and a small change is made in the x pointing (yaw) of U-M8, and a corresponding correction is made with U-M9 to bring the spot on-center for the far iris. U-RR is then moved all the way back again, and the motion of the spot is once again noted; the x deviation should either decrease (if the change was in the correct direction) or increase (if it was not). U-RR is then brought forward and the process is repeated as necessary until no x deviation is observed, indicating the beam is parallel to the axis of motion in the xz plane. The same process can be repeated to remove y deviation, at which point the beam is parallel to the delay stage's axis of motion.

Alignment of the pump path proceeds to the sample stage by aligning U-MF, U-M10, and U-M11 to the marked iriss. U-M12 is then used to aim the pump beam at the sample, as described below.

A.3 Sample stage and detection alignment

To configure the detector for TAA measurement, the three outputs of the BPD (P_+, P_-, and D as described in Section 2.3.1) are connected to three lock-in amplifiers, through a 100 kHz BNC lowpass filter to average over the slight differences in the temporal responses of the BPD photodiodes. The reference signal for all is the same triggering signal used to reference the chopper. The first step to aligning the detector is to rotate the Wollaston prism (R-PrW), which splits the parallel and perpendicular polarization components of an incoming beam (relative to its own optical axis) into two diverging beams. With the probe beam unblocked and no sample in place, R-PrW is rotated about the z-axis until the plane of two outcoming beams is parallel to the laser table, and the BPD is placed such that one beam is incident on each photodiode.

The next step is to set the polarization of the probe beam to 45° relative to the optical axis of the Wollaston prism. Importantly, note the positions of both R-P and U-P; the polarizers must be placed directly before the sample, to remove any spurious depolarizing effects of reflection or other optics. To do so, the lock-in amplifier for the differential signal D is temporarily referenced to a 5 kHz triggering signal (i.e., the repetition rate of the laser) rather than to the chopping frequency, such that the voltage readout is proportional to the magnitude of the shot-to-shot difference between the two polarization components of the beam. R-P is then rotated until this differential signal reaches a minimum (near 0), indicating the intensity of the two polarization components is equal and thus the polarization of the probe is 45° relative to the R-PrW.

Lastly, the polarization of the pump is set to 45° relative to the probe. To do so, a temporary third "analyzer" polarizer is placed after the probe polarizer R-P. The rotation of the analyzer is set to the point of full extinction, indicating it is set exactly 90° relative to the probe. The analyzer is then rotated exactly 45° relative to this position using the Vernier scale on the mount. Then, the analyzer is moved after the pump polarizer U-P, and the rotation of U-P is set to full extinction, thus set 45° relative to the probe.

Last, the pump and probe must be overlapped in space and time. The reference frequency of all lock-in amplifiers is set back to the pump chopping frequency, and the sample is placed in the sample holder. It may be useful to use a reference sample with a long-lived TA signal for this procedure. The delay stage is set to a relatively large positive time delay, and U-M12 is used to aim the pump beam to overlap the probe while monitoring the three lock-in outputs on an oscilloscope. When overlap is achieved, a signal will appear on the P_+ and P_- channels, and likely the D channel unless the anisotropy is very short-lived. This signal is maximized by alignment of U-M12 to overlap the pump with the probe. Then, time $t = 0$ is found by reducing the delay until the exact time of signal onset is found. The time of maximum signal is then found, and the gains of the lock-in amplifiers are set based on this signal. The gains of the P_+ and P_- lock-ins should be equal and set just low enough to avoid saturation of either signal. The gain of the D lock-in should be set low enough to avoid saturation.

With these parameters set, the apparatus is prepared to take a transient absorption anisotropy measurement.

Appendix B

Optics diagrams of stroboSCAT microscope

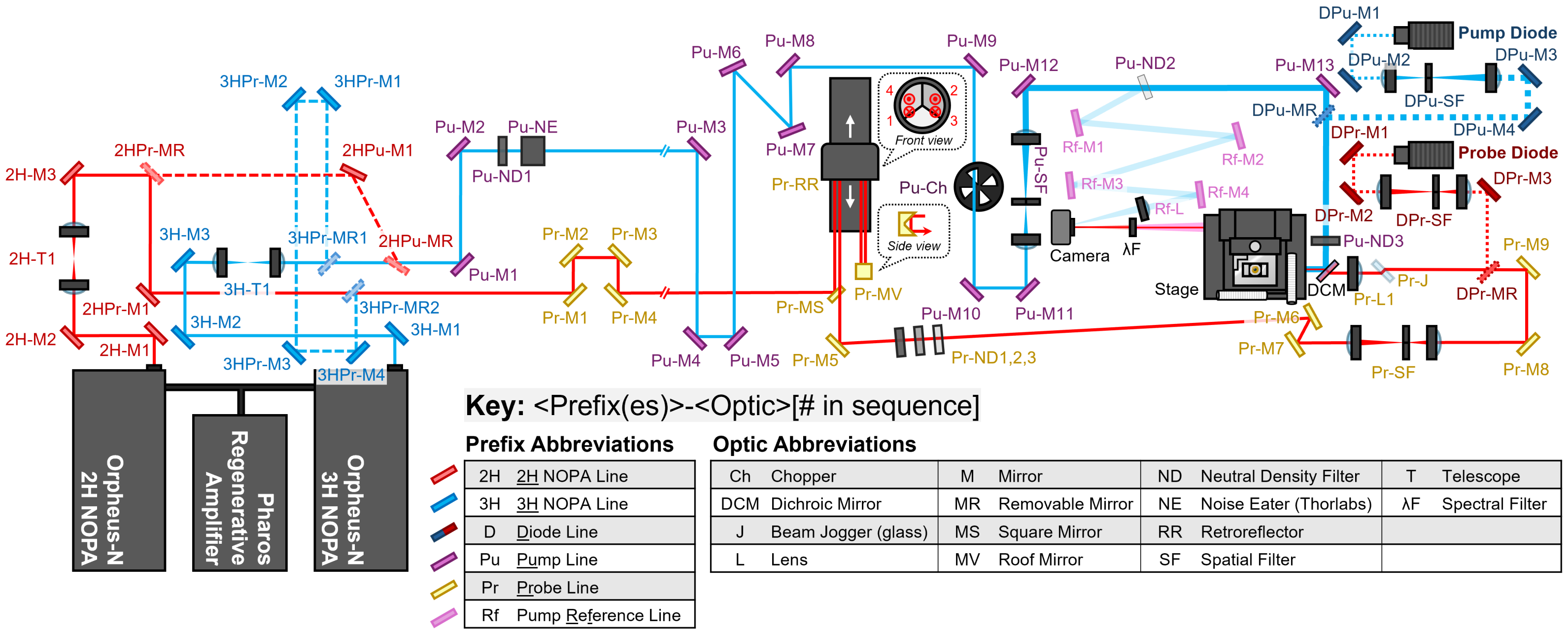

Key: <Prefix(es)>-<Optic>[# in sequence]

Prefix Abbreviations

🟥	2H	2H NOPA Line
🟦	3H	3H NOPA Line
▨	D	Diode Line
🟪	Pu	Pump Line
🟨	Pr	Probe Line
▨	Rf	Pump Reference Line

Optic Abbreviations

Ch	Chopper	M	Mirror	ND	Neutral Density Filter	T	Telescope
DCM	Dichroic Mirror	MR	Removable Mirror	NE	Noise Eater (Thorlabs)	λF	Spectral Filter
J	Beam Jogger (glass)	MS	Square Mirror	RR	Retroreflector		
L	Lens	MV	Roof Mirror	SF	Spatial Filter		

Figure B.1: Optical diagram of the newly configured stroboSCAT microscope (to approximate scale, note // breaks in beams where paths have been visually shortened), with all optional configurations shown. Retroreflector callout depicts order of incidences of beam on retroreflector, with ⊗ and ⊙ indicating in and out of plane, respectively. All mirrors shown are protected silver mirrors, and mounted transmissive optics have an aperture size of 25 mm, with the exceptions of Pu-NE (5 mm diameter) and the pinholes in Pu-SF and Pr-SF (25 um).

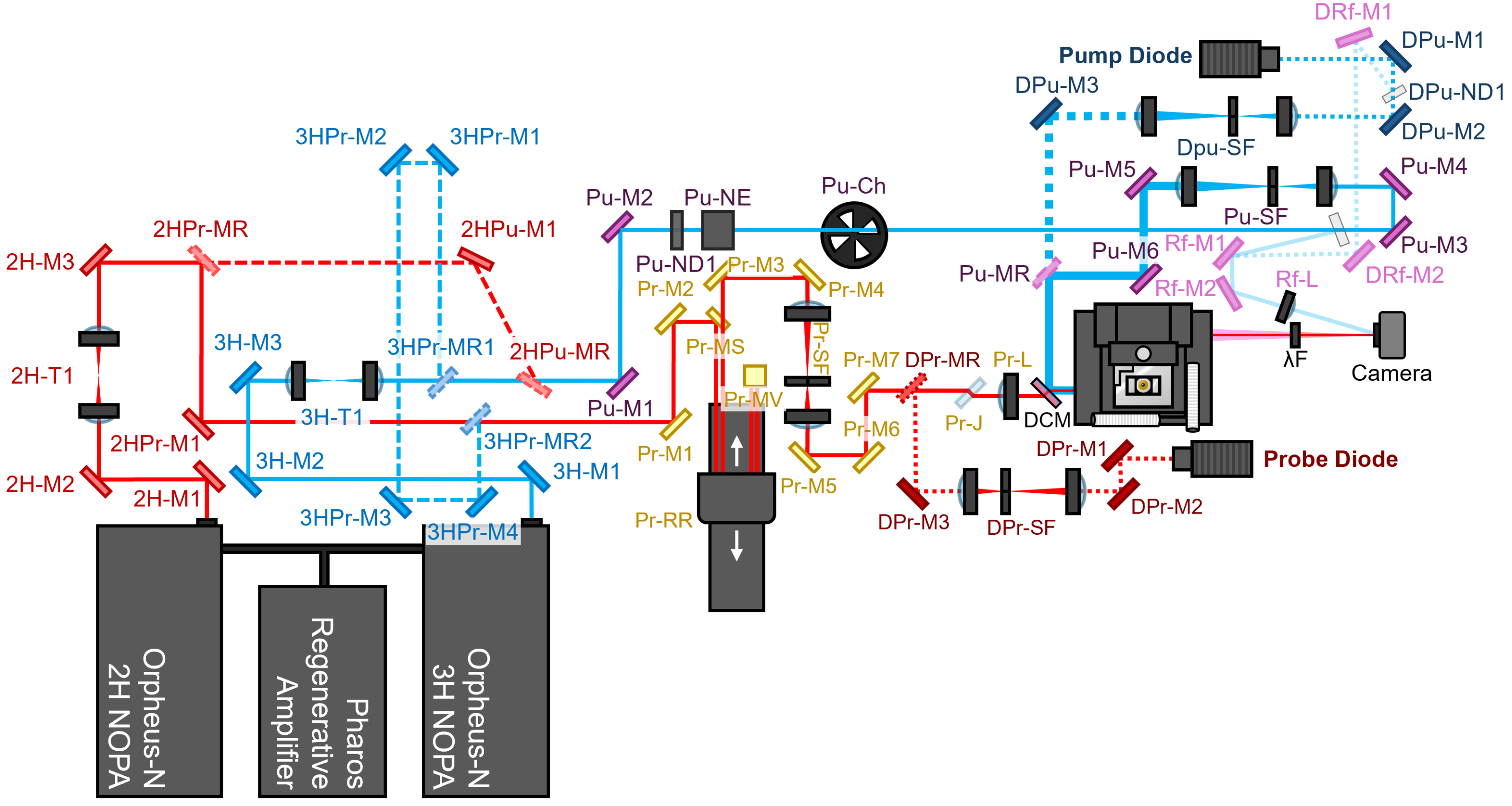

Figure B.2: Proposed reconfiguration of stroboSCAT microscope to shorten probe path length and reduce vibration effects. See Fig B.1 for optic labeling key.